



Universitat Autònoma de Barcelona

Facultat de Ciències - Departament de Física
Estudis de Doctorat en Física

TOWARDS HIGHLY SENSITIVE AND MULTIPLEXED NANOPLASMONIC BIOSENSORS

DOCTORAL THESIS - NOVEMBER 2012

Dr. B. Sepúlveda Martínez
DIRECTOR

Prof. J. Pascual Gainza
TUTOR

M. A. Otte Ortiz
AUTHOR



Voor Mijn Vader

Abstract

In this dissertation, different aspects of refractometric nanoplasmonic sensors are discussed. First, a theoretical and experimental sensing performance assessment is made of Localized Surface Plasmon Resonance (LSPR) sensors based on single gold nanorods, by directly comparing them to conventional thin film Surface Plasmon Polariton (SPP) sensors. Besides the discovery of a material-specific optimized spectral sensing region that can be accessed via precise nanoparticle engineering, this work reveals a better biosensing performance for LSPR sensors that can be further improved if certain - inherent - drawbacks are overcome.

For this, arrays of gold nanodisks are used to identify and suppress such drawbacks. First, negative influences that stem from thin metal adhesion layers and the high refractive indices of the supporting substrate are analyzed. It is shown that the right choice of material and thickness for these adhesion layers, significantly improves the signal-to-noise ratio (S/N)-values of these biosensors. Besides, by placing the nanodisks on nanopillars, thereby distancing them from the substrate, much higher sensitivities can be obtained, providing a strategy that can be easily expanded to other plasmonic systems.

Next, it is demonstrated that the employed arrays of gold nanodisks support a guided mode, that besides other interesting nanophotonics applications, alters the far-field radiation of these nanoplasmonic structures in such a manner, that both enhanced sensitivities and improved S/N-ratios are obtained. Finally, combining all gathered knowledge, a road map is sketched towards the creation of a LSPR sensor with multiplexing capabilities and integrated microfluidics.

Resumen

En esta tesis se ha abordado la caracterización de sensores LSPR refractométricos desde diferentes puntos de vista. En primer lugar, se presenta un análisis teórico y experimental de nanocápsulas cilíndricas (*nanorods*) de oro, comparando su capacidad sensora con sensores SPP convencionales. El estudio ha conducido al hallazgo de una región espectral con rendimiento sensor optimizado, y a la que se puede acceder llevando a cabo un diseño preciso y detallado de las nanoestructuras. Por otro lado, el análisis desvela un rendimiento superior de los LSPR comparado con los convencionales SPP, con atisbos de mejoras adicionales si se superan ciertos inconvenientes inherentes a estas plataformas biosensoras.

De cara a identificar y suprimir estos inconvenientes, se han empleado matrices de nanodiscos de oro como nanoestructura modelo. En primer lugar, se han analizado las influencias negativas que se derivan de las finas capas metálicas de adhesión y de los altos índices de refracción del sustrato que soporta a los nanodiscos. Se ha demostrado que la elección adecuada del material y del espesor de estas capas de adhesión mejora significativamente la relación señal-ruido. Además, mediante la colocación de los nanodiscos sobre nanopilares dieléctricos, alejándolos del sustrato, se han obtenido incrementos significativos de sensibilidad, proporcionando así una estrategia que se puede extender fácilmente a otros sistemas plasmónicos.

Se ha demostrado, por otro lado, que estas matrices de nanodiscos soportan un modo guiado, que, además de otras aplicaciones nanofotónicas interesantes, provoca un cambio en la radiación en campo lejano de estas estructuras que causa mejoras en sensibilidad y en la relación señal-ruido. Por último, se han combinado todos los conocimientos adquiridos y resultados obtenidos para esbozar la creación de un biosensor LSPR con funciones de multiplexado y con microfluídica integrada.

Acknowledgements

Desde aquí, quiero dedicarle mi agradecimiento a todas esas personas, que durante estos años me han proporcionado la ayuda, el apoyo y el cariño necesario para llevar a cabo este trabajo. En primer lugar, quiero dar las gracias a dos personas que lo significan todo para mi: mi madre y mi hermano. A pesar de las distancias, vuestro apoyo y confianza incondicional en todo lo que hago, han sido una ayuda incalculable durante todos estos años. Borja, het was een genot om je gedurende deze jaren te zien groeien van broertje naar broer. Os quiero.

Desde aquí también quiero dar las gracias a una persona sin la cual hoy no me encontraría aquí escribiendo estas palabras: Borja Sepúlveda. Ha sido un verdadero placer trabajar al lado de alguien tan impregnado con el *gen científí co*. Añadiéndole a eso tu exquisito gusto musical, y la cantidad de buenos momentos que hemos pasado fuera del laboratorio, no me queda otra que concluir que estos años han sido excepcionales. Gracias por todo.

Laura Lechuga, quiero darte las gracias por los muchos consejos recibidos durante estos años y por propocionarme el espacio y los medios necesarios para poder haber llevado a cabo este trabajo. Te considero la principal responsable de la grata experiencia que ha sido trabajar en este grupo. A mi tutor, Jordi Pascual, le quiero agradecer el interés mostrado en este trabajo durante las conversaciones que hemos tenido a lo largo de estos años. Also, I would like to thank Anatoly Zayats for his kind hospitality during my internship in London.

Este trabajo tampoco hubiera sido posible sin el soporte técnico recibido por parte de diversas personas. Por eso, quiero dar las gracias a Raquel y M. Angeles, las chicas de sala blanca de la UAB, por las numerosas ayudas recibidas en la fabricación de

muestras. Siempre me acordaré del impecable estado en el que mantenéis el *Spinner*, y las bronquitas recibidas por no limpiarlo (lo suficientemente) bién ;-). Also, I would also like to thank Nikos for the received service regarding the metal evaporator. Y también, agradecer al Ministerio de Ciencia e Innovación la financiación de esta tesis a través del Programa Nacional de Formación de Profesorado Universitario (FPU).

En cuanto al grupo NanoB2A y sus satélites que lo han rodeado en todo momento puedo ser muy breve: sois fantásticos! Es difícil poner palabras a todo lo vivido con cada uno de vosotros. Por nada cambiaría mi aventura en el Centro del Universo junto a David² y sus respectivas: Rebequita y la Señora Artiles. Han sido tantos, y tan buenos los momentos que he pasado junto a vosotros, que no sabría por donde empezar. Simplemente quiero daros las gracias por absolutamente todo lo vivido en este periodo de tiempo! Cerdanyola City no hubiera sido lo mismo sin la compañía de *mi hermano* Orly, Ana (y el *juego* que ha dado su patio...) y el CAP. Muchas han sido las fiestas ahí acompañados de *The Others* (Ya sabéis, los del extra-radio...): Mar (*La del chocolate*), Laurita (*La del no-chocolate*), Stefáááania (*No me gusta el chocolate, pero tampoco la canela - Really???*) y la Dra. Happy. Poco a poco me habéis ido convenciendo de que vivir con *los otros* tan malo no era, hasta que llegó el momento en que hasta yo caí :). Con el tiempo, mientras unos nos abandonaban (Fernando, Elena, Laura F., Nico, Juan, Eva, Sofía, Braulio), han ido llegando refuerzos de primerísima calidad: Daphné, Silvia, María, César, Sam, Iraís, Dulce y Jesús. Ha sido un placer pasar tiempo con cada uno de vosotros, ya sea dentro o fuera de las paredes de la ETSE! Sois lo mejor!

Aan vrienden en familie in Nederland zou ik het volgende willen zeggen. Ondanks het feit dat we elkaar de laatste jaren veel minder zien dan voorheen, blijven onze ontmoetingen in Nederland en/of Spanje als vanouds aanvoelen! En dat is mij ontzettend veel waard. Bij deze, Opa, Derek, Nick, Arthur, Jaap: Bedankt!

I vull acabar donant les gràcies per tot i més a la meva parella, M.-Carmen. Tot el viscut amb tu és inoblidable. Sempre t'estaré agraït per tot el suport i afecte que has després cap a mi durant aquests anys. També et vull donar les gràcies, com també els les dono als teus pares i als teus germans, per haver-me fet sentir sempre en família. Sense tu, això no hagués estat el mateix. Kusje :-)

Contents

| | |
|--|-------------|
| Abstract | v |
| Resumen | vii |
| Acknowledgements | ix |
| Contents | xiii |
| Motivation and Objectives | 1 |
| 1 Nanoplasmonic Biosensors | 3 |
| 1.1 Nanoplasmonics | 8 |
| 1.2 Biosensors | 9 |
| 1.3 Optical Biosensors | 12 |
| 1.3.1 Biosensors Based on Dielectric Waveguides | 14 |
| 1.3.2 Biosensors Based on Propagating Surface Plasmons | 15 |
| 1.3.2.1 Surface Plasmon Polaritons | 15 |
| 1.3.2.2 Refractometric SPP Sensing Concept | 18 |
| 1.3.2.3 SPP Biosensing Trends | 20 |
| 1.4 Biosensors Based on Localized Surface Plasmons | 22 |
| 1.4.1 Localized Surface Plasmon Resonances | 22 |
| 1.4.1.1 Polarizability Spherical Nanoparticles | 23 |
| 1.4.1.2 Polarizability Ellipsoidal Nanoparticles | 26 |
| 1.4.1.3 Extinction Cross-sections | 28 |
| 1.4.2 Refractometric LSPR Sensing Concept | 28 |

| | | |
|----------|--|-----------|
| 1.4.3 | Fabrication of LSPR Nanostructures | 30 |
| 1.4.3.1 | Colloidal Nanoparticles | 30 |
| 1.4.3.2 | Nanostructured Substrates | 32 |
| 1.4.4 | LSPR Biosensing Trends | 34 |
| 1.4.4.1 | Refractometric LSPR Sensors | 34 |
| 1.4.4.2 | Other LSPR Sensing Approaches | 36 |
| 2 | Materials and Methods | 41 |
| 2.1 | Sample Fabrication | 43 |
| 2.1.1 | Nanorod Synthesis | 43 |
| 2.1.2 | Hole-Mask Colloidal Lithography | 44 |
| 2.1.2.1 | Disk-Density Variations | 47 |
| 2.1.2.2 | Au Nanodisk Dimers | 48 |
| 2.1.2.3 | Pillar-supported Nanodisks | 48 |
| 2.2 | Experimental Measuring Schemes | 50 |
| 2.2.1 | SPP Biosensor | 50 |
| 2.2.2 | Single Particle Spectroscopy | 51 |
| 2.2.3 | LSPR Reflection Measurements | 54 |
| 2.2.3.1 | Fixed Angle Measurements (Chapter 4) | 54 |
| 2.2.3.2 | Multi-angle Measurements (Chapter 5) | 55 |
| 2.2.4 | Atomic Force Microscopy | 56 |
| 2.3 | Details on Bulk Sensing Experiments | 56 |
| 2.4 | Details on Surface Sensing Experiments | 57 |
| 2.4.1 | Deposition of Polyelectrolyte Monolayers | 57 |
| 2.4.2 | DNA Hybridization Measurements | 58 |
| 2.4.3 | Carb/Anti-Carb Immunoassay | 58 |
| 2.5 | Theoretical Simulations | 59 |
| 2.5.1 | Optical Constants | 59 |
| 2.5.2 | SPP Simulations | 59 |
| 2.5.3 | Single Particle LSPR Simulations | 59 |
| 2.5.3.1 | Quasi-static MLWA Calculations | 60 |
| 2.5.3.2 | FDTD Calculations | 61 |
| 2.5.4 | Maxwell-Garnett Effective Medium | 62 |
| 3 | Sensing Performance Comparison: Single Particle LSPR vs. SPP Sensor | 65 |
| 3.1 | Introduction | 67 |

| | | |
|----------|--|------------|
| 3.2 | Simulations | 70 |
| 3.2.1 | Bulk Sensitivity Comparison | 70 |
| 3.2.2 | Surface Sensitivity Comparison | 75 |
| 3.2.3 | Impact of Substrate RI on LSPR Sensing Performance | 76 |
| 3.3 | Experiments | 78 |
| 3.3.1 | Experimental Bulk Sensitivity Comparison | 78 |
| 3.3.2 | Experimental Surface Sensitivity Comparison | 80 |
| 3.4 | Analytical Derivation Optimized Sensing Region | 83 |
| 3.5 | Influence of the Particle Shape on the Sensing Performance | 85 |
| 3.6 | Discussion and Conclusion | 87 |
| 4 | Overcoming Substrate Effects for Improved LSPR Sensing | 89 |
| 4.1 | Introduction | 91 |
| 4.2 | Effect of Adhesion Layers on Sensing Performance | 92 |
| 4.3 | Effect of Substrate RI on Sensing Performance | 95 |
| 4.3.1 | Influence of Substrate RI on Nanodisk Sensing Performance | 95 |
| 4.3.2 | Improving the Sensing Sensitivity Suspended Nanodisks | 97 |
| 4.3.3 | Experimental Bulk Sensitivity Suspended Au Nanodisks | 98 |
| 4.3.4 | DNA Hybridization Measurements | 100 |
| 4.3.5 | Bulk Sensitivity of Suspended Au Nanodisk Dimers | 102 |
| 4.4 | Discussion and Conclusion | 104 |
| 5 | Far-Field Guided Modes for Improved LSPR Sensing | 105 |
| 5.1 | Introduction | 107 |
| 5.2 | TE Guided Modes in Thin Monolayers of Au Oblate Spheroids | 108 |
| 5.2.1 | Mode Dispersion and Reflectivity Spectra | 108 |
| 5.2.2 | Bulk Sensitivity Analysis | 114 |
| 5.3 | Experimental Results | 116 |
| 5.3.1 | Experimental Mode Dispersion and Reflectivity Spectra | 116 |
| 5.3.2 | Experimental Bulk Sensitivity Assessment | 118 |
| 5.3.3 | Carb/Anti-Carb Immunoassay | 120 |
| 5.4 | Discussion and Conclusion | 122 |
| 6 | Towards a LSPR Biosensor with Multiplexing Capabilities | 125 |
| 6.1 | Introduction | 127 |
| 6.2 | Miniaturized High-Angle LSPR Sensor | 127 |
| 6.2.1 | Standalone Real-time Readout Software | 130 |

| | | |
|---------|--|------------|
| 6.3 | Towards a Multiplexed LSPR Sensor | 133 |
| 6.3.1 | Fabrication | 133 |
| 6.3.1.1 | Design | 134 |
| 6.3.1.2 | Instrumentation | 136 |
| 6.3.2 | Software | 136 |
| 6.3.3 | Au Nanodisk Samples and PDMS Microfluidics | 139 |
| 6.3.3.1 | Fabrication of PDMS microfluidics | 139 |
| 6.3.3.2 | Sample Assembly | 142 |
| 6.4 | Discussion and Conclusion | 143 |
| | General Conclusions | 145 |
| | List of Publications | 149 |
| | List of Figures | 151 |
| | Abbreviations and Acronyms | 155 |
| | Symbols | 159 |
| | Bibliography | 163 |

Motivation and Objectives

Nanoplasmonics studies light-matter interactions that take place on metal nanostructures. The Localized Surface Plasmon Resonance (LSPR) excited on metal nanoparticles upon interaction with light, attributes some very remarkable optical properties to these sub-wavelength structures. Among the numerous applications of nanoplasmonics, one that stands out relates to label-free refractometric biosensing. In this regard, metal nanoparticles are considered to be the next-generation refractometric sensing platforms, thereby offering higher levels of miniaturization, multiplexing opportunities and possibly even better sensitivities than conventional sensing techniques. Given the relative youth of this research area, there are still a lot of gaps to fill in order to obtain a complete - quantitative and qualitative - picture of all the pros and cons inherent to the use of metal nanoparticles as label-free refractometric sensing platforms. With this work, we intend to contribute basic knowledge to this ever-growing field of interest. To this end, the **main objectives** for this work are formulated as follows:

1. Sensitivity assessment of label-free refractometric nanoplasmonic biosensors, in order to determine the true potential of these new generation biosensors.
2. Providing strategies to optimize the sensing performance of refractometric nanoplasmonic biosensors.
3. The development, fabrication, and optimization of a miniaturized nanoplasmonic biosensor with multiplexing capabilities.

Chapter 1

Nanoplasmonic Biosensors

This chapter comprises a general introduction to nanoplasmonic sensing. A short description of nanophotonics and - its subfield - nanoplasmonics is followed by a brief discussion of optical biosensors. Finally, both topics are combined, thereby shifting focus towards the field of refractometric nanoplasmonic sensing. Herein, the key concepts of these sensing platforms are discussed and a brief overview regarding the state-of-the-art of this research field is given.

In the late sixties and beginning of the seventies, Prof. Richard P. Feynman, who was awarded the Nobel Prize in 1965 for his work on Quantum Electrodynamics, gave a unique introductory course on physics to undergraduate students at Caltech, whose transcripts were bundled forming the *Feynman Lectures on Physics*. [1] Among these teachings, covering subjects ranging from classical to quantum physics, one particular lecture stands out, in which the visionary skills of Feynman prognosticated the trend that technology would follow in the next decades. In this lecture, titled *There is Plenty of Room at the Bottom*, Feynman sketched a future world, dominated by molecular manipulation, a world not governed by gravity, a world that would bring information storage and computing power to unprecedented levels. As he literally stated in 1959:

As soon as I mention this, people tell me about miniaturization, and how far it has progressed today. They tell me about electric motors that are the size of the nail on your small finger. And there is a device on the market, they tell me, by which you can write the Lord's Prayer on the head of a pin. But that's nothing; that's the most primitive, halting step in the direction I intend to discuss. It is a staggeringly small world that is below. In the year 2000, when they look back at this age, they will wonder why it was not until the year 1960 that anybody began seriously to move in this direction.

In retrospect, history has proven that Feynman could not have been more right. In the decades that would follow, a new field in science - **nanotechnology** - emerged and was directly linked to Feynman's vision in the book *Engines of Creation*. [2] It comes as no surprise that this new field draws its name from the prefix *nano-*, being the characteristic one-billionth-of-a-meter-scale at which all engineering in this ever-growing research field takes place. Two illustrating examples that characterize the possibilities offered by this exciting field of expertise were pursued with the help of Scanning Tunneling Microscopy (STM) and Atomic Force Microscopy (AFM). [3, 4] These nanotechnology-related techniques, belonging to the family of scanning probe microscopies, provide both the ability of imaging and manipulating on an atomic level. Following this path, Donald M. Eigler, researcher at IBM, used STM to move and control the position of 35 individual Xe atoms, enabling him to create the company corporate logo on an atomic scale, as shown in Figure 1.1A. Years later, the Mirkin Research Group at Northwestern University (Chicago, USA) devised a new AFM based patterning method, called dip-pen lithography, [5] that combined with lateral mode AFM made it possible to write and image the cited paragraph from Feynman's

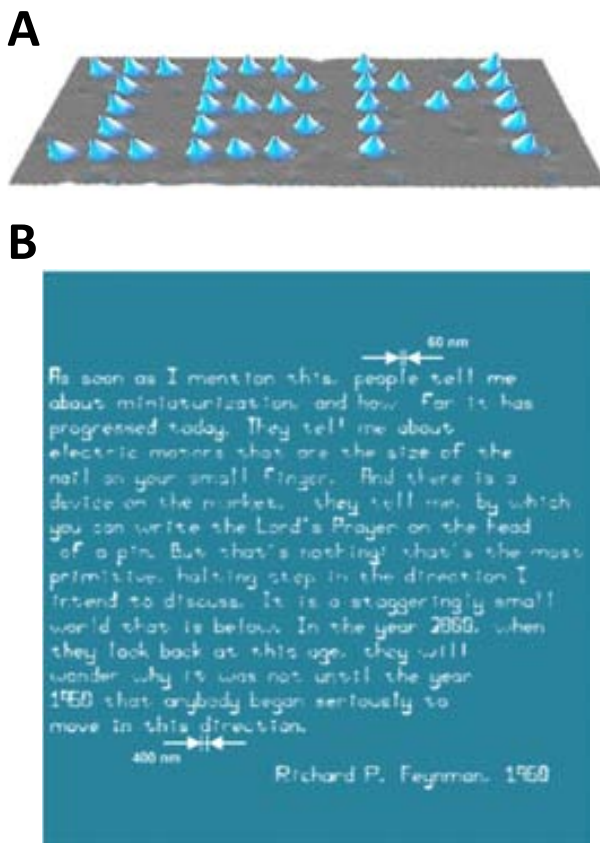


Figure 1.1: Examples of advances in nanotechnology. (A) STM image of the corporate IBM logo spelled out with 35 individual Xe-atoms (Donald M. Eigler, IBM, 1989). (B) Paragraph of Feynman's 'There is plenty of room at the bottom', written using Dip-Pen Nanolithography, and imaged using lateral atomic force microscopy (Mirkin Group at Northwestern University).

lecture on a nanometer scale, as shown in Figure 1.1B, exemplifying Feynman's vision of extreme miniaturization. Currently, nanotechnology has become one of the most vivid and evolving fields in science, with an exponential increase in nanoscience-related publications since the late nineties, leading toward a current amount of tens of thousands of scientific papers per year (Figure 1.2A).

The exponential growth experienced by nanotechnology in the last decades has forced its subdivision into different, but closely related subfields, among which **nanophotonics** can be highlighted. Boosted by the emergence of new fabrication

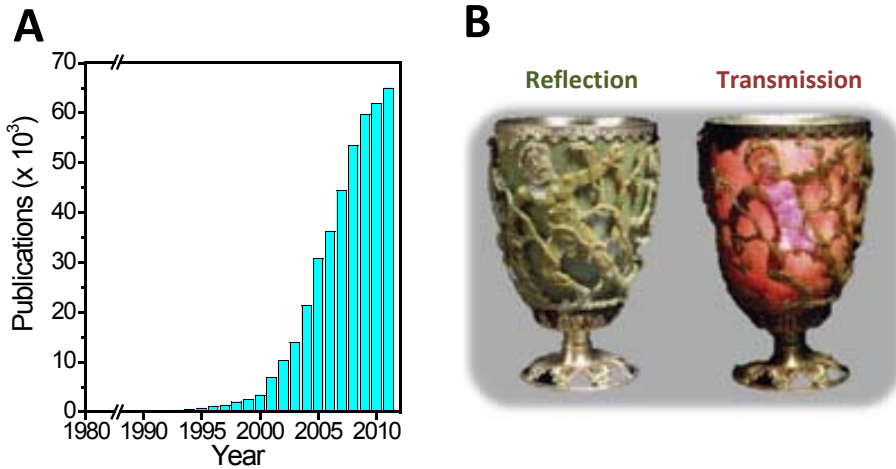


Figure 1.2: (A) Approximate yearly amount of publications in the field of nanotechnology and (B) the Lycurgus Cup seen in reflection (left) and in transmission (red).

techniques that enable the fabrication of nanostructured materials, nanophotonics studies light-matter interaction at sub-wavelength scales, thereby being heavily influenced by the physical, chemical and structural nature of either artificial or natural nanostructures. Within nanophotonics, different research branches can be distinguished. The first subfield of nanophotonics studies discrete quantum confinement of electrons in sub-wavelength nanostructures. These structures, typically made out of semiconductors and dielectrics, exhibit optical effects that are directly related to these quantized electron states and manifest themselves via specific, size-dependent absorption and emission spectra. Within this field, much effort is being put in the exploitation of these remarkable optical phenomena in order to create components for photonic circuitry such as lasers, emitters, filters and optical switches. A second subfield of nanophotonics deals with the confinement and transport of light waves in structured dielectric materials, commonly known as waveguides. This field, being governed by classical optics, also focuses on the development of integrated photonic circuitry, such as waveguides, photonic crystals, and cavities. Finally, the last category of nanophotonics is known as **nanoplasmonics**. This research area investigates the interaction of light with metal nanostructures. As described in the next section, the extraordinary optical properties of metal nanostructures give rise to a wide range of novel and interesting nanoplasmonics-driven applications.

1.1 Nanoplasmonics

The field of nanoplasmonics explores light-matter interactions that take place on metal structures with dimensions well below the wavelength of light. Interaction of the electro-magnetic (EM) wave with a nanostructure, via its coupling to the free electrons of the metal, induces a collective oscillation of these charges. When the wavelength of the EM wave matches the eigenfrequency of this free electron oscillation, this collective motion of charges is greatly amplified, giving rise to a surface bound plasmon mode, known as a Localized Surface Plasmon Resonance (LSPR). This enhanced electron oscillation amplifies the scattering and absorption cross-section of the nanostructures at specific wavelengths. As a direct consequence, metal nanoparticles tend to exhibit very bright colors that have fascinated people for centuries. One of the most illustrative examples is shown in Figure 1.2B, depicting the Lycurgus Cup: an ancient Roman cup, currently exposed in the British Museum. This object, made out of dichroic glass, which is composed out of nanoparticles, appears green when viewed in reflected light, whereas when light is transmitted from the inside of the cup through the glass, the cup appears to be red, illustrating the remarkable optical properties of these nanometer-sized objects. Theoretical interest in the optical properties of nanoparticles dates back to the 20TH century. [6] However, it has not been until recently, that, accompanied by the eruption of nanotechnology, providing new methods to fabricate, structure and measure nanoscale materials, nanoplasmonics has experienced a gigantic experimental boost leading to a deeper comprehension of these light-metal interactions.

Within this growing field of expertise, the search for novel technological applications, has forced nanoplasmonics to diverge into several subfields. In this regard, the use of metal nanoparticles in applications involving solar-cell technologies, sub-wavelength and biomedical imaging, photocatalysis, drug delivery, therapeutics, biomolecular sensing and nano-optical circuitry can be highlighted. [7] Currently, especially the latter two fields draw much attention from the scientific community. The area that deals with nano-optical circuitry is of a very fundamental nature, and is mainly dedicated to the creation and development of passive and active nanoplasmonic components for photonic circuitry. Nanoplasmonic circuitry is expected to surpass the current standards of electronic signal processing, thereby proclaiming higher processing speeds (nothing travels faster than light) and unprecedented levels of miniaturization. For this to happen, plasmonic alternatives for standardized electronic components such as waveguides, switches and transistors have to be developed. An

example that points into this direction, are linear chains of metal nanoparticles, that have proven their use as plasmonic waveguides exploiting the EM near-field interparticle coupling. [8] Despite the limited propagation lengths, and the expensive fabrication methodologies, this pioneering work shows a glimpse of the huge possibilities offered by this novel field. Next to passive components, such as waveguides, also active optical components are needed for fully optical circuits. To this end, active optical control of nanoplasmonic structures is mandatory. Boosted by the enhanced EM near-field of metal nanostructures, this active control can be accomplished by precisely controlling the refractive index (RI) surrounding the employed nanostructures. In this regard, liquid crystal molecules, in which the RI depends on the molecular alignment, or dielectric materials with strong Kerr nonlinearities, can be exploited to trigger RI changes around the nanoparticles using either external electric fields, or ultrashort laser pulses, respectively. [9]

As previously mentioned, apart from nanophotonic circuitry, also the use of metal nanoparticles for sensing applications receives much scientific interest. Exploiting the enhanced optical near-field of metal nanostructures, different sensing approaches exist that enable the qualitative and quantitative study of biomolecular interactions. Among these, applications involving enhanced molecular spectroscopy, colorimetric sensing assays and label-free refractometric nanoplasmonic biosensing can be emphasized. [10–12] The latter field, that is, the one based on label-free refractometric nanoplasmonic biosensing, is the main topic of this dissertation. Before describing the basic sensing concept and the reported applications involving label-free LSPR sensing (Section 1.4), first, a general overview of biosensors, and in particular, optical biosensors, is given in Sections 1.2 and 1.3, respectively.

1.2 Biosensors

A biosensor is an analytical tool that is built out of biological or biomimetic recognition elements that contact a transducer, the latter being able to translate a biological recognition event into a measurable and quantifiable signal. Biosensors allow for the detection of specific analytes (detectable substances) for which the receptor layer was specifically designed. Therefore, when a solution containing different substances/molecules contacts the device, only those with strong affinity for the recognition elements are able to produce molecular recognition events (Figure 1.3). The latter gives rise to a series of physical-chemical alterations detected by the transducer, yielding a quantifiable signal that strongly depends on the target analyte

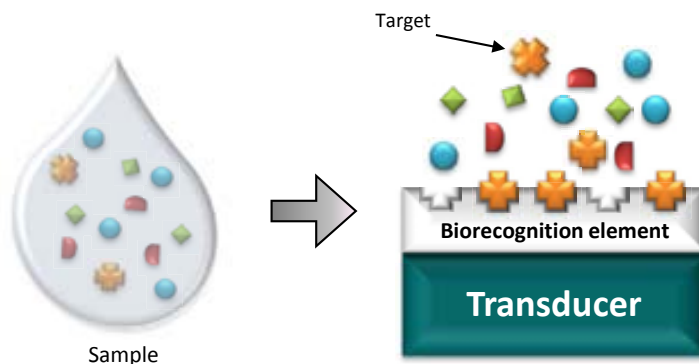


Figure 1.3: Schematic representation of a biosensor, including the transducer, the biological recognition element and specific and non-specific analytes.

concentration.

Contact of the molecular receptor layer with the transducer provides the sensing device with a **sensitivity** and **selectivity** for a certain target analyte. Furthermore, compared to other analytical tools, biosensors offer the possibility of a **label-free** and **real-time** detection, opening up pathways to evaluate the kinetics of the biological interaction. Most biosensors also benefit from their ease of use, their limited physical size and portability, thereby enabling their use at otherwise inviable locations, such as the doctor's office, or even at home (glucose electrochemical sensors [13]). Also, these devices typically require small sample volumes (μL - nL), which is especially important when for example cellular tissue, extracted via a biopsy, needs to be analyzed.

For biosensors, the creation of an optimized biomolecular receptor layer via precise surface modification procedures is one of the most critical and challenging tasks. Besides an efficient coverage of the transducer surface, the receptor layer should allow for surface regeneration, suppress non-specific absorptions when analyzing real samples and maintain its properties, such as functionality (affinity and specificity), structure and biological activity. Hence, the design of a proper biomolecular recognition layer via the optimization of all these previously mentioned factors is considered to be a key factor that determines the quality of a sensing platform. In practice, many biomolecules can be used as bioreceptors, such as antibodies, nucleic acids, aptamers, cell receptors among many others. Logically, the choice of receptor biomolecule is strongly conditioned by the intended sensing application, thereby requiring high specificity for the selected target molecule. To this end,

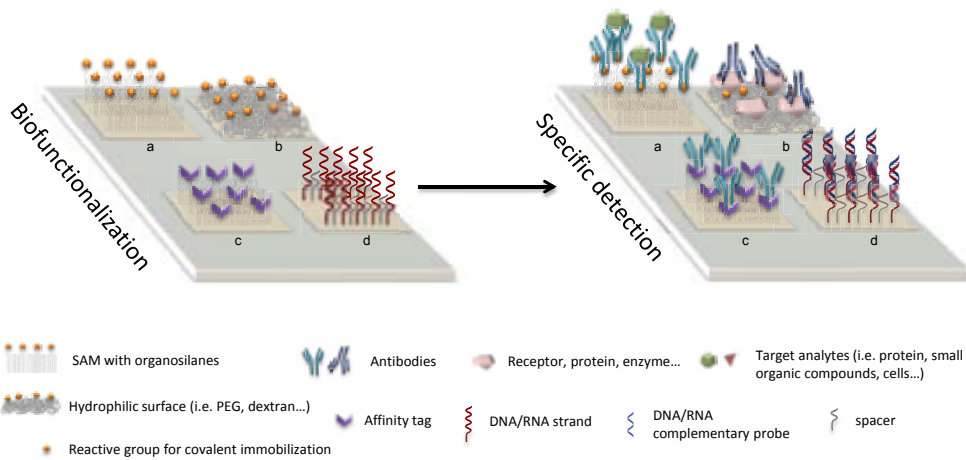


Figure 1.4: Schematic representation of different biosensing assays, depicting (A) a mixed self-assembled monolayer with reactive and non-reactive silanes compounds with specific antibodies covalently immobilized for protein recognition, (B) hydrophilic and biocompatible reactive monolayer based on pegylated-silane or dextran compounds with proteins covalently immobilized for antibody recognition, (C) affinity tags immobilized on the surface (i.e. protein A, or streptavidin onto biotinylated surface) to achieve appropriate orientation of specific antibodies for protein recognition and (D) covalent immobilization of DNA or RNA probes (together with non-specific spacers) for hybridization with complementary DNA/RNA strands (Courtesy of Estévez et al. [14]).

several surface biofunctionalization strategies exist, among which one can highlight direct immobilization strategies via physical absorption or covalent linking, or indirect immobilization approaches, such as non-covalent molecule binding to a previously deposited active layer, or physical entrapment of biomolecules in polymer layers. A selection of several different surface modification protocols are schematically depicted in Figure 1.4

Besides categorization based on the family of employed biological receptors, biosensors can also be distinguished by the nature of the measured physiochemical process. In this regard, biosensors can be separated in those based on catalytic reactions, [15] in which the biomolecular recognition event is followed by a chemical modification of the target analyte, thereby facilitating its detection, and those categorized as affinity-based biosensors. [16] In this latter group, the molecular recognition is based on the characteristic affinity that exists between a specific target and its receptor molecule. In a similar manner, biosensors can be classified depending on the type of employed transducer. Following this path, six mayor

groups of biosensors can be distinguished. The first group comprises electrochemical sensors. [17–20] In these devices, commonly using enzymatic bioreceptors, the transducer measures electrochemical changes caused upon molecular recognition events. Secondly, acoustic-wave biosensors, employ acoustic transducers that detect changes of mass via a micro-balance composed out of a piezoelectric crystal. [21] In a similar manner, micro-mechanical biosensors use micro-cantilevers in a static or dynamic mode in order to detect biomolecular interactions (mass-changes) that take place on the cantilever surface. [22] Next, magnetic biosensors, employ magnetic micro- or nanoparticles covered with bioreceptor elements for specific target analytes. A secondary element (gel/matrix), then captures only those particles on whose surfaces a biomolecular interaction has taken place, after which a magnetic sensing technique is used determine the number of these particles. [23, 24] Furthermore, calorimetric sensors use heat changes caused by exothermic or endothermic properties of certain catalyzed reactions, as a measure for the reaction rate, and hence, the analyte concentration. [25–27] Finally, the last category is formed by optical biosensors. [28] These sensors detect biomolecular interactions by measuring changes of the optical properties of the transducer that are induced by the same molecular recognition event. This sensing protocol can be achieved by measuring changes of RI, or via fluorescence-, polarization- or dispersion-based detection schemes.

1.3 Optical Biosensors

Over the years, optical biosensors have profiled themselves as an alternative commercial technology, given their undisputed advantages over electrochemical sensors, such as higher levels of sensitivity, the non-requirement of reference electrodes, immunity against electrical interferences and higher versatility. Optical biosensors can be separated in two large sub-groups: optrodes and evanescent wave sensors. Optrodes consist of an optical fiber that is positioned both in- and outside of a flow cell in which a biomolecular interaction takes place. [29, 30] Then, specific molecular probes - immobilized on the exposed fiber surface - interact with target analytes thereby inducing a quantifiable change of the fiber's optical properties (absorption, fluorescence, RI, bioluminescence or dispersion).

On the other hand, evanescent wave sensors exploit the possibility of EM field confinement in certain dielectrics and/or metals. [31] Biosensors based on this phenomenon are characterized by 1) the use of an EM mode, which can be either **propagating** or **localized**, and 2) the detection principle of *evanescent wave sensing*.

In this sensing concept, part of the EM guided mode penetrates into the external medium, forming a so-called evanescent field. This evanescent field forms a unique and ideal probe to detect any biochemical reaction that takes place within its extent. Hence, changes of RI in the external medium caused by molecular recognition events, change the optical properties of the excited EM mode. This relative change provides a quantitative measure for the analyte involved in the biomolecular interaction. Besides, given the exponential decay of the evanescent wave into the external medium, the only changes that can be detected are forced to take place close to the surface of the material on which the EM mode is excited, thereby minimizing the possibility of interference with other substances present in the solution. As a direct consequence, biosensors based on this sensing principle are considered to be ideal candidates for affinity-related analyte detection, without the need of any molecular marker, thereby allowing for label-free detection. [32]

To date, the vast majority of evanescent field biosensors are based on the properties of propagating guided modes. Within this latter field, distinction can be made between those using conventional dielectric waveguides (Figure 1.5A, left panel), and those based on propagating plasmonic modes excited at a planar metal-dielectric interface (Figure 1.5, right panel). Details regarding both sensor types are extensively discussed in Sections 1.3.1 and 1.3.2.

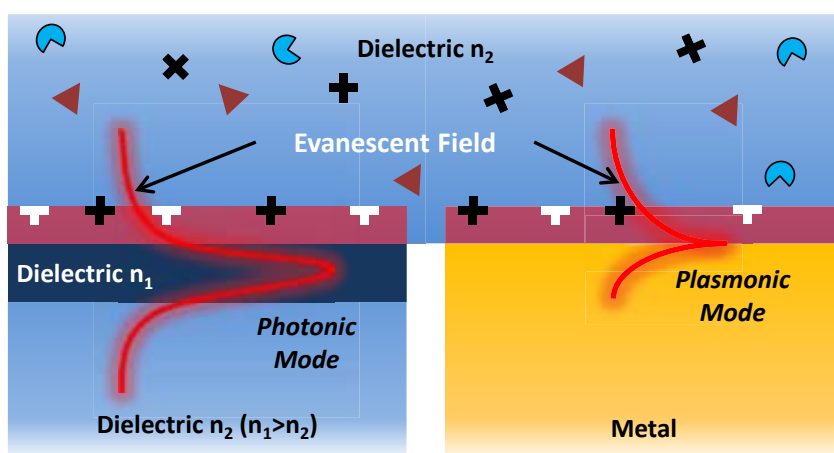


Figure 1.5: Schematics depicting the sensing principle of evanescent wave sensors based on propagating EM modes, thereby distinguishing between those devices relying on conventional waveguides (left), and those on surface plasmon polaritons (right).

1.3.1 Biosensors Based on Dielectric Waveguides

Photonic biosensors based on dielectric waveguides can be differentiated by using the employed waveguiding mechanism as the categorizing factor. Continuous advances in silicon technology have stimulated the fabrication of a large variety of photonic biosensors, comprising devices based on optical fibers, planar waveguides, integrated optics, photonic crystals and whispering gallery modes. [14] Optical fiber-derived biosensors implement the evanescent wave sensing principle by partly exposing the cladding layer of the fiber, thereby creating a sensor area close to the fiber core. [45] Planar waveguide biosensors, such as those based on resonant mirrors, are dielectric waveguides that use frustrated total internal reflection (TIR) to probe RI changes on the sensing surface. [34, 46] Next, integrated optics biosensors are highly miniaturized and typically very sensitive sensing platforms that usually employ a certain interferometric detection scheme. Examples are bimodal waveguides, [35] Young interferometers, [47] Fabry-Perot interferometers, [48] Mach-Zehnder interferometers, [49, 50] and Hartmann interferometers. [51] Furthermore, photonic crystals are periodic dielectric or metallo-dielectric nanostructures, that possess

Table 1.1: Comparison of limit of detection (LOD) of optical sensors based on evanescent wave detection.

| Type | LOD (pg/mm ²) | LOD (RIU) | REF |
|-----------------------------|----------------------------|--|----------|
| Optical Fibers | n.d. ⁽¹⁾ | 10 ⁻⁷ | [33] |
| Resonant Mirrors | 0.1 | 10 ⁻⁶ | [34] |
| Bimodal Waveguides | n.d. | 10 ⁻⁷ | [35] |
| Mach-Zehnder Interferometer | 0.01 ⁽²⁾ – 0.06 | 10 ⁻⁷ – 10 ⁻⁸ ⁽²⁾ | [36, 37] |
| Young Interferometer | 0.01 ⁽²⁾ – 0.75 | 10 ⁻⁸ – 10 ⁻⁹ | [38, 39] |
| Hartmann Interferometer | n.d. | 10 ⁻⁶ | [40] |
| Photonic Crystal | 0.4 | 10 ⁻⁵ | [41] |
| Optical Microresonator | 1 | 10 ⁻⁷ | [42, 43] |
| SPP-based Sensor | 1 – 5 ⁽³⁾ | 10 ⁻⁵ – 10 ⁻⁸ | [44] |
| LSPR-based Sensor | n.d. | 10 ⁻⁴ | [10–12] |

⁽¹⁾not determined

⁽²⁾estimated values

⁽³⁾averaged values

precisely defined photonic bands and band-gaps enabling their use as waveguides with strong light confinement, turning these devices into attractive sensing platforms. [52, 53] Finally, biosensors based on whispering gallery modes, such as optical micro-resonators, are sensing platforms that contain ring-shaped dielectric waveguide structures that are optically coupled to one or more linear waveguides. [54, 55]

It has been proven difficult to determine which of all these sensors is most sensitive, since for this, a thorough and precise study in equal conditions is a prerequisite (electrical noise, stability, immobilization and detection, etc.). However, when analyzing the limit of detection (LOD) of all above mentioned biosensors, including the plasmonic sensors that will be discussed in a later stadium (Table 1.1), it can be concluded that at this very moment the interferometric biosensors stand out against all others. Nevertheless, for photonic sensors based on dielectric waveguides, external coupling of light into the waveguided devices is commonly a rather difficult process, that requires much stability and precision and is therefore considered to be an important drawback for the practical implementation of these sensor types. Furthermore, although much advancements have been made, the surface chemistry on silicon-based surfaces is not as standardized as the thiol-based surface chemistry on gold surfaces. It comes therefore as no surprise, that plasmonic sensors, with user-friendly light-coupling methods and well-developed surface modification protocols are considered to be good and widely employed alternatives.

1.3.2 Biosensors Based on Propagating Surface Plasmons

For decades, the field of plasmonic sensing has been dominated by sensing platforms based on propagating surface plasmons, known as Surface Plasmon Polaritons (SPPs). [44] A SPP is excited at the planar interface between a thin metal film and a dielectric. General details regarding SPPs and their implementation in refractometric SPP sensing schemes are provided in the following sections, together with a short overview discussing various SPP sensing applications.

1.3.2.1 Surface Plasmon Polaritons

SPPs are surface charge waves that propagate at the interface between a thin metal film and a dielectric, as schematically depicted in Figure 1.6A. This EM mode generates transversal field distributions with their maxima located at the metal-dielectric interface and exhibit exponentially decaying evanescent fields into both media (Figure 1.6B). A SPP is limited to transverse-magnetic (TM) modes only,

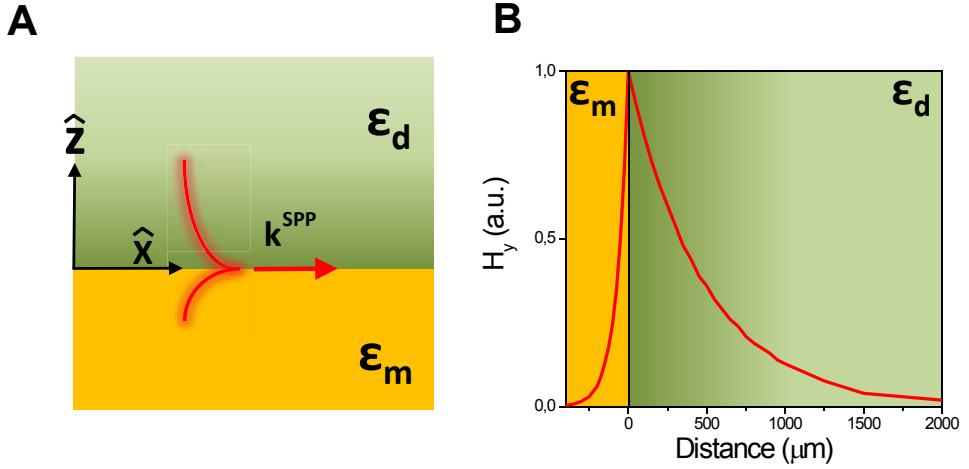


Figure 1.6: (A) Schematics of a SPP at an interface of a metal and a dielectric, together with the transversal magnetic field distribution H_y of a SPP at a Au/H₂O ($n_d = 1.33$ and $\epsilon_m = -11.8 + 1.246i$) interface for $\lambda = 633$ nm.

and possesses a wave vector (k_x^{SPP}), which is expressed by: [7]

$$k_x^{SPP} = k_0 \sqrt{\frac{\epsilon_m \epsilon_d}{\epsilon_d + \epsilon_m}} \quad (1.1)$$

In equation 1.1, ϵ_m and ϵ_d are the dielectric constants corresponding to the metal and the dielectric, respectively, while $k_0 = \omega/c = \omega \cdot \sqrt{\epsilon_0 \mu_0}$, represents the wave vector of light in vacuum. For equation 1.1 to be valid, the wavelength dependent real part of the metal's dielectric constant must be negative, that is, $\text{Re}[\epsilon_m] < 0$, and $\text{Re}[\epsilon_d] < -\text{Re}[\epsilon_m]$. These conditions are satisfied by a numerous amount of metals. Nevertheless, normally Au or Ag is used, since for these two metals, the required excitation conditions can be met in the visible (VIS) and near infra-red (NIR) regions of the light spectrum, thereby considerably simplifying the SPP excitation. Besides, due to the relatively low imaginary part of the dielectric constant of these two metals, losses caused by plasmonic damping are strongly suppressed when compared to other plasmonic materials.

Equation 1.1 shows that SPPs cannot be excited by direct illumination with light. This can be easily deduced by considering the wave vector of incoming light:

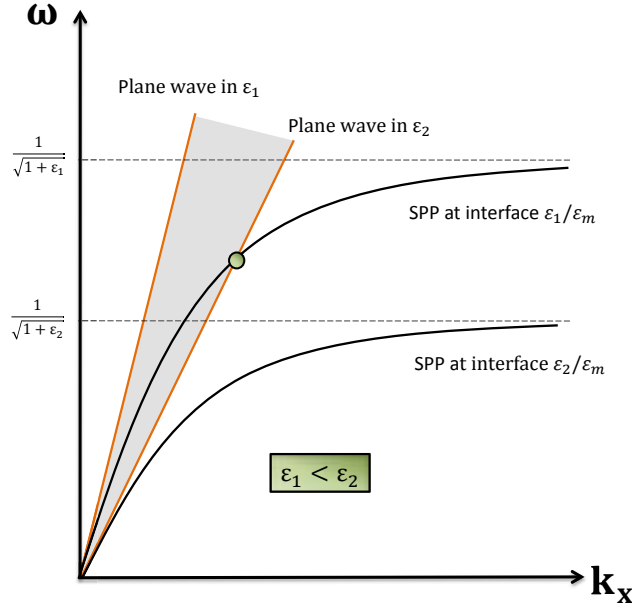


Figure 1.7: Dispersion relations of SPPs excited at different metal-dielectric interfaces, together with the dispersion relations of plane waves traveling through the same dielectrics.

$$k_x^{Light} = \frac{2\pi}{\lambda} \sqrt{\epsilon_d} \sin \theta \quad (1.2)$$

In this equation θ is the incidence angle of the incident light. Direct comparison of equation 1.2 with k_x^{SPP} shows that:

$$|k_x^{Light}| < |k_x^{SPP}| \quad (1.3)$$

This behavior is clarified in Figure 1.7. Herein, it can be seen for two different dielectrics, that the dispersion relations of a plane wave traveling through each of them, and that of SPP excited at a metal-dielectric interface composed of the same dielectric material, never cross, thereby ruling out any possibility of direct SPP excitation. In general, this means that in order to excite SPPs, k_x^{Light} needs to be enlarged. To this end, several techniques have been developed. The most common method to do this employs a prism-coupled Kretschmann excitation scheme. [56] This methodology uses a high RI prism (ϵ_p) to excite the SPP (Figure 1.8A). In this configuration the following wave vector coupling condition can be satisfied:

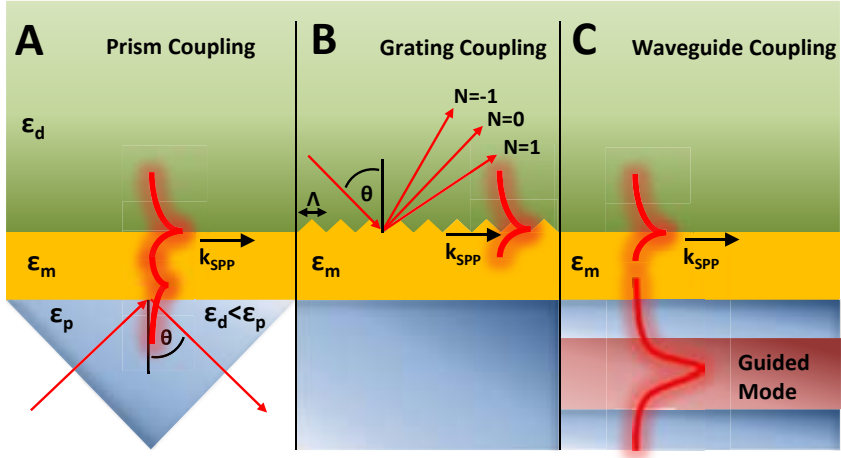


Figure 1.8: SPP coupling methods, including (A) a prism-coupled Kretschmann configuration, (B) grating coupling and (C) waveguide coupling.

$$k_x^{SPP} = \frac{2\pi}{\lambda} \sqrt{\epsilon_p} \sin \theta \quad (1.4)$$

This equation shows that both θ and λ can be used to match k_x^{SPP} . Hence, SPPs can then be detected as sharp reflectivity dips as a function of θ (for a fixed λ) or in a spectroscopic approach (for a fixed θ). Although less frequently used, plasmon excitation can also be accomplished via grating coupling, [57] or via the use of the evanescent field of guided light traveling through a photonic waveguide. [58] Schematic representations of both techniques are shown in Figures 1.8B and 1.8C, respectively.

1.3.2.2 Refractometric SPP Sensing Concept

Equation 1.1 reveals that k_x^{SPP} , and thus the SPP excitation condition, strongly depends on the dielectric constant ϵ_d of the external dielectric medium. This dependency forms the basis of refractometric SPP sensing. In general, the penetration depth of the SPP's evanescent field into the external dielectric can reach up to hundreds of nm in the VIS range of the light spectrum. Therefore, a biomolecular reaction within its extent induces a local RI change that alters the SPP wave vector, and thus, its excitation condition, providing a quantitative methodology for the label-free detection of biomolecular interactions that take place close to the metal surface.

Hence, SPP biosensors are based on the prior immobilization of specific receptor molecules on the metal surface, in which the latter acts as a transducer. Besides

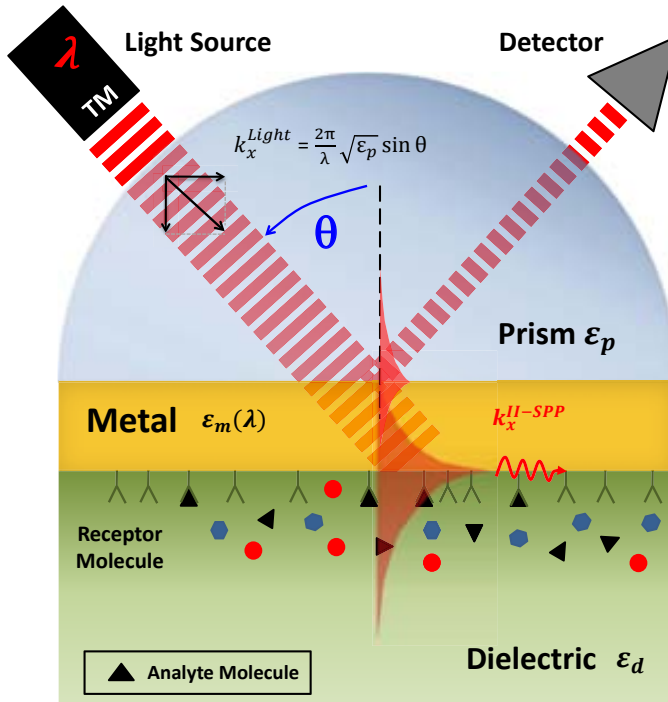


Figure 1.9: Schematics of a SPP biosensor, employing a Kretschmann configuration with a monochromatic light source.

the transducer, these devices typically comprise three major components, being 1) the light source (mono-chromatic or broadband), 2) a detector (intensity- or phase-based), and 3) one of the previously discussed excitation methods, which, motivated by simplicity, generally is a prism-coupled excitation scheme. Figure 1.9 depicts the schematics of a Kretschmann-based SPP biosensor where SPP excitation is achieved with a TM-polarized monochromatic laser and the reflected light is collected with a photodetector. In this particular sensing scheme, SPP excitation can be achieved by either using λ or θ as tuning parameters. Since the wavelength is fixed (monochromatic light source), the reflected light is measured as a function of θ . At a certain angle, denoted as θ_{TIR} (Figure 1.10A), TIR sets in. As θ increases, the reflected intensity exhibits a strong decrease, until a minimum value is reached. It is at this angle (θ_{SPP}), where k_x^{Light} equals k_x^{SPP} , yielding excitation of the SPP. Local RI changes, alter the SPP wave vector, thereby producing a lateral displacement of the reflectivity curve (Figure 1.10A), providing a quantitative measure for the induced

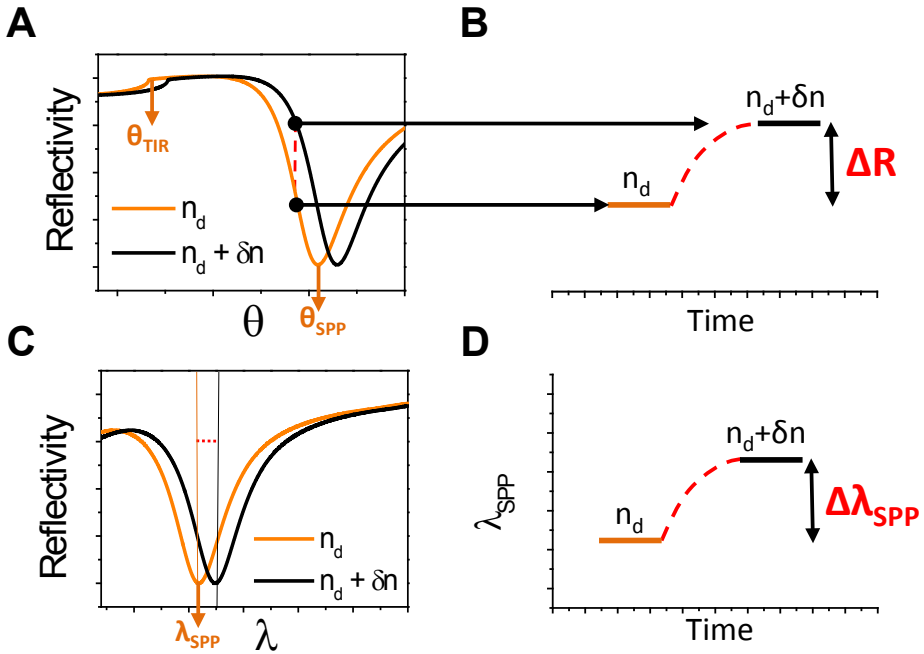


Figure 1.10: Representative SPP curves for (A) θ - and (B) λ -interrogated SPP sensors, together with their corresponding real-time tracking of curve displacements via (C) the monitorization of changes of reflectivity R or (D) shifts of the resonance wavelength λ_{SPP} .

RI change. This information can be measured by time-dependent monitorization of the entire curve, or by fixing θ at the point where the slope of the SPP resonance curve is maximized, after which intensity changes of the reflected light are monitored as a function of time. This latter approach is illustrated in Figure 1.10B.

It should be noted that the roles of both λ and θ can be interchanged. In this case, a broadband light source at a fixed θ is used for SPP excitation. Then, spectral analysis of the reflected light results in a reflectivity spectrum with a dip located at λ_{SPP} (Figure 1.10C), which is also subjected to lateral (spectral) displacements induced by changes of RI. Spectral monitorization of λ_{SPP} translates changes of RI into a measurable quantity that can be extracted as a function of time (Figure 1.10D).

1.3.2.3 SPP Biosensing Trends

SPP biosensors are the most widely employed label-free optical biosensors, and can be used in the determination of any type of biochemical interaction. [44]

Currently, several commercial devices are on the market, while new prototypes are appearing continuously. This technique has been applied in biomolecular engineering, drug design, monoclonal antibody characterization, epitope mapping, phage display libraries, virus-protein interaction, environmental pollutants detection, among other interesting fields. In general, SPP sensors based on diffractions gratings, [59] integrated optics, [60] or fiber optics, [61] offer the possibility to design more compact and integrated sensors, although they show lower sensitivity than prism-coupled devices. Interestingly, diffraction gratings can be designed in such a way that they simultaneously excite the SPP and out-couple the light towards a position sensitive detector. This approach allows for the wavelength interrogation without the need of spectrometers, [62] which can simplify and reduce the cost of the device. One problem of the conventional SPP sensors derives from the long penetration of the evanescent field into the dielectric. As a consequence, SPP sensors simultaneously detect both local RI changes due to the biosensing interactions and bulk RI changes. The simultaneous excitation of long range and short range SPPs in metal layers allows for the distinction between both effects. [63, 64]

Nowadays, the most important challenge of SPP biosensors is multiplexing. The most simple way to reach these levels of high-throughput detection is provided by Surface Plasmon Imaging (SPI). [65] In this technique, a collimated monochromatic light beam excites the SPP in an extended area via prism coupling. The reflected light suffers an intensity modulation due to the variations of RI in different parts of the metallic layer, which can be analyzed in a 2D charge-coupled device (CCD) camera. If various biomolecules are immobilized at different parts of the metal layer, the multianalyte biosensing measurement can be made with the analysis of the 2D reflected intensity pattern. However, this multiplexing technique is limited due to its poor lateral resolution. This drawback stems from the propagating nature of the SPP, which is around tens of μm in the VIS region, and increases in the NIR, thereby limiting the miniaturization of the sensing channels and causing inter-channel cross-talk. In addition, the LOD in SPI sensors is generally lower than in conventional SPP sensors with wavelength interrogation. To improve the LOD of such SPI systems, a wavelength division multiplexing scheme has been proposed. [66, 67] Such a scheme uses different incidence angles or dielectric overlayers to spectroscopically discriminate between sensing channels. Using this arrangement the simultaneous measurement of four pairs of channels has been shown. [67] To increase the number of sensing channels, a spatially patterned multilayer with polarization contrast imaging has been reported. [68] The presented prototype has 108 channels and its size is $400 \times 800 \text{ mm}^2$.

The polarization contrast, together with the patterning, increases the resolution and reduces channel cross-talk.

Another important issue regarding SPP sensors is increasing their LOD. To this end, several SPP configurations have been described as, for example, the phase sensitive SPP based Mach-Zehnder configuration, [69] the differential ellipsometric Surface Plasmon Resonance (SPR), [70] or the optical heterodyne SPR. [71] In the same way, a magneto-plasmonic biosensing concept has been shown, [72] based on the combination of the magneto-optic (MO) activity of magnetic materials and the SPR of metal layers. Such a Magneto-Optic Surface Plasmon Resonance (MOSPR) biosensor shows a very sharp MO resonance, in which the measurements derive from the reflectivity modulation induced by an oscillating magnetization. This MOSPR device can reduce the signal-to-noise ratio (S/N) and improve the LOD of conventional SPP sensors significantly. [73] Independently of the type of employed SPP sensor, the LOD of these devices varies between 1 and 5 $\text{pg}\cdot\text{mm}^{-2}$ of adsorbed biological material on the sensing surface. Nevertheless, these values are insufficient for detection of low concentration of very small molecules ($M_W < 1\text{k}$). Furthermore, the minimum size of the sensing area is restricted to the SPP propagation distances (10-100 μm), thereby strongly reducing multiplexing possibilities.

1.4 Biosensors Based on Localized Surface Plasmons

In order to overcome the drawbacks related to SPP sensing, the use of metal nanoparticles, along with their LSPRs, has gained much interest as an alternative refractometric label-free sensing technique. Since the minimum sensing area of metal nanostructures is dictated by their size and no bulky coupling methods are required, metal nanoparticles offer unprecedented opportunities for sensor miniaturization and multiplexing. In this section, we first explore the fundamental optical properties of metal nanoparticles. Subsequently, the refractometric nanoplasmonic sensing concept is discussed, after which overviews are given of commonly employed fabrication methods for the creation of nanoplasmonic structures used in biosensing applications and the work done in this young research field.

1.4.1 Localized Surface Plasmon Resonances

As previously described in Section 1.1, LSPRs are non-propagating excitations of the conduction electrons of a metal nanoparticle, coupled to an EM field. Herein, we

first explore the physics behind this optical phenomenon by the hand of the most archetypical example: a metallic sphere located in an EM field.

1.4.1.1 Polarizability Spherical Nanoparticles

The coupling of an EM field to the conduction electrons of a spherical metallic nanoparticle, gives rise to a charge oscillation that builds up alternating surface charges of opposite sign that, given the curvature of the particle, result in a restoring force between them. As a consequence, the charge oscillation behaves as a single oscillating dipole, with an amplitude that is strongly influenced by this force, and hence, by the distance between the surface charges. When the diameter of this particle, denoted by a , is much smaller than the wavelength of the EM radiation, the phase of the EM field can be assumed to be constant over the entire particle volume, such that retardation effects can be neglected. In this so-called Rayleigh regime, where $a \ll \lambda$, an electrostatic approach is justified for the analysis of the optical properties of the nanoparticle. Hence, following the approach as provided by Bohren and Huffman, [74] in which the nanoparticle is treated as an ideal dipole, an expression for the particle's polarizability can be obtained. In the case of a metallic particle, with its corresponding complex dielectric function ($\epsilon_m(\lambda)$), embedded in a homogeneous dielectric medium (ϵ_d), and interacting with a static EM field E_0 (Figure 1.11A), the induced dipole moment (P) is given by:

$$P = \epsilon_0 \epsilon_d \alpha_0 E_0 \quad (1.5)$$

Herein, α_0 is the polarizability of the particle, which can be written as:

$$\alpha_0 = 4\pi a^3 \frac{\epsilon_m(\lambda) - \epsilon_d}{\epsilon_m(\lambda) + 2\epsilon_d} \quad (1.6)$$

From equation 1.6 it can be seen that the optical response is maximized when the denominator approaches zero, that is, when $\text{Re}(\epsilon_m(\lambda)) + 2\epsilon_d = 0$, defining the excitation condition for the LSPR. For metals, the dielectric function $\epsilon_m(\lambda)$ shows a strong λ -dependency. As a direct consequence, the bright colors exhibited by nanoparticles therefore strictly rely on the exact wavelength at which the LSPR resonance condition is satisfied. Furthermore, equation 1.6 also reveals the strong influence of the dielectric environment on the LSPR excitation condition. An

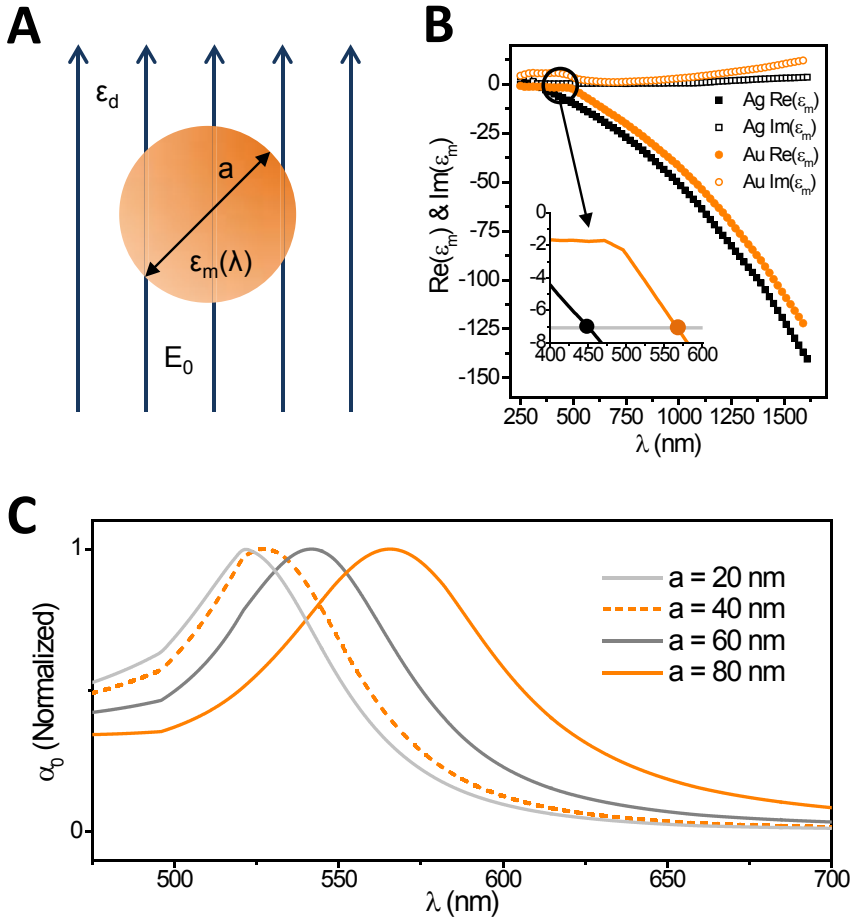


Figure 1.11: (A) Schematic representation of a spherical nanoparticle positioned in a static electric field. (B) Real and imaginary dielectric functions of gold and silver [75], showing the crossing where the denominator of the polarization of a spherical particle in H_2O equals 0. (C) Calculated normalized polarizability for spherical gold nanoparticles in H_2O for various particle diameters.

illustrative example is given by considering a spherical nanoparticle embedded in H_2O ($n_d \approx 1.33$), whose dielectric constant equals $\epsilon_d = n_d^2 \approx -3.54$, thereby dictating a LSPR excitation condition given by $\text{Re}(\epsilon_m) \approx -7.08$. For the two most employed plasmonic materials, that is, Au and Ag, whose dielectric functions are plotted in Figure 1.11B, it can then be seen that this condition is satisfied at $\lambda \approx 560$ nm (Au) and $\lambda \approx 450$ nm (Ag) (see inset Figure 1.11B).

Extension to Larger Particles

The validity of equation 1.6 is restricted to very small particles, thereby limiting this electrostatic approach to particles with length-scales below 40 nm. [76] Experimental measurements show that the LSPR red-shifts as the size of the particle increases. In addition, the linewidths of the resonance become broader due to the dephasing of the coherent oscillation of the free electrons. Therefore, for larger particles, retardation effects have to be taken into account. These effects can be accounted for by using the modified long-wavelength approximation (MLWA) methodology for the polarizability. [76] In this approximation, a modified polarizability is obtained in which the original polarizability (equation 1.6), is multiplied by a correction factor (F_{MLWA}), given by:

$$F_{\text{MLWA}} = \left(1 - \frac{2}{3}ik^3\alpha - \frac{k^2}{a}\alpha \right)^{-1} \quad (1.7)$$

The new terms in the denominator correct for the red-shift and broadening of the experimental resonance peak. To be more specific, the imaginary term in this equation represents spontaneous radiation emitted by the induced dipole. This radiative damping can be identified by an increase in the resonance line-width. On the other hand, the term that scales with $\frac{k^2}{a}$ accounts for depolarization of the collective electron oscillation, directly caused by the finite ratio that exists between the particle size and the wavelength of light. This contribution causes the LSPR to red-shift when the particle diameter is increased. After multiplication of equation 1.6 with the correction factor equation 1.7, the modified polarizability of a spherical particle can then be written as:

$$\alpha_0 = 4\eta a^3 \cdot \frac{\epsilon_m(\lambda) - \epsilon_d}{\epsilon_m(\lambda) + 2\epsilon_d - \eta(\epsilon_m(\lambda) - \epsilon_d)(2ka)^2(1 + i\frac{2}{3}ka)} \quad (1.8)$$

Figure 1.11C depicts the MLWA-compliant calculated polarizabilities of spherical gold nanoparticles with particle diameters given by 20, 40, 60 and 80 nm, which are embedded in a homogeneous dielectric medium ($n = 1.33$). These results clearly show that larger particle sizes are accompanied by the predicted red-shifting and peak-broadening features.

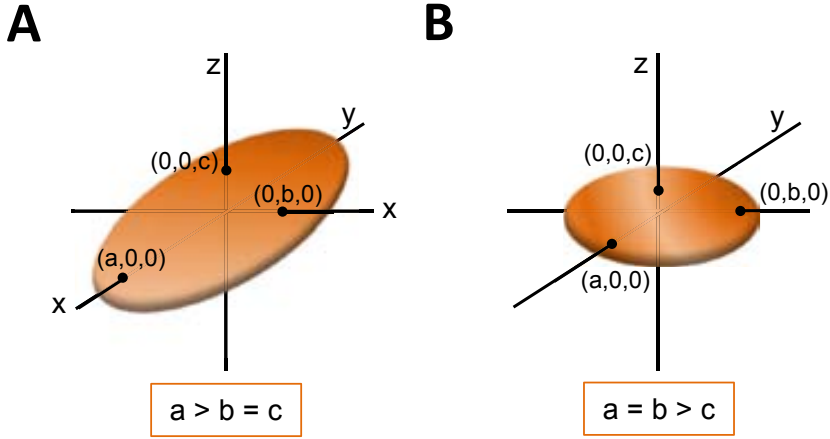


Figure 1.12: Schematic representations of (A) a prolate spheroid and (B) an oblate spheroid.

1.4.1.2 Polarizability Ellipsoidal Nanoparticles

This electrostatic approximation can be easily extended to ellipsoidal particles. Ellipsoidal particles are structures characterized by three semi-axis (a , b and c) which obey to $a \geq b \geq c$. Ellipsoids normally come in two geometries, that is, prolate spheroids (*rod-shaped*, $a > b = c$), and oblate spheroids (*disk-shaped*, $a = b > c$), shown in Figures 1.12A and 1.12B, respectively. The polarizability of an ellipsoid in the Rayleigh regime can be described with a tensor whose diagonal components are given by:

$$\alpha_i = 4\pi abc \cdot \frac{\epsilon_m(\lambda) - \epsilon_d}{3L_i(\epsilon_m(\lambda) - \epsilon_d) + 3\epsilon_d} \quad (1.9)$$

where a , b and c are the semi-axis of the ellipsoid and L_i is the shape depolarization factor, defined as:

$$L_i = \frac{abc}{2} \int_0^\infty \frac{dq}{(s_i^2 + q)\sqrt{(q + a^2) + (q + b^2) + (q + c^2)}} \quad (1.10)$$

with $s_i = a$, b , or c . As a direct consequence, ellipsoids with three different axis exhibit three different resonances. Just as for spherical particles, larger nanoellipsoid volumes are accompanied by LSPR dephasing effects. Therefore, these effects have

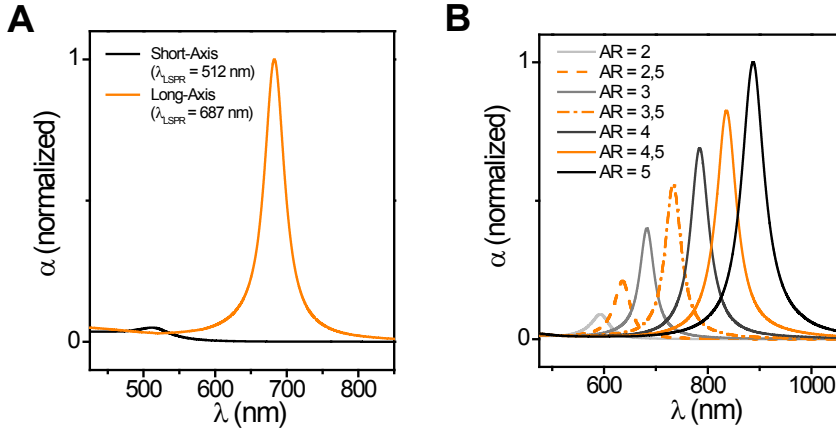


Figure 1.13: (A) Calculated short- and long-axis polarizability of a gold prolate spheroid with a 3:1 aspect ratio embedded in a homogeneous dielectric with $n = 1.33$. (B) Calculated long-axis polarizabilities of rod-shaped nanoparticles with varying aspect ratios embedded in a homogeneous dielectric with $n = 1.33$. All values are normalized with respect to the polarizability corresponding to $AR = 5$.

to be accounted for by multiplying equation 1.9 with the correction factor F_{MLWA} (equation 1.7), yielding a MLWA-compliant polarizability. Logically, when considering a spherical particle ($a = b = c$), L_i is equal in all directions ($L = \frac{1}{3}$), thereby reducing equation 1.9 to equation 1.6.

From equations 1.9 and 1.10 it becomes apparent that the polarizability of these nanoparticles strongly depends on both the shape of the particle and the its dielectric environment (ϵ_d). The size- and shape-dependency leads to another important property of plasmonic nanostructures, which is their **spectral tunability**. In this regard, the LSPR can be tailored and tuned along the entire VIS and NIR regions of the light spectrum, which is an extremely useful property for many applications, among which, biosensing can be highlighted. To illustrate this LSPR shape-dependency, here, we calculate the polarizability of a (rod-like) Au prolate spheroid with varying aspect ratios (ARs) and embedded in a dielectric medium ($n = 1.33$). In these calculations, the semi-axis a and b of the nanoellipsoid are kept constant (10 nm), while the size of the longitudinal axis is varied. As can be seen in Figure 1.13A, a nanoellipsoid for which $AR = 3$ exhibits two LSPRs: one blue-shifted (barely visible) resonance corresponding to the short-axis ($\lambda_{\text{LSPR}} \approx 512$ nm) and one corresponding to the longitudinal axis ($\lambda_{\text{LSPR}} \approx 687$ nm). The short-axis LSPR does not significantly vary when the AR of the nanoellipsoid is changed. However, as can

be seen in Figure 1.13B, by varying the AR of the nanostructure between 2 and 5, the long-axis LSPR can be tuned along the entire VIS and NIR regions of the light spectrum, thereby clearly exemplifying the extraordinary spectral tunability of these nanoparticles.

1.4.1.3 Extinction Cross-sections

When a metal nanostructure interacts with a light beam, part of the incident light is absorbed and part is scattered in different directions. The angular distribution of the scattered light is highly dependent on both the size and the spatial arrangement of the nanoparticles. Optical characterization of metal nanostructures is commonly based on extinction or scattering measurements. From a theoretical point of view, these effects can be analyzed calculating the extinction, scattering or absorption cross sections of the nanostructures. For particles that are much smaller than the wavelength of light, the scattering (C_{sca}) and absorption (C_{abs}) cross-sections can be approximated by: [74]

$$C_{sca} = \frac{k^4}{6\eta} \cdot \alpha^2 \quad (1.11)$$

$$C_{abs} = k \cdot \text{Im}(\alpha) \quad (1.12)$$

In these equations, k is the wave vector of the light, while α is the previously calculated polarizability of the particle. The extinction cross-section (C_{ext}) is then obtained as the sum of both quantities, that is:

$$C_{ext} = C_{sca} + C_{abs} \quad (1.13)$$

1.4.2 Refractometric LSPR Sensing Concept

Next to their size-, shape-, and material dependency, LSPRs strongly depend on the RI of the dielectric medium surrounding the nanostructure. When analyzing equations 1.6 and 1.9 that represent the polarizabilities of spherical and ellipsoidal particles, respectively, this ϵ_d -dependency can easily be observed. Hence, like SPP sensors, this latter property can be exploited for the use of metal nanostructures as refractometric biosensing platforms: [77] the strongly confined EM near-fields of LSPRs decay very rapidly from the particle surface into the direction of the

surrounding dielectric medium, thereby creating an evanescent field that is sensitive to changes of RI. Changes that occur in close proximity of the nanostructures, such as the specific recognition of biomolecules (Figure 1.14A), alter their immediate dielectric environment and therefore their LSPR. Hence, time-dependent spectral interrogation of metal nanostructures provides qualitative and quantitative information of the biomolecular interaction. In this regard, an increase of RI causes the LSPR wavelength to red-shift, while a decrease of RI results in a blue-shift of λ_{LSPR} (Figure 1.14B).

Coated Ellipsoidal Particles

From a biosensing point-of-view it therefore becomes very interesting to probe the EM field distribution of a metal nanoparticle close to the metal surface. This can be accomplished by computing the shift of the LSPR resonance wavelength ($\Delta\lambda_{\text{LSPR}}$) as a function of the thickness of a thin dielectric coating layer that surrounds the entire particle. For ellipsoidal nanoparticles it is possible to obtain a very useful analytical formula to describe the polarizability and retrieve the corresponding $\Delta\lambda_{\text{LSPR}}$ -values induced by a uniform dielectric shell surrounding the particle. To this end, the polarizability of a nanoellipsoid coated with a dielectric shell is expressed by: [74]

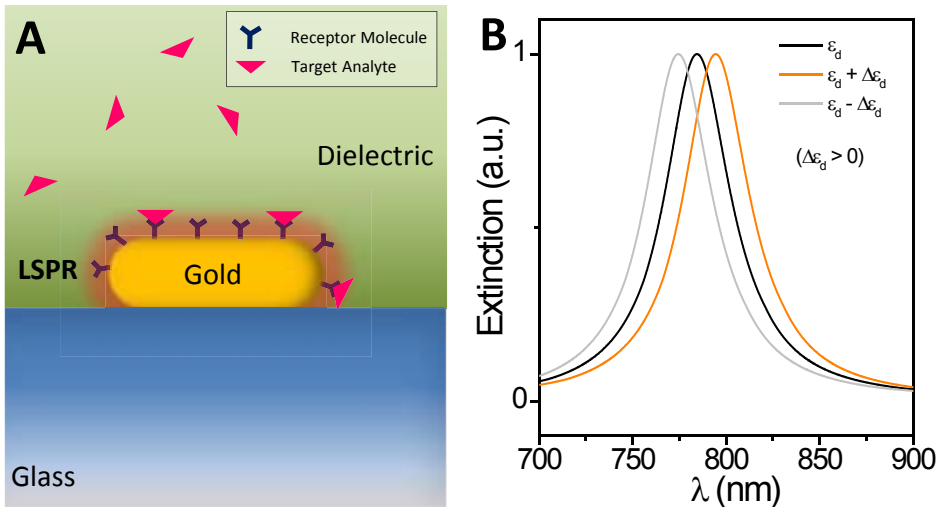


Figure 1.14: (A) Schematics representing the sensing principle of refractometric LSPR sensing using a sub-wavelength metallic nanoparticle. (B) Representative spectra that illustrate how positive/negative changes of RI, result in red-/blue-shifted LSPR peaks.

$$\alpha_i = \nu \cdot \frac{(\epsilon_s - \epsilon_f)(\epsilon_s + (\epsilon_m - \epsilon_s)(L_{i1} - fL_{i2})) + f\epsilon_s(\epsilon_m - \epsilon_s)}{(\epsilon_s + (\epsilon_m - \epsilon_s)(L_{i1} - fL_{i2}))(\epsilon_d + (\epsilon_s - \epsilon_d)L_{i2}) + fL_{i2}\epsilon_s(\epsilon_m - \epsilon_s)} \quad (1.14)$$

where

$$\nu = \frac{a_2 b_2 c_2}{3} \quad (1.15)$$

and

$$f = \frac{a_1 b_1 c_1}{a_2 b_2 c_2} \quad (1.16)$$

being a_2, b_2, c_2 and a_1, b_1, c_1 the semi-axes of the nanoellipsoids with and without the dielectric shell, respectively, L_{i2} and L_{i1} the depolarization factors in the i direction with and without the dielectric coating, and ϵ_s is the dielectric constant of the modeled dielectric coating. Logically, equation 1.14 is reduced to equation 1.9 when $\epsilon_s = \epsilon_d$. Again, in order to account for retardation and dephasing effects, equation 1.14 needs to be multiplied by F_{MLWA} (equation 1.7).

1.4.3 Fabrication of LSPR Nanostructures

Great advances in nanotechnology have led to various fabrication techniques for the creation of metal nanostructures. Generally, distinction can be made between chemically synthesized metal nanoparticles and nanostructured substrates generated by top-down lithographic processes. Both fabrication methodologies are described below.

1.4.3.1 Colloidal Nanoparticles

Colloidal metal nanoparticles are generally prepared in a process that involves the precipitation of metallic ions in a solution and subsequent stabilization of the created nanoparticles. [78–80] During this process, the size, shape and composition of the colloidal nanoparticles can be tailored precisely. The photograph in Figure 1.15 shows some examples of metal colloids, showing how depending on the previously mentioned variables, metal nanoparticles can exhibit very distinct colors. A classical approach is the citrate reduction of the Ag and Au ions in aqueous solutions, providing

simultaneous nucleation and stabilization of the nanoparticles. Other stabilization methods include the covalent linking of thiol and disulphide monolayers to the metal surface. [81, 82] Also, particle stabilization can be achieved by covering them with dielectric shells, like silica, [83] or polystyrene. [84] For further details on the fabrication methods of gold colloids, we refer to the work published by Daniel *et al.* [85] Besides, via this methodology one can also modify and control the particle shape. For example, spherical nanoparticles can be converted into nanorods, [86] in a seed mediated growth process. [87–91] Also, Ag nanoparticles can be reshaped into nanoprisms in a photoinduced process. [92–94] Furthermore, thermal processes allow for the fabrication of Ag nanobelts and triangular nanoplates starting out from spherical particles. A photoinduced process can also be employed to transform gold nanorods into spherical particles. [95]

Motivated by their tunable optical properties, another type of interesting structures are core-shell nanoparticles. As their name suggests, these particles possess a dielectric core surrounded by a metallic shell. [96, 97] The fabrication process of these composite nanoparticles starts with silica nanospheres coated with organosilane molecules, to which very small gold nanoparticles (1-2 nm) are covalently bound. The small particles act as nucleation seeds in a reduction process of chloroauric acid and potassium carbonate. In this process, it is possible to control the thickness metal shell. Using the size of the dielectric sphere and the thickness of the metal shell as variables, the resulting LSPR can be tuned over the VIS and NIR part of the light spectrum. Furthermore, an elongated core-shell structure has been reported - nanorice - that shows improved optical properties for sensing and thermal treatments. [98] Other promising nanostructures are metal hollow cages, [99] or nanocaps. [100]

Biofunctionalization of colloidal nanoparticles is a complex process due to the delicate balance between attractive Van der Waal's and repulsive electrostatic forces.



Figure 1.15: Photography that depicts different solutions of noble metal nanoparticle colloids (Courtesy of the Inorganic Nanoparticles Group, lead by Prof. V. F. Puntes - ICN, Barcelona).

Changes in the ionic strength, pH or buffer temperature can lead to the precipitation of the colloidal particles. In addition, the immobilization process can screen or modify the charge distribution at the surface of the nanoparticles breaking the colloidal equilibrium. Furthermore, the range of functionalization surface chemistries is broader and advantage can be taken from the knowledge acquired in the conventional SPP sensors. To avoid these difficulties, attachment of plasmonic nanostructures to a solid support is often a prerequisite. Besides, the latter also provides compatibility with microfluidics and in-flow sensing assays. The simplest method to attach nanoparticles onto solid supports, is based on the self-assembly of colloidal nanoparticles on the substrate. This process generally exploits the high affinity of Au and Ag colloids to amine functional groups. In this method, glass surfaces are typically silanized, thereby generating the amine terminated binding surface. [101–103] Also, attachment of colloidal particles can be achieved via mercapto groups. [104] Electrostatic interaction between positively charged polylysine treated SiO_2 surfaces and negatively charged colloids supply another strategy for particle self-assembly. [105] To optimize the sensing performance of metal nanoparticles, reduction of nonspecific binding events of the target molecules to the surface is necessary. To this end, a glass surface modified with biotinylated lipid bilayers can be employed. The lipid bilayer provides an inert supporting substrate and the biotin groups the link to attach streptavidin modified colloids to the surface. [106] In an entirely different approach, nanoshells can be fabricated directly on a solid support, by evaporating a gold film over dielectric spheres that are previously attached to a gold layer. [107]

1.4.3.2 Nanostructured Substrates

Another approach for the creation of nanostructured surfaces is offered by numerous lithographic techniques, that assure top-down fabrication methodologies. Modern lithographic techniques like Electron Beam Lithography (EBL), [109, 110] or Focused Ion Beam (FIB) lithography [111, 112] permit the fabrication of metal nanostructures (nanoparticles or nanoholes), attributing very accurate control to the size, shape and spatial distribution of the created nanostructures. An example of a Au FIB-patterned nanohole substrate can be observed in Figure 1.16A. However, these techniques are very expensive and the patterned regions are small, making them from a commercial perspective not very suitable.

In contrast, an inexpensive and large scale lithographic method that has attracted great attention is the Nanosphere Lithography (NSL). [113] This method involves drop-coating a suspension of monodisperse polystyrene nanospheres onto a substrate

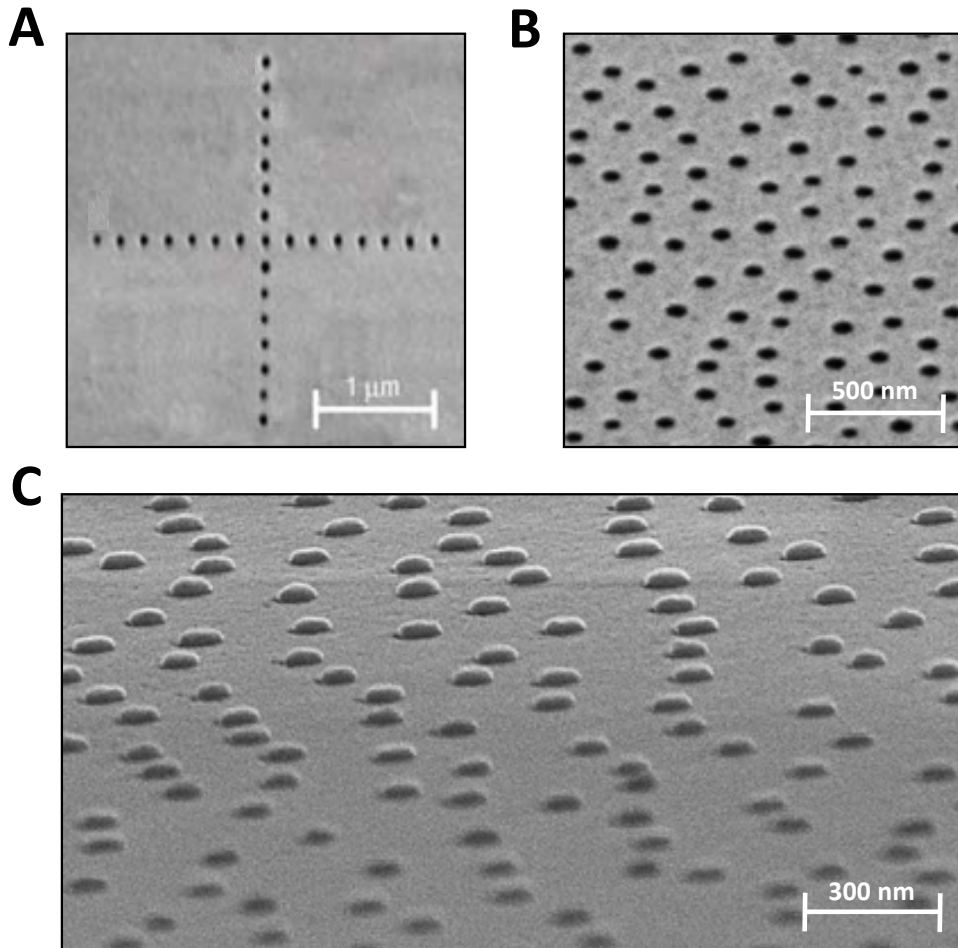


Figure 1.16: Scanning electron microscopy images of (A) nanoholes in thin gold films fabricated by focused ion beam lithography (Courtesy of Alaverdyan et al. [108]), together with gold (B) nanoholes and (C) nanodisks fabricated by colloidal lithography.

and allowing them to self-assemble in a hexagonal close-packed monolayer. The monolayer of nanospheres acts as a deposition mask through which the metal is deposited. After sonication in a solvent, an array of truncated tetrahedron shaped metal nanoparticles with hexagonal symmetry remains on the substrate. The optical properties of these arrays of nanoparticles can be tuned by controlling the size of the polystyrene spheres and thickness of the deposited metal. Colloidal Lithography (CL), and its derivation referred to as Hole-Mask Colloidal Lithography (HCL), are

two NSL-based techniques, in which much lower densities of dielectric nanospheres are used. These two techniques enable the large scale fabrication of short range ordered arrays of nanostructures, such as for example nanoholes (CL), [114] or nanodisks (HCL), [115] as displayed in Figures 1.16B and 1.16C, respectively. Following this path, also the fabrication of nanorings has been reported. [116]

Short-range ordered arrays of disks, rings, holes, [117, 118] or even more complicated quasi-3D plasmonic crystals, [119] can also be fabricated with nanoimprint lithography in large scales. These latter structures consist of a square array of 480 nm diameter wells, with a depth of 350 nm and a spatial periodicity of 780 nm in a photocurable polyurethane. Over these structures, a 50 nm Au film is evaporated to create an array of metal nanoholes and nanodisks separated by the dielectric layer. These plasmonic crystals exhibit two resonances in the NIR. The more blue-shifted peak is associated to the LSPR in the nanohole, while the second peak represents overlapping Wood's anomalies and Bloch wave SPPs.

1.4.4 LSPR Biosensing Trends

Next, an overview is presented that describes the state-of-the-art of nanoplasmonic biosensing. This overview is thereby limited to work with publication dates prior to that of the initialization of the work presented in this dissertation.

1.4.4.1 Refractometric LSPR Sensors

The number of applications involving refractometric LSPR sensing that are being reported in literature grows continually. In this section we provide the reader with a tip of the iceberg, discussing some of the most interesting applications of this ever-increasing field of expertise. Firstly, the detection of biotin-streptavidin interactions with gold colloids was shown, [101] which after particle-size optimization yielded a streptavidin LOD of 1 nM. [120] In a similar manner, these measurements were extended to protein and DNA biosensing using Au and/or Ag colloids. [103, 106, 121] Gold colloids have also been used to detect low molecular weight doping substances, like stanozolol, in a competitive immunoassay. [104] Besides, in an effort to develop portable devices, Au colloids have been combined with optical fibers, resulting in the detection of streptavidin with nanoparticles attached to the core, [122] or to the end-face, [123] of the fibers. The wide range possibilities of LSPR are probably best illustrated by examples of extreme sensor miniaturization, reaching levels of single nanoparticle biosensors. In this regard, single spherical colloidal

nanoparticles, attached to a glass substrate and spectrally interrogated via dark-field (DF) microscopy, have been employed to study the interaction of biotin and streptavidin. [124] This sensing concept has been extensively exploited, using a great variety of plasmonic nanostructures, of which the use of single Au nanorods can be highlighted. [125] In this work, problems regarding the proper biofunctionalization of non-spherical nanoparticles is circumvented by covering the immobilized nanorods with lipid bilayers to probe the interaction between biotin and streptavidin.

Besides applications based on the immobilization of colloidal nanoparticles on supporting substrates, multiple applications that employ lithographically nanostructured substrates have been reported. Among them, biotinylated silver triangular nanoparticles fabricated with NSL have been used to detect streptavidin, [126] and anti-biotin, [127] resulting in a LOD of 1 pM and 1 nM, respectively. Modification of these particle surfaces with mannose monosaccharide allowed for the real-time monitoring of concanavalin A, [128] comparing the obtained results to those of conventional SPP sensors. In the association phase, both LSPR and SPP sensing platforms presented comparable signals. However, in the dissociation phase, the SPP sensor showed a $5\times$ higher signal variation, being directly caused by the characteristic decay length of the EM fields that intervene in the sensing process. For the nanotriangles, the size of the sensing region is of the same order as the size of the binding molecules, which makes them less sensitive to non-specifically linked molecules. Furthermore, NSL-based substrates, used to study the interaction of molecules that are possibly involved in Alzheimer disease, can be highlighted. To this end, the interaction of amyloid-derived diffusible ligand (ADDL) antigen and its specific antibody was probed either directly or via a sandwich immunoassay. [129] Also, gold capped nanoparticle layer substrates have been utilized to detect DNA hybridization, [107] and antigen-antibody immunoreactions. [130] Interestingly, this substrate formed the basis of a multiarray nanochip composed of 300 sensing spots, for the detection of antigen-antibody reactions, exemplifying the possibilities of LSPR sensors for multiplexing and high throughput analyses. [131]

Other attractive metal nanostructures for biosensing applications are nanoholes in metal layers. These nanostructures combine the properties of SPPs in metal layers with the LSPR created by the nanohole features. [132] For optically thick metal layers, ordered distributions of nanoholes give rise to extraordinary optical transmission phenomena. [133] As for metal nanoparticles, the local increment of RI near the nanoholes induce a red-shift in the transmission spectrum.

The proof-of-principle of this sensing scheme has been demonstrated with the

detection of alkanethiol chains and protein monolayers in arrays of nanoholes, [111, 118] and nanoslits, [134] fabricated in thick gold and silver films, respectively. Conversely, nanoholes in thin metal layers show optical features that resemble nanoparticle LSPRs, thereby resulting in red-shifted resonance peaks as the nanohole size or the surrounding RI increase. In this regard, nanoholes fabricated with CL in thin gold films (20 nm) have been used for refractometric sensing applications. [135, 136] Interestingly, the preference of supported phospholipid bilayers (SPB) formation on silicon based substrates rather than on metal surfaces has been exploited to induce the rupture of phospholipid vesicles in the bottom of the nanometric holes. This self-assembled process enabled the detection of biochemical interactions located exclusively in the nanoholes, where the LSPR-induced EM field enhancement is maximized, yielding 16-fold higher sensitivity compared to detection on the Au surface. Furthermore, even biosensing applications with single nanoholes has been demonstrated. [136]

1.4.4.2 Other LSPR Sensing Approaches

The field of nanoplasmonic biosensing is not exclusively limited to refractometric sensing applications. Promoted by their optical properties, the use of metal nanoparticles in other sensing applications has been devised. In this section, we provide a brief review of these other LSPR-based sensing approaches.

- **Colorimetric LSPR sensors**

LSPR-based colorimetric sensors find their basis in drastic color changes triggered by nanoparticle aggregation: for two nanoparticles, when the polarization is parallel to the dimer axis, the LSPR peak red-shifts as the interparticle distance diminishes, and blue-shifts for perpendicular polarization. [109] This color change is induced by EM near field coupling. Thus, if two sets of metal nanoparticles are functionalized with complementary biomolecules, the biochemical interaction will induce the aggregation of the nanoparticles, the latter being easily detectable through the color change of the aggregate (Figure 1.17). [137]

- **Nanoparticles as Labels**

The bright colors associated with metal nanoparticles turn them into ideal candidates as labels to report and image biochemical interactions (Figure 1.18). [138, 139] The scattering flux from a single 80 nm metal nanoparticle is comparable to that of $5 \cdot 10^6$ fluorescence molecules, and is $105 \times$ larger than

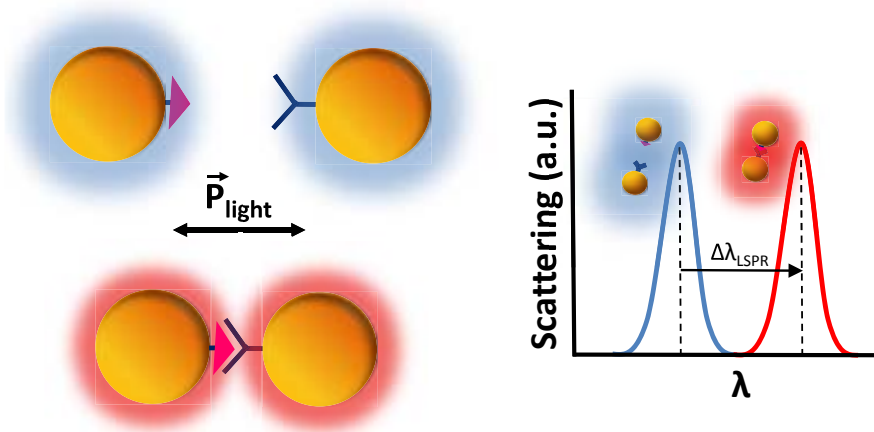


Figure 1.17: Schematic representation of and LSPR biosensor based on the aggregation of metal nanoparticles.

that of a single quantum dot (QD). [140] Furthermore, metal nanoparticles can easily be visualized using DF microscopy, they do not suffer from photobleaching and they can be easily bioconjugated. Therefore, nanoplasmonic particles profile themselves as serious alternatives to conventional fluorescence or chemiluminescence labels.

- **Surface Enhanced Effects**

The large EM energy enhancements induced by SPRs in metal surfaces and nanostructures can be applied to amplify the signal of other analytical techniques, as in SPP biosensing, fluorescence or Raman scattering.

- **Sensitivity Enhancement in SPP Sensors**

Metal nanoparticles can be used as an efficient amplification method for the biosensing response in conventional SPP sensors. Driven by the EM coupling between the nanoparticles' LSPR and the SPP of the metal film, immobilization of colloidal Au nanoparticles on evaporated Au films results in a large spectral shift of the surface plasmon, broader resonance peaks and an increase of the reflectance minimum. [141]

- **Surface Enhanced Raman Scattering**

Raman Scattering (RS) is an inelastic optical phenomenon caused by the excitation of molecular vibrational modes. This vibrational spectroscopy

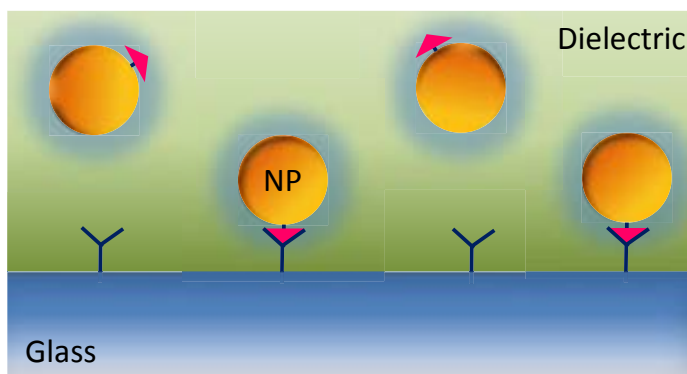


Figure 1.18: Schematic representation of a biosensing assay where metal nanoparticles are used as labels.

requires high power lasers and long acquisition times due to the very low RS cross-section of the molecules of interest. The Raman cross-section is around 10^{-30} cm^{-2} , that is, approximately 14 orders of magnitude smaller than that of fluorescence molecules. Higher Raman signals and lower acquisition times can be achieved by taking advantage of the extremely intense EM field generated by the LSPR of nanostructured metals, giving rise to Surface Enhanced Raman Scattering (SERS). SERS enhancement factors scale approximately as the 4th power of the local field EM enhancement, [142] emphasizing the importance of the EM coupling between metal nanostructures for this process. Typically, SERS enhancements in ensembles of molecules approximates 8 to 9 orders of magnitude, although enhancements as high as 15 orders of magnitude can be reached in special configurations. This dramatic enhancement of the Raman cross section can lead to single-molecule sensitivity detections. [143–145]

– Surface Enhanced Fluorescence or Quenching

Fluorescence labeling is a valuable technique in biochemistry, being an essential tool in DNA sequencing and hybridization detection and immunosensing. Also, quenching, Resonant Energy Transfer (RET) and anisotropic emission of fluorophores have been useful to detect certain biochemical groups in macromolecules. Interestingly, these properties can be drastically modified in the presence of metals, thereby enabling quenching, fluorescence intensity enhancements, changes in radiative decay

rates and alterations of their spatial emission pattern. These effects are usually referred to as Surface Enhanced Fluorescence (SEF) or Radiative Decay Engineering, and constitute a very active area in plasmonics for biosensing or cell imaging. Changing the emission properties of fluorophores in the vicinity of a metal surface strongly depends on their distance to the surface (d). For short distances ($d=0-5$ nm), the dominant effect is quenching due to the Forster Energy Transfer (FET) from the fluorophore to the SPR in the metal. This effect decreases with d^3 to the surface. However, for larger distances ($d=5-20$ nm), the fluorescence intensity can be increased (SEF). [146] SEF stems from two effects, being the local EM field enhancement induced by SPPs or LSPRs, and the increase of the fluorophores' radiative decay rate. Both effects combined can lead to fluorescence enhancements as high as $109\times$. [147] Both quenching and SEF can be employed in biosensing and bioimaging applications.

- **Photothermal Effects, Phototherapy and Drug Delivery**

Finally, a nanoparticle LSPR, can induce important thermal effects that are able to cause particle reshaping. This thermal effect forms the basis of an interesting photothermal interference contrast method used to image single metal nanoparticles in cells. [148] This selective photo-induced heating and the possibility to conjugate metal nanoparticles to specific targets makes them also very valuable for photothermal therapeutic medicine. The first hyperthermal therapy application used gold nanoshells to take advantage of their large absorption cross section and resonance in the NIR, where tissue is transparent, [149], while exploitation of the scattering properties of the nanoshells can be used to image the cells under consideration. [150] These photothermal properties can also be exploited for selective drug delivery. [151]

Chapter 2

Materials and Methods

Herein, we discuss all materials and methods that have been used throughout all the experimental and theoretical work, whose results are presented in this manuscript. This information includes details on the sample fabrication, experimental measuring techniques, bulk and surface sensitivity measurements which have been used to assess the refractometric sensing performance of the employed SPP and LSPR biosensing schemes and information regarding the different types of simulations that were carried out.

2.1 Sample Fabrication

First, all the details regarding sample fabrication are presented, including the synthesis of Au nanorods, and the fabrication of short-ordered arrays Au nanodisks, via implementation of HCL.

2.1.1 Nanorod Synthesis

Au nanorods were prepared following the Ag^+ assisted methodology as proposed by *Nikoobakht et al.* [91] and modified by *Liu et al.* [152] Briefly, first a Au seed solution was prepared by borohydride reduction of 5 mL 0.25 mM HAuCl_4 in an aqueous 0.1 M CTAB solution. For the synthesis of the Au nanorods, 24 μL of seed solution was added to a growth solution containing 0.1 M CTAB, 0.5 mM HAuCl_4 , 0.75 mM ascorbic acid, 0.12 mM Ag nitrate and in the presence or the absence of 0.019 M HCl. The nanorods, thus synthesized, have an average length, width and AR of 72.1 ± 10.2 , 19.0 ± 2.9 , and 3.86 ± 0.77 nm (I), and 46.15 ± 5.54 , 14.78 ± 1.42 , and 3.15 ± 0.49 nm (II), and 53.0 ± 8.1 , 21.3 ± 3.1 , and 2.52 ± 0.46 nm (III), respectively.¹ The UV-VIS spectra of the 3 obtained Au nanorod solutions are shown in Figure 2.1A, Figure 2.1B and Figure 2.1C, exhibiting long-axis LSPRs at $\lambda_{\text{LSPR}} \approx 839$ nm (I), $\lambda_{\text{LSPR}} \approx 751$ nm (II) and $\lambda_{\text{LSPR}} \approx 687$ nm (III), respectively. A Transmission Electron Microscopy (TEM) image of glass-supported Au nanorods of sample II is shown in Figure 2.1D.

In order to attach the Au nanorods to a solid support, they were electrostatically attached to SiO_2 cover slips (Menzel-Gläser, nr.1). Briefly, after cleaning the cover slips in a freshly prepared piranha solution (3:1 H_2SO_4 : H_2O_2) during 20 min, they were incubated for 2 min in a 2 wt % poly(diallyldimethylammonium chloride) (PDDA) (Sigma-Aldrich, 409030-1L, $M_w = 400\text{k}-500\text{k}$) solution, followed by extensive H_2O rinsing, yielding the formation of a PDDA monolayer on top of the glass slide. Strongly diluted solutions (1000-10000 x) of the Au nanorods with varying ARs and coated with poly(sodium 4-styrenesulfonate) (PSS) were then drop-coated during 30 s on the oppositely charged PDDA covered SiO_2 cover slip, in order to assure both single nanoparticle discrimination and electrostatic binding to the substrate. Subsequently, the samples were placed in an ozone generator for 10 min, to remove all the remaining organic compounds. Finally, a new PDDA monolayer was deposited for stability purposes, following the same drop-coating process as described above.

¹The nanorods were synthesized as part of an established scientific collaboration by the Colloid Chemistry Group, lead by Prof. L. M. Liz-Marzán, belonging to the University of Vigo (Spain).

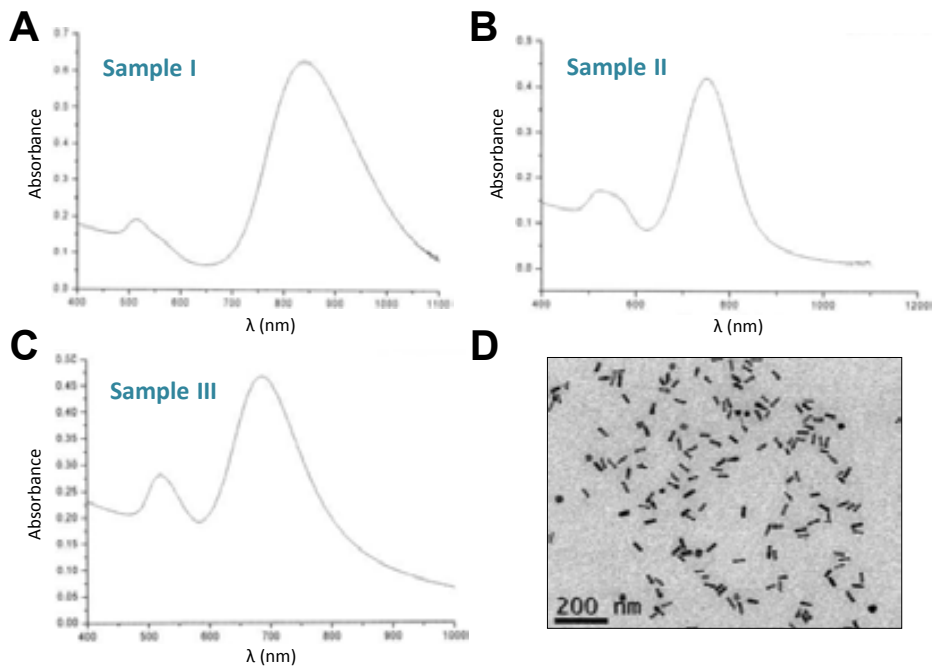


Figure 2.1: UV-Visible spectra of colloidal nanorod solutions (A) I ($\lambda_{LSPR} \approx 839$ nm), (B) II ($\lambda_{LSPR} \approx 751$ nm) and (C) III ($\lambda_{LSPR} \approx 687$ nm), next to (D) a TEM image of sample II.

2.1.2 Hole-Mask Colloidal Lithography

Short-ordered arrays of Au nanodisks (Diameter ≈ 100 nm, Height ≈ 20 nm) were fabricated by HCL. [153] First, SiO₂ substrates (Menzel-Gläser, nr.4) were cleaned, by placing them 20 min in a freshly prepared piranha solution (3:1 H₂SO₄/H₂O₂). After drying the SiO₂ substrates with N₂, they were ready for the HCL process that resulted in the creation of the Au nanodisk-patterned substrates. The exact details of this lithographic process are described by the following 4 steps.

1. Polystyrene Bead Deposition

First, an approximately 200 nm thick layer of 950K PMMA (4% in Anisole) was spin-coated on the clean SiO₂ substrates (4000 rpm, 1500 r·s⁻²). After a 5 min baking process at a temperature superior to 150°C, the PMMA covered SiO₂ substrates were subjected to a short O₂ plasma (10 s, 75 W, 75 mTorr and a 20% O₂-flux) in order to increase the hydrophilicity of the PMMA. Then, oppositely charged polyelectrolyte was dropcoated on top of the PMMA layer in order

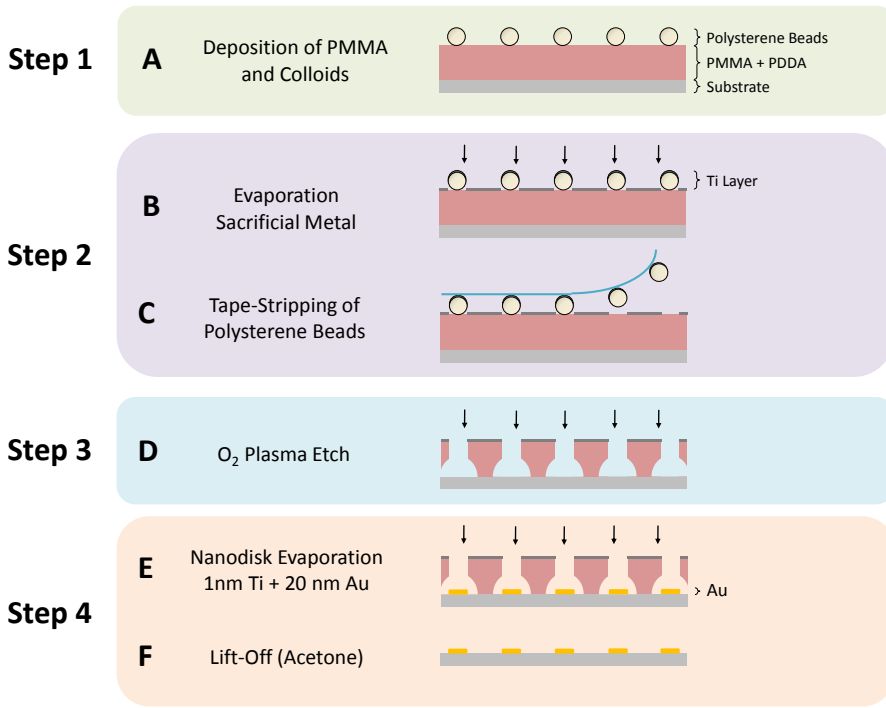


Figure 2.2: Schematics depicting the 4 steps of the hole-mask colloidal lithography process. These steps include (A) the polymer (PMMA and PDDA) deposition for the adhesion of polystyrene beads, (B) the evaporation of a sacrificial metal layer, (C) the tape-stripping process of the polystyrene beads, (D) an oxygen plasma etch for the creation of holes in the polymer layer, (E), the evaporation of the metal adhesion layer and the Au (typically 20 nm), and finally, (F) the removal of the remaining hole mask by a lift-off process in acetone.

create an adhesive layer on top of the latter. For this purpose, a 0.2 wt.% PDDA (Sigma-Aldrich, 409030-1L, $M_W = 400k-500k$) was used (60 s incubation time), after which the sample was thoroughly rinsed with H₂O and dried with N₂. As a last step, a colloidal solution containing polystyrene beads (Invitrogen, S37204, $D \approx 100$ nm, 0.2 w/v%) was deposited, by a similar dropcoating process (60 s incubation), subsequently rinsing and drying the substrate with H₂O and N₂, respectively. The electrostatic repulsion between the polystyrene beads, in combination with the attractive force that exists between these spheres and the PDDA layer, define a short-range ordered polystyrene particle array. A schematic 2D drawing depicting the final result is shown in Figure 2.2A.

2. Creation Hole-Mask Template

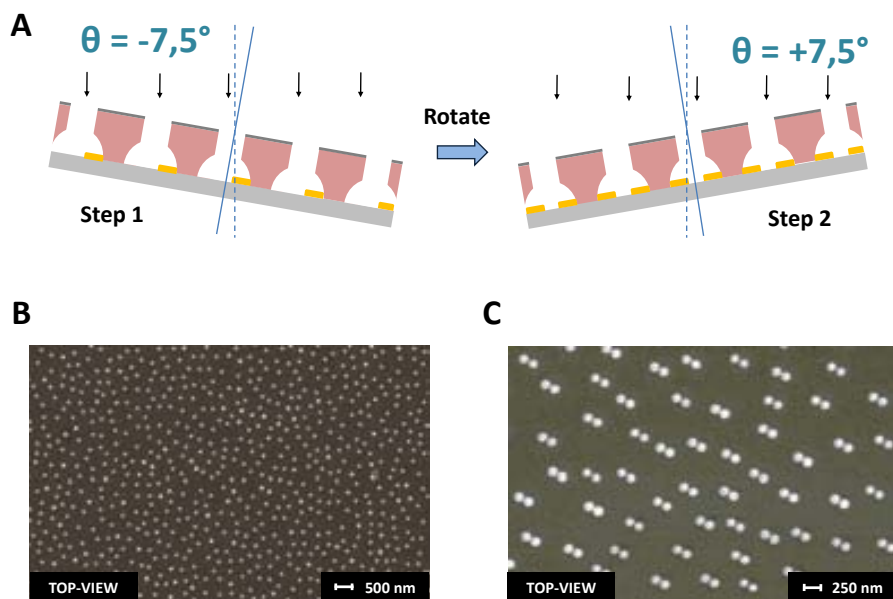


Figure 2.3: (A) Schematics representing the two-step fabrication process of short-ordered arrays of nanodisk dimers, fabricated via hole-mask colloidal lithography. SEM images of typical short-ordered arrays of nanodisks or nanodimers are shown in subpanels (B) and (C), respectively.

As a second step, the hole-mask template is created by first depositing a sacrificial layer of a material that is resistive to O_2 plasma treatments. In our case, we opted for the electron-beam deposition 15 nm of Ti (Figure 2.2B). Secondly, the polystyrene beads are tape-stripped away, as shown in Figure 2.2C, leaving a sacrificial PMMA layer with a perforated Ti hole-mask on top.

3. Oxygen Plasma Treatment

Next, an O_2 plasma treatment (180 s, 75 W, 75 mTorr and a 20% O_2 -flux) is applied in order to remove the exposed polymer (PMMA/PDDA) underneath the holes that are perforated in the sacrificial Ti layer. The etching selectivity of the PMMA and Ti, and ion backscattering (over-exposure) result in *under-cut* features as schematically depicted in Figure 2.2D.

4. Disk Evaporation and Lift-Off

As a final step, the resulting hole-mask is used as a deposition mask for the resulting Au nanodisks. Using electron-beam metal deposition, first the metal adhesion layer is deposited. Depending on the specific requirements, Ti or Cr was used for this purpose. These adhesion layers had a height of 1 or 2 nm, evaporated at $0.5 \text{ \AA}\cdot\text{s}^{-1}$. Next, a 19 or 20 nm thick Au film was evaporated at $1.0 \text{ \AA}\cdot\text{s}^{-1}$, creating the resulting Au nanodisks (Figure 2.2E). Subsequently, the remainder of the hole-mask was removed by a lift-off process, carried out in acetone at ambient temperature. It should be noted that the undercut-features caused by the O_2 plasma treatment facilitate the lift-off process. The final result is a nanostructured SiO_2 surface with 19 or 20 nm high Au nanodisks, attached to the surface by a 1 or 2 nm thick adhesion layer (Ti or Cr), as shown in Figure 2.2F. Note that the nanodisk diameters (and its corresponding diameter size distribution) and interdisk spacings are entirely governed by the properties of colloidal polystyrene bead solution. A typical top-view Scanning Electron Microscopy (SEM) image of a short-ordered array of Au nanodisks is shown in Figure 2.3B.

As a final procedure, before use, the nanodisk samples were cleaned by consecutive 1 min sonication-cycles in acetone, ethanol and deionized H_2O ($2 \times$), after which the samples were blown dry with N_2 . The samples were then placed in an ozone generator for 20 min, after which they were thoroughly rinsed with de-ionized H_2O and dried with N_2 .

2.1.2.1 Disk-Density Variations

For the creation of short-ordered arrays of Au nanodisks with varying nanodisk densities (F), a few changes were applied to the lithographic process described in Section 2.1.2. To this end, the single 0.2 wt.% PDDA monolayer was expanded with a PSS/diallyldimethylammonium chloride (DDA) bilayer, prior to the drop-coating of the polystyrene beads. To this end, first a 2 wt.% PSS solution (Sigma-Aldrich, 243051-100G, $M_W = 70\text{k}$) was dropcoated (1 min incubation) on top of the PDDA. Then, DDA (Sigma-Aldrich, 348279-1L, $M_W = 7\text{k}$) with v/v ratios ranging from 1.5% to 3% was drop-coated (1 min incubation) on top of the PDDA/PSS bilayer. The addition of DDA at various concentrations assures varying values of F, once the oppositely charged polystyrene beads are drop-coated in a subsequent step, thereby following again the same protocol as described in Section 2.1.2.

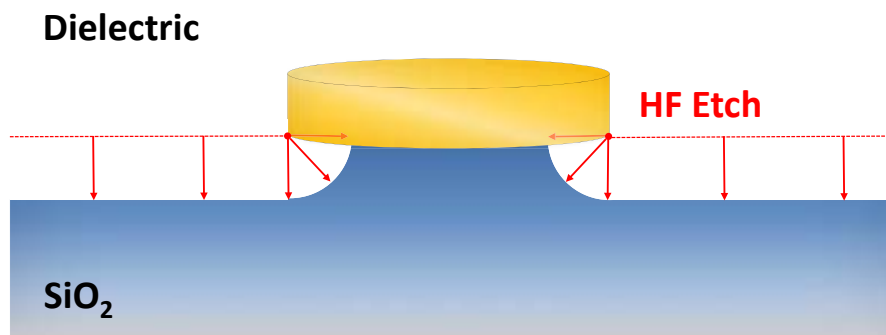


Figure 2.4: Schematic representation of a single Au nanodisk, supported by a dielectric pillar.

2.1.2.2 Au Nanodisk Dimers

Also for the creation of short-range ordered arrays of Au nanodisk dimers, small changes were applied to the experimental HCL fabrication procedure described in Section 2.1.2. In this case, the final metal evaporation step, such as depicted in Figure 2.2E, is replaced by the following 2-step process. As schematically depicted in Figure 2.3A, the nanodisk dimers are fabricated by carrying out metal deposition at two different, mirrored rotation angles (θ) of the sample with respect its normal axis. The values of θ can then be used as a variable to precisely tune the interparticle separation distance. In our specific case, a $\theta = 15^\circ$ resulted in interparticle distances of approximately 30 nm. A SEM image of such a short-ordered array of dimers is depicted in Figure 2.3C.

2.1.2.3 Pillar-supported Nanodisks

Pillar-supported Au nanodisks, of which a schematic representation is shown in Figure 2.4, were created by etching away the SiO₂ underneath the nanodisks in a controlled and isotropic manner. For this, a strongly diluted solution (0.05%) of hydrofluoric acid (HF) was employed. Since gold is not affected by direct contact with HF, the nanodisks function as a mask for a controlled etching process of the exposed SiO₂. Given the isotropic nature of this process, the resulting supported nanodisks exhibit mushroom-like geometries as shown in Figure 2.4. The creation of these dielectric nanopillars can be either performed via the in-flow injection of HF into the flow cell or via an ex-situ protocol, the latter consisting of a time-controlled immersion of nanodisk substrate into the acidic solution, thereby obtaining similar

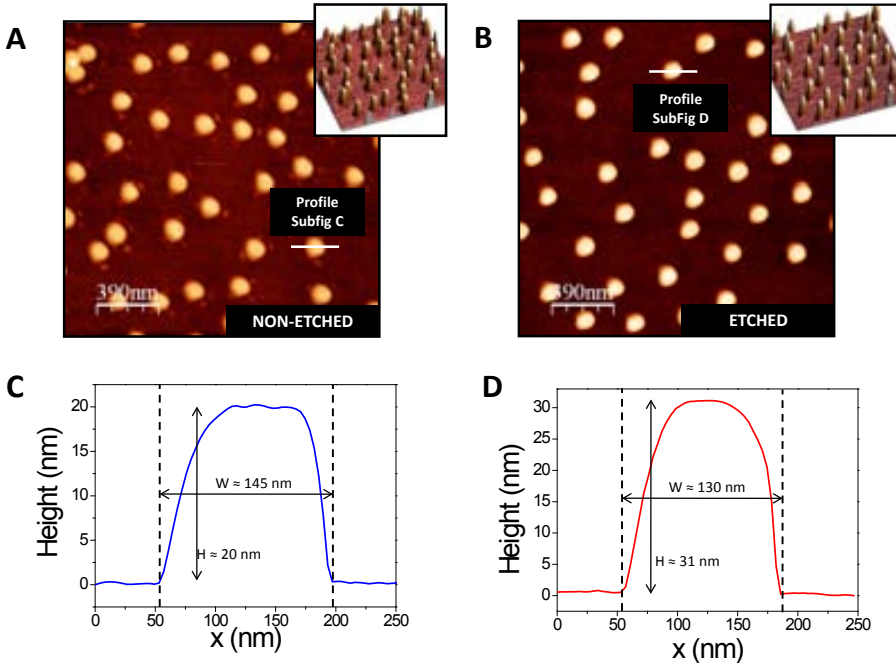


Figure 2.5: Topological AFM images of non-suspended (A) and suspended (B) short-ordered arrays of gold nanodisks, together with the corresponding height profiles for non-etched (C) and etched (D) samples.

results.

The latter ex-situ etching process is nicely illustrated when analyzing the AFM images that were recorded for both non-etched and etched nanodisk substrates, as shown in Figures 2.5A and 2.5B, respectively (For further details on the employed AFM instrumentation, we refer to Section 2.2.4). Also, Figures 2.5C (non-etched) and 2.5D (etched) show typical nanodisk height profiles, extracted from the data represented in Figures 2.5A and 2.5B, respectively. As expected, non-etched nanodisk substrates exhibit a height of approximately 20 nm, that is, the originally intended height of the Au nanodisks. On the other hand, nanodisks who experienced 10 min HF etch show a height difference of approximately 31 nm with respect to the glass substrate, yielding an isotropic etching distance of approximately 11 nm. One can also observe similar nanodisk distributions in both nanodisk substrates, indicating that the etching process is non-destructive as long as the etch distance is small enough to prevent nanodisk instability. The finite size of the AFM tip causes geometric

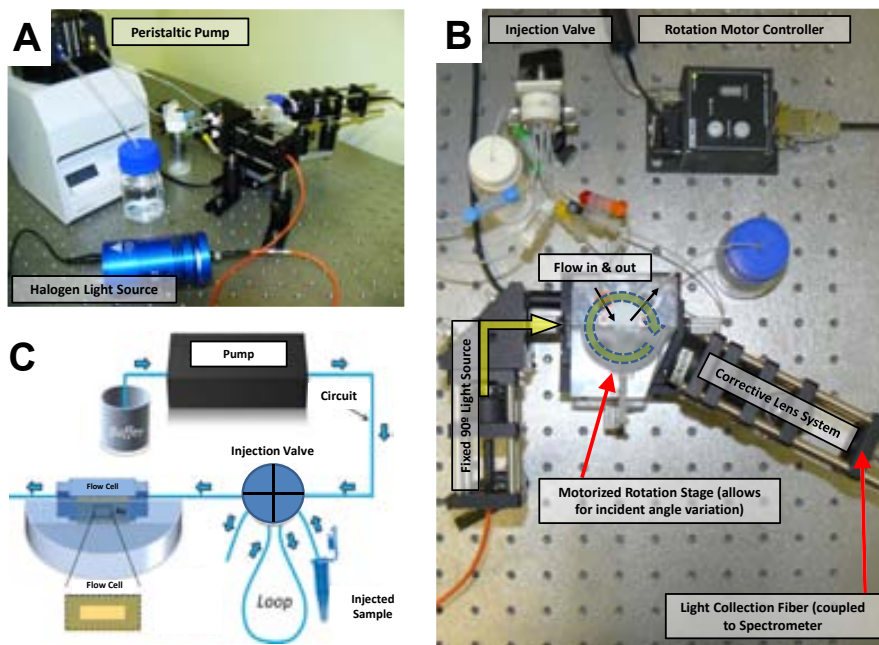


Figure 2.6: (A) Bird-view and (B) Top-view photographs of the employed SPP sensor pointing out the components of the experimental setup, together with (C) schematics representing the fluidics of the system.

convolution, thereby distorting the original diameter of the nanodisks ($D = 100 \text{ nm}$) to larger values. Either way, the smaller widths obtained for the etched nanodisks ($W = 130 \text{ nm}$ vs. $W = 145 \text{ nm}$) could point toward a re-shaping process of the nanodisks when underlying SiO_2 is etched away.

2.2 Experimental Measuring Schemes

This section discusses all the employed measurement techniques and provides the necessary details concerning the experimental setups that were implemented.

2.2.1 SPP Biosensor

Commercial Au substrates ($50 \pm 2 \text{ nm Au}$, $1.5 \pm 0.3 \text{ nm Ti}$) were clamped between a custom-made flow cell (Volume $\approx 4 \mu\text{L}$) and a hemi-cylindrical glass prism that contacted to the backside of the Au substrate via RI matching oil ($n \approx 1.515$) in

order to assure a Kretschmann configuration. This part of the setup was mounted on a motorized rotary plate, allowing the system to rotate with respect to a fixed halogen light source (HL-2000, Mikropack), such that the incidence angle of the collimated incoming TM polarized light could be varied. A corrective lens system, rotating along the same axis, was used to collect the reflected light leaving the prism with a multi-mode optical fiber, with a diameter (\varnothing_F) given by $400\ \mu\text{m}$. Finally, a spectrometer (Shamrock SR-303i, Andor) connected to a cooled CCD detector (Newton, Andor) was used to analyze the collected light, as depicted in Figure 2.8B. A peristaltic pump with adjustable pumping speed was used to assure a constant liquid flow through the microfluidics, thereby passing through a manual injection valve and the flow cell. Bird-view and top-view photographs of this system are depicted in Figure 2.6A and 2.6B, together with schematics representing the fluidics of this SPP sensing platform (Figure 2.6C). The exposure time of the SPP spectra was set to 10 ms. The Au substrates were cleaned before use, by immersing them during 5 min in a freshly prepared piranha solution (3:1 $\text{H}_2\text{SO}_4/\text{H}_2\text{O}_2$).

2.2.2 Single Particle Spectroscopy

DF microscopy in transmission mode offers a very reliable technique for the acquisition of elastic scattering spectra of single nanoparticles. This experimental method operates in a very similar way as a conventional microscope. The difference is hidden in the use of a DF condenser, which is placed between the excitation light source and the sample, as shown in the schematics of Figure 2.7 for an inverted microscope geometry. The idea behind this technique is to detect only the scattered light coming from a single nanoparticle against a dark background, the latter being accomplished by inhibiting the excitation light to reach the light collection objective. This is done via the mediated use of a DF condenser. In order to accomplish this, excitation and collection angles have to be chosen very carefully. Angles are typically defined by their Numerical Aperture (N.A.), defined as $\text{N.A.} = \sin(\theta) \cdot n$, in which θ is the incidence angle of the light with respect to the optical axis and n is the RI of the medium through which the light propagates. In order to ensure that no excitation light enters the collection objective, θ must be larger than the light collection angle, i.e. the N.A. of the DF condenser must be larger than the N.A. of the objective employed for the collection of the scattered light coming from the nanostructure. By meeting this requirement, the DF condenser blocks all the incoming light angles that otherwise would travel right into the objective.

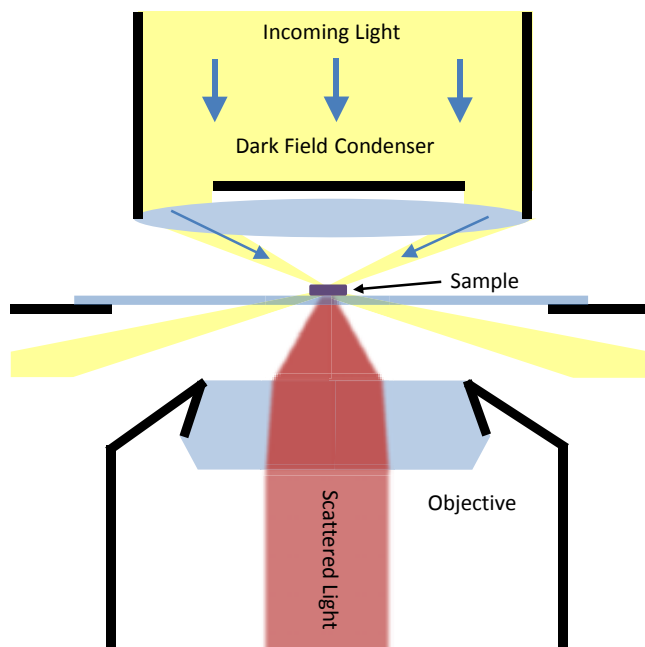


Figure 2.7: Schematic drawing of an inverted dark-field transmission spectroscopy setup.

In our approach, we employed an inverted Nikon inspection microscope (Eclipse Ti-U, Figure 2.8A), equipped with a halogen light source (100 W) and fiber-coupled ($\varnothing_F = 400 \mu\text{m}$) to a CCD-cooled spectrometer (Shamrock SR-303i, Andor, Figure 2.8B), was utilized to obtain the elastic scattering spectra of single Au nanorods by means of DF microscopy. Two different DF condensers (Dry N.A. 0.90-0.80 and Oil N.A. 1.43-1.20, Nikon), in combination with a $100\times$ oil immersion objective (Plan Fluor $100\times$ N.A. 0.5-1.3 Oil, Nikon) were employed to collect light scattered by single Au nanorods. A custom-made Teflon flow cell (Figure 2.8C), sealed by two SiO_2 cover slips (the underlying cover slip contained the immobilized nanorods), and possessing in- and outlets that serve as connections for the fluidics was employed to carry out the sensitivity measurements. A peristaltic pump with adjustable pumping speed was used to assure a constant liquid flow through the microfluidics, thereby passing through a (manually operated) injection valve and the flow cell. A schematic drawing of the experimental setup, containing all the major components, can be observed in Figure 2.8C. All acquired scattering spectra of single Au nanorods presented in this work were taken with a total accumulation time of 60 s. An example of a CCD DF image of Au nanorods immobilized on a SiO_2 substrate can be observed in Figure 2.8D.

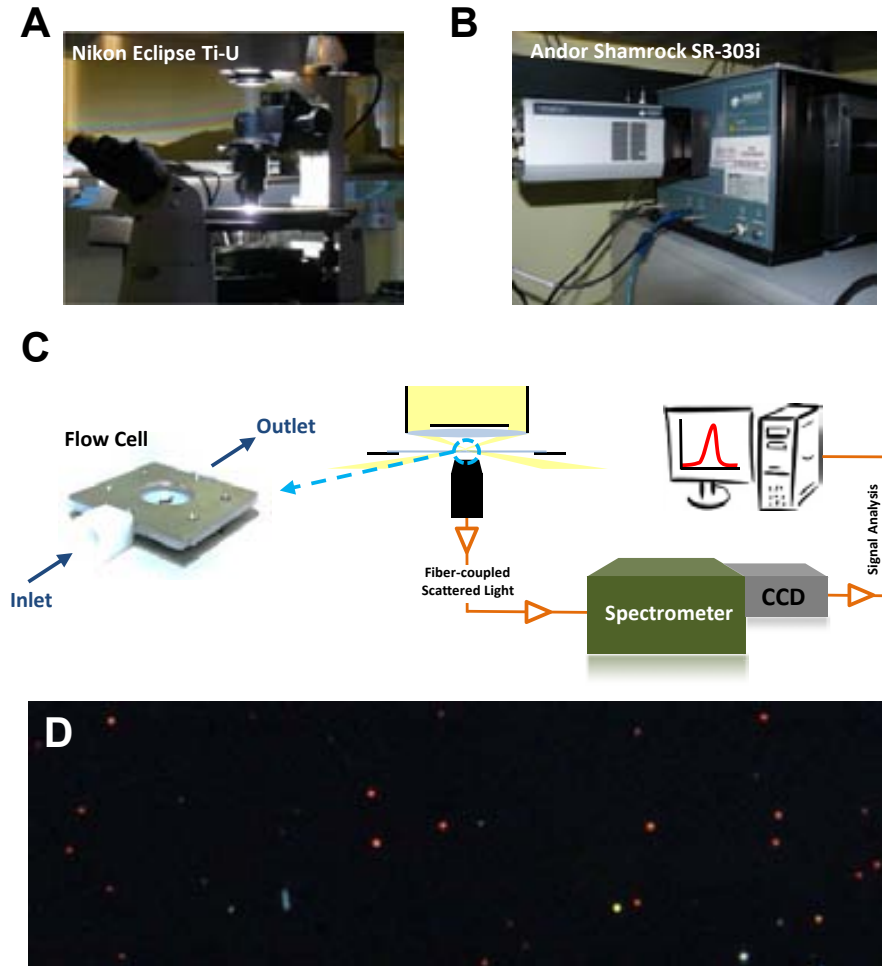


Figure 2.8: (A) Photograph of an inverted Nikon Eclipse Ti-U microscope for DF microscopy measurements. (B) Photograph of a Shamrock SR-303i Andor CCD-cooled spectrometer. (C) Schematics representing the employed experimental DF measurement configuration. (D) Dark field CCD image of Au nanorods immobilized on a glass substrate.

In this photograph, every colored dot represents the light scattered by an individual Au nanorod.

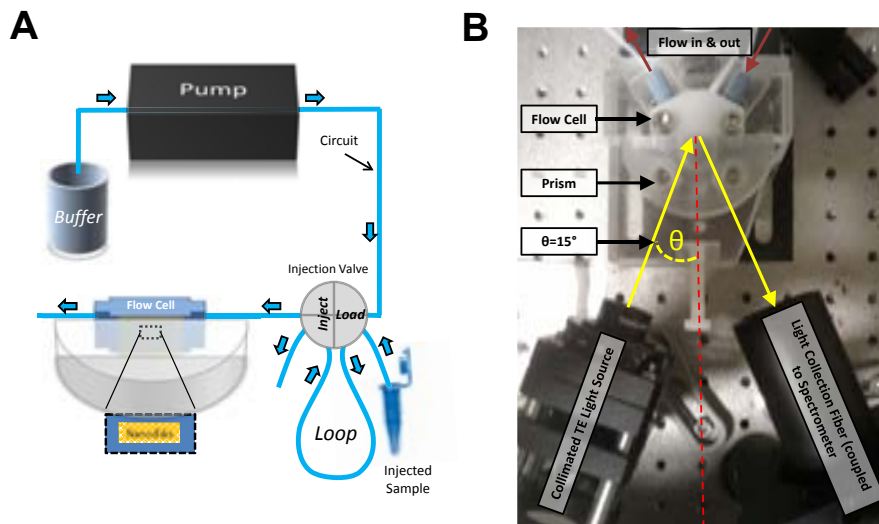


Figure 2.9: (A) Schematic representation of the microfluidics employed in the fixed angle LSPR excitation setup, together with (B) a top-view photograph of this experimental measuring scheme.

2.2.3 LSPR Reflection Measurements

2.2.3.1 Fixed Angle Measurements (Chapter 4)

The LSPR of the short-range ordered arrays of Au nanodisks was excited by a transverse-electric (TE) polarized collimated halogen light source (HL-2000, Micro-pack), reaching the nanodisks through a hemi-cylindrical glass prism (K9, $n \approx 1.512$), contacting the sample via RI matching oil ($n \approx 1.512$). From the other side, the nanodisk samples were clamped by a custom-made Delrin flow cell (Volume = 4 μL). LSPR excitation was achieved at $\theta = 15^\circ$. Spectral analysis of the reflected light was carried out with a CCD-cooled spectrometer (Andor Shamrock SR-303i, T = -60°C) that can be observed in Figure 2.8B. For this, the reflected light was collected with a collection lens (Thorlabs, F230SMA-B) and guided to the spectrometer via a multi-mode fiber ($\varnothing_F = 400 \mu\text{m}$). LSPR spectra (2 ms exposure time) were accumulated every 3 s (1500 spectral accumulations). A syringe pump (New Era, NE-1000) with adjustable pumping speed was used to assure a constant liquid flow through the microfluidics, thereby passing through a manually operated injection valve (IDEX Health and Science, V-451) and the flow cell. A schematic representation of the employed microfluidics can be observed in Figure 2.9A. A photograph of

this measurement setup, comprising all of its major components can be observed in Figure 2.9B. Extraction of the spectral LSPR peak position as a function of time was done after the measurements were finished, using a high-degree polynomial fit. [154] To this end, the commercially available Wolfram Mathematica software package was used. Standard deviations were calculated using measurement data collected during the first 400 s of the experiment.

2.2.3.2 Multi-angle Measurements (Chapter 5)

Reflectivity spectra of short-range ordered arrays of Au nanodisks were obtained by exciting them with a collimated halogen light source (HL-2000, Micropack), reaching the substrate via a hemicylindrical glass prism (K9, $n \approx 1.512$) that contacts the nanodisk sample through RI matching oil ($n \approx 1.512$). Depending on the experiment, TE or TM polarized light was used. The samples were comprised between the prism and a custom-made flow cell (Delrin, Volume = 4 μl). Both incident and reflected optical paths were mounted on arms rotating around the center point of the flow cell, guaranteeing the ability to carry out θ -dependent analyses. A syringe pump (New Era, NE-1000) with adjustable pumping speed was used to assure a constant liquid flow through the microfluidics, thereby passing through a manually operated injection valve (IDEX Health and Science, V-451) and the flow cell. For all measurements, the employed microfluidic system was identical as the one described in section 2.2.3.1, whose schematic representation is shown in Figure 2.9A. The reflected light was collected by a collection lens (Thorlabs, F230SMA-B) and fiber-coupled ($\varnothing_F = 400 \mu\text{m}$) to a low-cost, USB-powered CCD spectrometer (Ocean Optics, Spectrasuite Jaz Module). Reflectivity spectra were acquired every 3 ms, with a total integration time of 900 ms (300 spectral accumulations). All spectra were normalized with a broad-band reference spectrum, obtained in TIR using the same acquisition settings. Extraction of the spectral LSPR peak position as a function of time was done after the measurements were finished, using a high-degree polynomial fit. [154] To this end, the commercially available Wolfram Mathematica software package was used. For simultaneous measurements at both low ($\theta = 20^\circ$) and high ($\theta = 75^\circ$) excitation angles, a second excitation was used, as depicted in Figure 2.10. In this measurement setup, two identical excitation and light collection paths are employed, each mounted at its corresponding θ -value. Both optical paths are mounted in such a way that the same white light illumination intensity is assured. Logically, also identical acquisition conditions (exposure time 3 ms and 300 spectral accumulations) were used, using two different USB-powered CCD spectrometers (Ocean Optics, Spectrasuite Jaz Module).

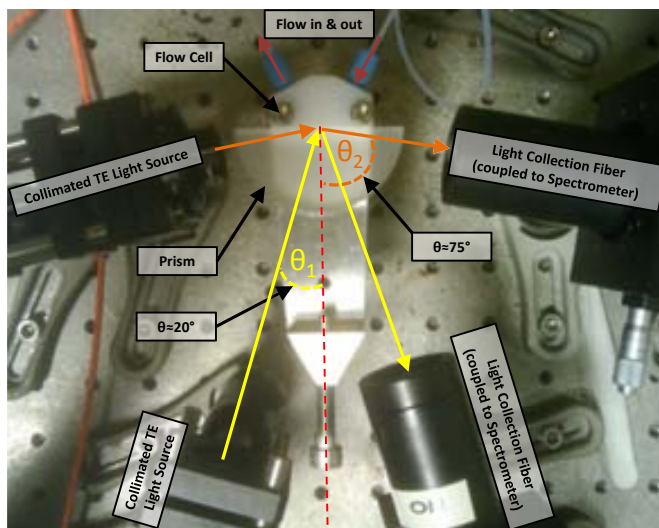


Figure 2.10: Top-view photograph an LSPR excitation setup that allows for simultaneous measurements at two different incidence angles, given by $\theta = 20^\circ$ and $\theta = 75^\circ$.

2.2.4 Atomic Force Microscopy

The AFM images were recorded on an Agilent 5500 AFM/SPM microscope in tapping mode. A multi-purpose low-coherence scanner with scan range up to $90 \mu\text{m}$ was used for imaging samples under ambient conditions. The AFM probes were NSC15-type silicon pointprobes (force constant 30-50 N/m, resonant frequency 330 KHz) from MikroMasch. Image processing and rendering was done with the opensource WSxM software package.

2.3 Details on Bulk Sensing Experiments

In this section we specify the details of the bulk sensitivity (η_B) studies that were carried out to test the bulk sensing performance of different refractometric SPP and LSPR sensors. In all experiments η_B was tested by injecting a previously prepared solution with a different RI and comparing the induced spectral resonance shift with respect to the initial spectral position of the resonance in H_2O ($n \approx 1.3325$). All solutions were injected into the microfluidics system of the employed SPP and/or LSPR sensing platforms at a pumping speed of $20 \mu\text{L}\cdot\text{min}^{-1}$. In the case if multiple

Table 2.1: Data table showing the experimental details concerning the employed bulk sensitivity measurements.

| Chapter | Plasmonic Substrate | Solution Type | Solution RI |
|----------|------------------------------------|------------------|-------------------------------|
| 3 | Au film (SPP) Single Rod (LSPR) | Saline Buffers | $n \approx 1.3325$ - 1.3415 |
| 4 | Nanodisks ¹ (LSPR) | Glycerol (12.8%) | $n \approx 1.3525$ |
| 5 | Nanodisks (LSPR) | Glycerol (12.8%) | $n \approx 1.3525$ |

¹Real-time monitorization of the isotropic etching process of the SiO₂ substrate was carried out via the injection of 0.05% HF. After each injection of HF, η_B was measured.

RI solutions, η_B was extracted from the slope of linear fits through the obtained data points ($\Delta\lambda_{\text{SPR}}$ vs. RI). All presented values of η_B are averaged over two separate, independent measurements. Temporal monitorization of the spectral peak position revealed that all resonance peaks were blue-shifted back to their initial spectral position after the injected samples passed through the flow cells. Further details regarding all η_B experiments carried out in this work are displayed in Table 2.1

2.4 Details on Surface Sensing Experiments

Here, we provide details regarding the different experimental approaches that we used to characterize the surface sensing performance of different plasmonic and nanoplasmonic biosensors. These experimental methods include the deposition of oppositely charged polyelectrolyte layers, DNA hybridization measurements and a Carb/Anti-Carb immunoassay.

2.4.1 Deposition of Polyelectrolyte Monolayers

Making use of electrostatic affinity of the positively charged PDDA to both negatively charged Au, SiO₂ and PSS, subsequent injection (Loop Volume $\approx 300 \mu\text{L}$) of PDDA

and PSS resulted in the in-flow formation of polyelectrolyte multilayers on top of the Au/SiO₂ substrate. To this end, 2 wt% solutions of PDDA (Sigma-Aldrich, 522376-1L, M_W = 7k) and PSS (Sigma-Aldrich, 243051-100G, M_W = 70k) in H₂O were subsequently injected at a pumping speed of 20 μL·min⁻¹.

2.4.2 DNA Hybridization Measurements

Nanodisks supported by dielectric pillars were obtained through an ex-situ immersion of a nanodisk sample for 10 min in 0.05% HF, after which the sample was thoroughly rinsed with deionized H₂O and dried with N₂. Immobilization of the 24-mer thiolated DNA probes on the surface of the suspended and non-suspended nanodisks was done employing an overnight incubation protocol in which the nanodisk surfaces were covered with a droplet (Volume = 40 μl) of 2 μM thiolated DNA, diluted in a 750 mM NaCl, 50 mM phosphate buffer at pH 7. DNA hybridization measurements were carried out using a saline 750 mM NaCl, 75 mM Sodium-Citrate buffer at pH 7. The 32-mer single stand DNA target contained a sequence of 24 bases complementary to the immobilized DNA receptor. DNA dehybridization was carried out using a 35% formamide solution. All measurements were carried out at a constant flow of 20 μL·min⁻¹.

2.4.3 Carb/Anti-Carb Immunoassay

A clean Au nanodisk surface was biofunctionalized under a constant flow of deionized H₂O at 20 μL·min⁻¹. Both the exposed SiO₂ and the Au nanodisks were modified with carboxylic groups by injecting a 0.5% solution of carboxyethylsilanetriol sodium salt (CTES, Gelest Ltd., UK) in distilled H₂O followed by a solution of a carboxy- and thiol-terminated compound that contains 4 units of ethylene glycol (PEG) (CO₂H-EG-SH, 100 M in 5 mM Carbonate Buffer). A derivative of the pesticide carbaryl conjugated to a carrier protein (Carb-BSA) was covalently attached to the carboxylic groups by means of the well-known carbodiimide reaction. First a mixture of 1-ethyl-3-(3 dimethylamino-propyl) carbodiimide hydrochloride (EDC) and N-hydroxysuccinimide (NHS), EDC/NHS (0.2 M / 0.05 M in MES Buffer) was injected in order to activate the carboxylic groups, followed by Carb-BSA (20 μg·mL⁻¹ in PBS) allowing for the free amino groups present in the conjugate to react. All remaining unreacted NHS-activated esters were deactivated by blocking the modified surface with ethanolamine (1 M, pH 8.5). Detection of specific antibody against carbaryl (monoclonal antibody Anti-carb) at different concentrations (0.25 - 3 μg·mL⁻¹) was

carried out using PBS as interaction buffer. Regeneration of the bioactive surface was achieved by injecting a basic 100 mM NaOH solution for 30 s.

2.5 Theoretical Simulations

This section describes all the details concerning the simulations, whose results are presented in this work.

2.5.1 Optical Constants

Throughout all simulations, optical constants of Au reported by Johnson and Christy were used. [75] Modeling of the Ti and Cr adhesion layers was carried out using optical constants retrieved from Weber. [155]

2.5.2 SPP Simulations

In order to model SPP based sensors, a transfer matrix formalism was employed to calculate the reflectivity of a TM polarized EM wave impinging at the sensing substrate at a single incidence angle, [156] using glass as incident medium, (Kretschmann configuration [56], $n = 1.52$), a 1.5 nm titanium sticking layer with a 50 nm Au layer on top, and H_2O as the sensing medium ($n = 1.33$). The surface sensitivity (η_S) was modeled by coating the metal layer with a 1 nm thick dielectric layer ($n = 1.5$). A schematic representation of the precise simulation geometry can be observed in Figure 2.11A. The bulk sensitivity was normalized by dividing the difference in peak position with the difference in RI. η_S -Values were evaluated by comparing the spectral peak positions with and without the modeled coating layer on top of the substrate. Full-width half-maximum (FWHM) values were measured at a peak intensity exactly at the middle of the peak maximum and peak minimum.

2.5.3 Single Particle LSPR Simulations

In order to characterize the optical and sensing properties of single nanostructures, two different theoretical methodologies were employed, being the quasi-static MLWA and more rigorous finite-difference time-domain (FDTD) calculations. Both techniques are discussed hereafter.

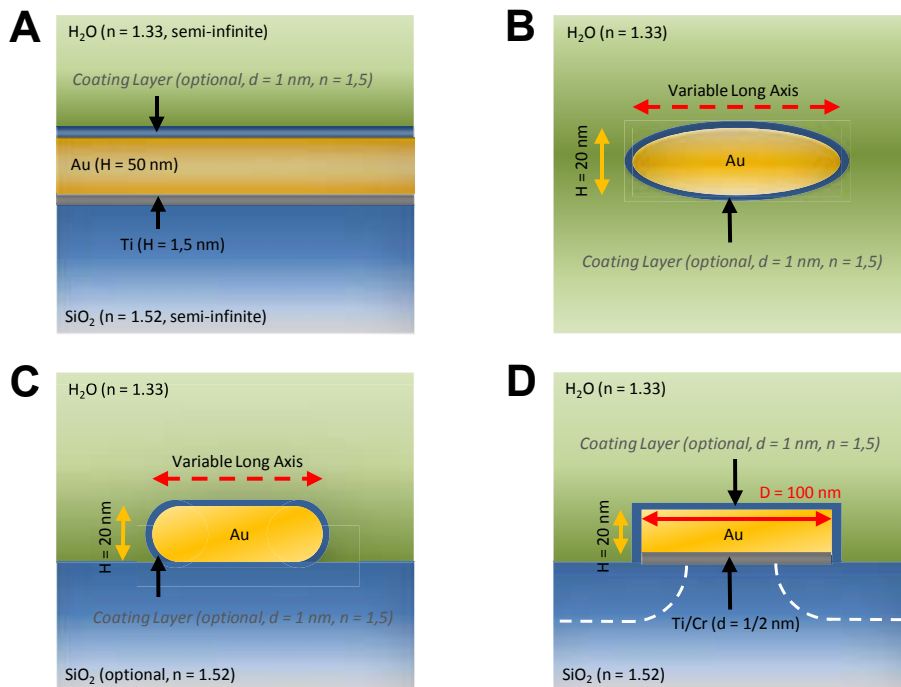


Figure 2.11: Schematic drawings representing the simulations that assess the sensing performances of (A) SPP sensors, (B) single Au nanoellipsoids (MLWA), (C) single Au nanorods (FDTD) and (D) single Au nanodisks (FDTD).

2.5.3.1 Quasi-static MLWA Calculations

Nanorods were modeled as if it were prolate spheroids surrounded by a homogeneous dielectric. Interaction of these rod-shaped nanoparticles with light was investigated through implementation of quasi-static theory, compliant with the MLWA approach, whose precise details are discussed in Section 1.4.1 for spherical and ellipsoidal nanoparticles. Analytic expressions for the polarization of these ellipsoidal particle geometries are given in Sections 1.4.1 and 1.4.2 for non-coated and coated nanoellipsoids, respectively. Using the AR of the particle as a variable, while maintaining the two short-axes of the particle at 10 nm (Cross-sectional diameter = 20 nm), we were able to spectrally tune the wavelength of the LSPR. The bulk sensitivity was measured by comparing the spectral LSPR shifts as a function of the induced RI change. This quantity was calculated by dividing the induced spectral shift by the relative RI change ($\Delta n = 0.02$). The surface sensitivity was modeled by coating

the nanoellipsoid with a 1 nm thick dielectric layer ($n = 1.5$). Then, the surface sensitivity was evaluated by comparing the spectral peak positions in the situation with and without the modeled coating layer. FWHM values were measured at a peak intensity exactly at the middle of the peak maximum and peak minimum. A schematic representation that illustrates this theoretical approach is displayed in Figure 2.11B.

2.5.3.2 FDTD Calculations

The FDTD is a theoretical calculation method that solves the Maxwell equations for complex geometries, whose optical properties lack of an analytical solutions. [157] FDTD calculations allow its user to solve the Maxwell equations in both linear and non-linear dispersive media, providing complete freedom when it comes to the choice of geometries and excitation sources. As its name indicates, the FDTD method is a time domain technique, meaning that all EM fields are solved as a function of time. Typically, this is done by the hand of Fourier transforms as a function of frequency or wavelength that are carried out during the simulation. Being both a direct time and space solution, this method is extremely valuable for all types of simulations that investigate the interaction of EM waves with metals.

- **Single Gold Nanorods - Chapter 3**

FDTD scattering spectra of single Au nanorods were calculated via the commercially available Lumerical Software Package. Single nanorods were modeled as cylinders capped by hemi-spheres. A mesh size of 2 nm was employed for the bulk sensitivity calculations in a homogeneous dielectric medium, whereas a 0.5 nm mesh size was used to model the surface sensitivity of the nanorods and in the calculations that tested the influence of a supporting glass substrate. The width of the nanorods was fixed at 20 nm. Only the longitudinal plasmon resonance of Au nanorods was calculated by setting the electric field of the plane wave parallel to the longitudinal direction of the Au nanorods. To investigate substrate effects, an edge of the nanorod was contacted to a modeled substrate ($n = 1.52$). For surface sensitivity simulations of the rods in the presence of a substrate, the overlapping part of the dielectric coating with the substrate was overridden by the substrate. After calculation, the positions of the resonance peaks in the scattering spectra were determined. Values corresponding to η_B and η_S were obtained as described in Section 2.5.3.1. A schematic representation that clarifies these calculations is depicted in Figure 2.11C.

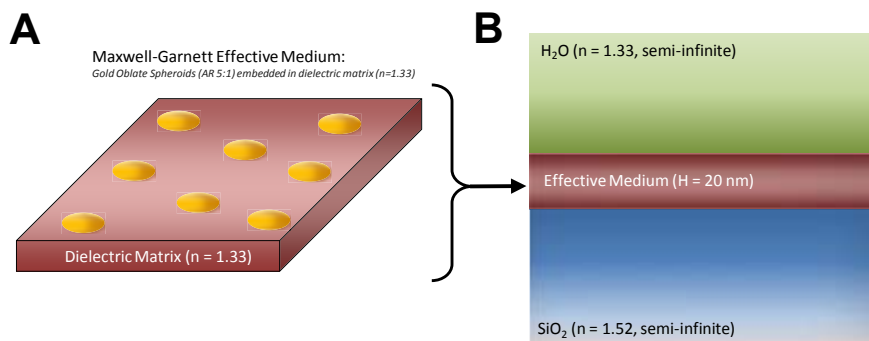


Figure 2.12: Schematics of (A) the modeled Maxwell-Garnett effective medium, showing Au oblate spheroids in a homogeneous dielectric matrix ($n = 1.33$) and (B) the multilayer configuration for the calculation of reflection coefficients of the Maxwell-Garnett effective medium.

• Single Gold Nanodisks - Chapter 5

FDTD scattering spectra and EM field profiles of single Au nanodisks were calculated via the commercially available Lumerical Software Package. Nanostructures were modeled as Au nanodisks (Diameter = 100 nm, Height = 20 nm) attached to the substrate by a Ti or Cr adhesion layer (Thickness = 1-2 nm), resembling the nanostructures used in the experiments. Typically, the substrate supporting the nanodisks resembled SiO₂ ($n = 1.52$). However, to elucidate the adverse effect of the substrate high RI on the sensing performance of nanodisks, the RI was varied between $n = 1.52$ and $n = 2.4$. The RI of the dielectric environment surrounding the nanodisks was set at $n = 1.33$, close to the RI of typical aqueous buffer solutions. Isotropic HF etches of the underlying glass substrate were simulated through the creation of dielectric pillars underneath the disks, with sizes corresponding to different etch-times. EM field profiles were calculated with a 0.5 nm mesh accuracy, whereas for the generation of typical scattering spectra a grid size of 1 nm was used. Schematics that exemplify these calculations are shown in Figure 2.11D.

2.5.4 Maxwell-Garnett Effective Medium

Optical properties of the sparse arrays of nanodisks were simulated using the Maxwell-Garnett (MG) effective medium approximation, modeling the nanodisks as infinitely small oblate spheroids (AR = 5:1) embedded in a homogeneous dielectric ($n = 1.33$)

using different disk densities ($F=2-10\%$), as schematically depicted in Figure 2.12A. [158] For the angle- and polarization-dependent reflectivity spectra a transfer matrix formalism was employed, such as described in Section 2.5.2, comprising the effective medium, with a thickness 20 nm, between two cladding layers (SiO_2 , $n = 1.52$ and H_2O , $n = 1.33$). The latter configuration is schematically represented in Figure 2.12B. Values corresponding to η_B were determined by inducing a RI change of $\Delta n = 5 \cdot 10^{-3}$ with respect to the RI of H_2O ($n = 1.33$). Dispersion relation and mode propagation distances were calculated via an analytical formalism to determine the waveguiding properties of planar anisotropic multilayers. [72, 159]

Sensing Performance Comparison: Single Particle LSPR vs. SPP Sensor

Herein, a theoretical and experimental study is presented, that discusses the refractometric sensing performance of plasmonic gold-based sensors involving both conventional thin film SPP sensing platforms and LSPR sensors formed by single nanorods. Exploitation of the spectral tunability of both systems, allowed for the assessment of their bulk and surface sensing performances. This is done by means of a general figure of merit parameter, revealing the existence of an optimized spectral region where the surface sensing performance of both sensors is optimized, which can be attributed to the optical properties of the employed material. In good agreement with theoretical predictions, it is shown that, although the SPP sensor offers a much better bulk sensitivity, the LSPR sensor exhibits an approximately 15% better performance for surface sensitivity measurements when its figure of merit (FOM) is optimized. However, optimization of the substrate refractive index and the accessibility of the relevant molecules to the nanoparticles can lead to a total 3-fold improvement of the FOM in LSPR sensors.

3.1 Introduction

As discussed in Chapter 1, refractometric plasmonic sensors exploit their SPR to detect small RI changes in close proximity to the sensing surface, the latter being formed by a plasmonic material that finds itself in contact with a dielectric. When this interface is planar, the plasmon can propagate in the form of an oscillating charge wave and is referred to as a SPP. Sensors based on SPPs have been intensively studied and their use in medical diagnostics, environmental monitoring, food quality and safety analysis has been reported even using real samples. Since they offer attractive properties such as real-time and label-free detection, SPP biosensors have profiled themselves as the most widely employed and commercialized optical biosensors (Section 1.3.2).

Contrary to an SPP, an LSPR is a type of SPR excited on a sub-wavelength plasmonic nanostructure. As emphasized in the preceding chapters, the LSPR excitation condition is strongly affected by the composition, size, shape and the surrounding dielectric environment of the considered nanostructure, the latter being the factor on which the sensing capabilities of nanoparticles rely. Typically, the LSPR energies of metal nanostructures are located in the visible or near-infrared regions of the EM spectrum, and their resonantly enhanced extinction cross sections are sufficiently high to allow imaging and optical characterization of single particles by means of DF spectroscopy, resulting in peak-shaped spectral responses. Boosted by the possibilities that such measurements offer for miniaturization and multiplexing, LSPR based sensing has attracted the interest of many researchers over the last decade. [10, 11]

Although both SPP and LSPR sensing platforms offer specific advantages, their performance is mainly evaluated through their capability to detect changes in the monitored quantity (RI), which ultimately determines the sensitivity η of the sensor. As both sensing schemes are generally characterized by a peak-shaped response, η can be defined as the shift of the peak position P_{SPR} upon dielectric changes in the environment, where P_{SPR} will be either the wavelength position λ_{SPR} or the energy position E_{SPR} of the resonance. When taking biosensing considerations into account, it should be noted that, typically, the EM fields used as sensing probes in SPP and LSPR detection penetrate deeper into the dielectric than the usual layer thicknesses of adsorbed biomolecules. For the propagating plasmon, this effect is much more pronounced, with decay lengths varying between 100 and 500 nm, [160] whereas for a single nanorod, according to our simulations, as will be shown later on in this chapter

(Figure 3.3), the sensitivity of the nanostructure saturates at a distance between 50 nm and 80 nm from the particle's surface, depending on the particle geometry. Therefore, distinction has to be made between bulk RI changes and local changes very close to the sensing surface. [161] In terms of η , this means that the bulk sensitivity η_B can be expressed as the variation of P_{SPR} per bulk RI (n_B) unit change:

$$\eta_B = \frac{P_{SPR}}{n_B} \quad (3.1)$$

On the other hand, the surface sensitivity η_S can be characterized as the P_{SPR} shift with respect to the thickness variation of an assembled thin dielectric layer with thickness d on top of the sensing substrate:

$$\eta_S = \frac{P_{SPR}}{d} \quad (3.2)$$

A second factor affecting the sensing performance of the sensor is its resolving precision to detect changes of the monitored quantity. This parameter is typically represented by the FWHM of the resonance peak: a sharp peak facilitates the registration of a peak shift and *vice versa*.

Therefore, when considering the performance of a sensor, it is necessary to evaluate both sensitivity and peak width. A good example supporting this statement, is the bulk sensitivity of LSPR based sensors with the same geometry: analysis in wavelength scale reveals that whereas this quantity increases linearly when the resonance is red-shifted, [77] the peak width follows the same trend, [162] and therefore a trade-off is required to determine the optimized sensing region. A FOM, defined as

$$FOM = \frac{\eta}{FWHM} \quad (3.3)$$

correlates both quantities and can be used to quantify the general performance of a sensor and to allow comparison with that of other sensing schemes. [163] Also, the FOM neutralizes the controversy that may arise when comparing sensitivities and FWHM values in wavelength and energy scales, as we demonstrate here.

Theoretical and experimental studies on sensitivities of wavelength interrogated SPP sensors have been reported, [44] and this investigation has recently been extended to the field of nanoparticle based sensing platforms. [77, 161, 164, 165] In this chapter, we present a comparative theoretical and experimental analysis, involving the sensing features of wavelength interrogated SPP sensors and LSPR sensors based on single nanoparticles with rod-like geometry, with the aim of extracting a general trend,

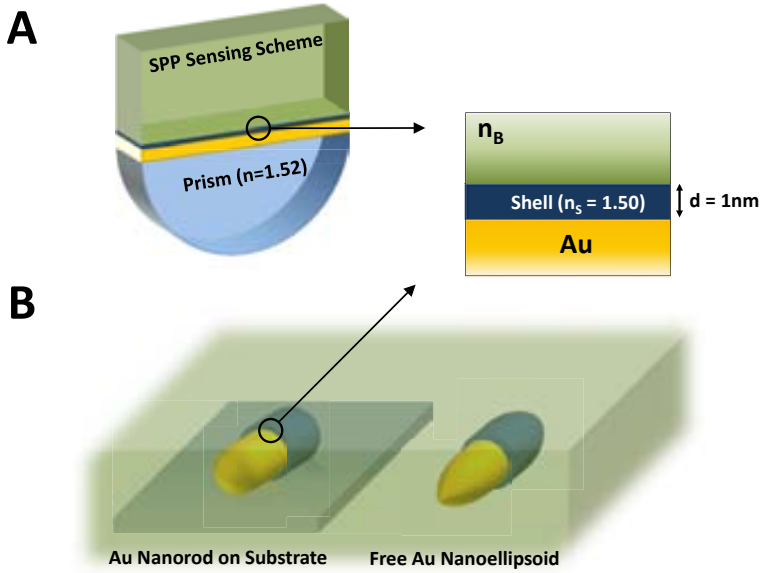


Figure 3.1: Schematic representation of both SPP (A) and LSPR (B) sensing schemes. The SPP Kretschmann setup consists of a gold sensing substrate, sandwiched between a prism and a bulk dielectric medium (n_B). Contrary, the LSPR sensing platform is modeled as a gold nanoellipsoid (MLWA) or a gold nanorod (FDTD) embedded in a dielectric environment (n_B). Surface sensitivity measurements are simulated by modeling a thin layer ($n_S=1.50$) over the sensing substrates of both sensor types.

valid for all plasmonic sensors. We take advantage of the spectral tunability of these systems to study their bulk and surface sensitivities as a function of plasmon resonance position. For both sensing schemes, we obtained FOMs for bulk and surface sensitivities, which reveal that the FOMs in wavelength and energy scales are equivalent and that an optimized surface sensing region can be established for plasmonic sensors, which can be ascribed to the intrinsic plasmonic spectral properties of gold. First, we discuss theoretical simulations regarding η_B and η_S , subsequently followed by an analysis involving the substrate effect on the sensitivity of immobilized nanorods. Next, we present the experimental results that confirm the theoretical findings. Again, the η_B results of both sensing schemes is discussed first, followed by the outcome of the measurements regarding η_S .

3.2 Simulations

The bulk and surface sensitivities for both SPP and LSPR based sensing methods were simulated according to the schematic models depicted in Figure 3.1. For the SPP sensors we considered a Kretschmann configuration with a glass prism ($n = 1.52$) and a sensing substrate composed of a 1.5 nm titanium sticking layer and a 50 nm gold layer, resembling the commercially obtained substrates used in the experiments (For further details, we refer to Section 2.5.2). On the other hand, for the LSPR analysis we simulated rod-like gold nanoparticles of different aspect ratios. The selection of this morphology was motivated by the wide spectral tunability of gold nanorods while keeping small particle volumes, thus minimizing dephasing effects. In this theoretical analysis, gold nanoparticles were modeled following two different approaches: firstly, an ellipsoidal geometry was assumed through implementation of a MLWA model which enabled us to analytically calculate the polarizability of these nanostructures (For further details, we refer to Section 2.5.3.1). Secondly, we accurately reproduced the experimental nanorod morphology as spherically capped cylinders and implemented it in a rigorous FDTD method, in which both the finite size of the particles and the effect of the substrate on the sensing performance of the particles are considered (For further details, we refer to Section 2.5.3.2). The peak positions of both sensing systems were spectrally tuned between 600 and 1000 nm by changing either the incidence angle (64° - 78°) of the incident light beam (SPP) or the AR (2-6) of the modeled nanorods (LSPR). In both sensing schemes, simulations of η_B were carried out by varying the RI of the surrounding dielectric, whereas η_S was tested by modeling the coating of a 1 nm thick uniform shell layer ($n_S = 1.50$) on the sensing substrate (see Figure 3.1). As previously mentioned, in FDTD the substrate ($n = 1.52$) was considered for both η_B and η_S simulations.

3.2.1 Bulk Sensitivity Comparison

Figure 3.2 summarizes the results obtained from the η_B simulations for both SPP and LSPR sensing schemes. The plots on the left-hand panel depict the normalized bulk sensitivity η_B , FWHM and the corresponding FOM values in wavelength scale as a function of peak position λ_{SPR} , while the graphs on the right-hand panel represent the same quantities, but converted to energy scale. When comparing the bulk sensing performance of both sensor types, analysis of η_B in terms of λ (Figure 3.2A) shows, for both configurations, a roughly linear increase as the peak position is red-shifted. This effect is due to the longer penetration of the EM field inside the dielectric at

longer resonant wavelengths, thus providing a larger volume that is sensitive toward RI changes.

In order to demonstrate this, the penetration depth of the evanescent field of a gold nanoellipsoid into the dielectric medium ($n = 1.33$) was calculated using MLWA simulations. To spectrally tune the values of λ_{SPR} , ARs of nanoellipsoids were varied between 2.5 and 5.5, maintaining the diameter of the short-axis fixed at 20 nm. This resulted in resonances ranging from $\lambda_{\text{SPR}} = 636$ nm (AR = 2.5) to $\lambda_{\text{SPR}} = 941$ nm (AR = 5.5). The nanoellipsoids were surrounded by a thin dielectric layer with

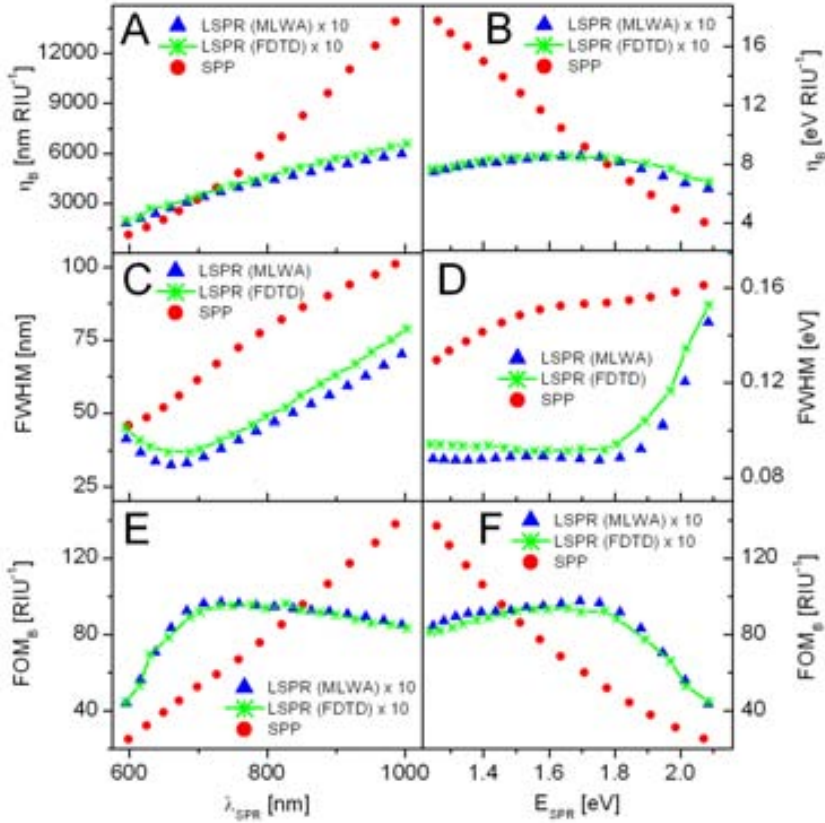


Figure 3.2: Calculated bulk sensitivity η_B , FWHM and the corresponding FOM for both SPP (red circles) and LSPR sensing platforms in wavelength (A,C,E) and energy (B,D,F) scales. For the LSPR based sensor, results obtained with both the MLWA (blue triangles) and the FDTD method (green crosses) are included. All data points are plotted as a function of the resonance wavelength (λ_{SPR}) and energy (E_{SPR}).

different refractive index ($n = 1.45$), whose thickness d_{Layer} was used as a variable to monitor the induced spectral shift $\Delta\lambda_{\text{SPR}}$ as a function of the thickness of this capping layer. The results of these calculations are shown in Figure 3.3, showing that for more red-shifted values of λ_{SPR} , that is, larger ARs, a larger spectral shift $\Delta\lambda_{\text{SPR}}$ is induced, demonstrating that at longer resonance wavelengths, the penetration depth of the EM field into the dielectric increases, yielding larger *sensing probes*. These results can be generalized and extrapolated to all other nanoplasmonic or plasmonic geometries.

Furthermore, as already stated Section 3.1, Figure 3.3 shows that the spectral shifts of the smallest nanoellipsoid ($\text{AR} = 2.5$) start saturating at a distance of approximately 20 nm from the particle surface, thereby putting a measure on the penetration depth of the EM field into the dielectric. For larger nanorods, this saturation initiates at somewhat larger distances from the gold surface, but it can be safely stated that the overall penetration depth of the EM field of the nanoellipsoids with resonances in the visible part of the EM spectrum is significantly smaller (approx. 20-30 nm depending on size) than those corresponding to propagating SPPs (100-500 nm). When going back to Figure 3.2A and 3.2B, it comes therefore as no surprise that

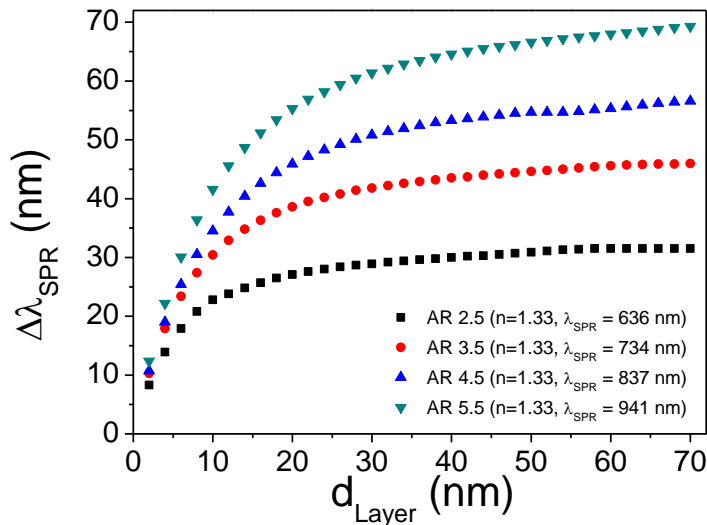


Figure 3.3: Calculated EM-field penetration depths of gold nanoellipsoids with varying aspect ratios, using the MLWA approximation.

comparison of η_B between both sensing schemes reveals that the calculated η_B values for SPP sensors is roughly one order of magnitude larger than that of their LSPR counterparts. For the LSPR, comparison of MLWA and FDTD methods shows that both the trends and obtained values for η_B , FWHM and FOM are approximately the same. Therefore, as long as the characteristic size of the nanoparticle is kept small compared to the wavelength of light and the nanoparticle is embedded in an homogeneous dielectric medium, the MLWA approach is justified and can be used to examine the sensing performance of these nanostructures, exploiting this method's much shorter calculation times compared to FDTD simulations.

However, if we compare sensitivity and FWHM values between wavelength and energy scales (Figures 3.2A-D), controversy may arise. For example, in the wavelength domain, the LSPR bulk sensitivity monotonically increases with λ_{SPR} , whereas in the energy plot the slope changes at $E_{SPR} \approx 1.75$ eV. When considering the FWHM, the observed trends are even more controversial. In this case, SPP sensors show larger values of FWHM for higher values of E_{SPR} , whereas wavelength representation suggests that lower resonance wavelengths are accompanied by narrower peaks. Also, for the LSPR sensing scheme, an abrupt FWHM increase is observed at a threshold value of $E_{SPR} \approx 1.8$ eV, whereas for smaller energies the peak width is more or less constant; this shows very little resemblance with the FWHM change in the wavelength scale. All this apparent controversy can be eliminated by using the FOM as the parameter of choice, since it can be mathematically demonstrated that the FOM in energy and wavelength domains are approximately equivalent, as demonstrated below. Starting out from the assumption that the FOMs is wavelength scale (FOM_λ), and in energy scale (FOM_E) are equivalent, this FOM-equivalence can be stated as:

$$FOM_E = \frac{\Delta E_{SPR}}{FWHM_E} = FOM_\lambda = \frac{\Delta \lambda_{SPR}}{FWHM_\lambda} \quad (3.4)$$

In this equation, ΔE_{SPR} and $\Delta \lambda_{SPR}$ are the induced spectral shifts in energy and wavelength scale, respectively, while $FWHM_E$ and $FWHM_\lambda$ are the corresponding FWHM values. Equation 3.4 can be rewritten as:

$$\frac{\Delta E_{SPR}}{\Delta \lambda_{SPR}} = \frac{FWHM_E}{FWHM_\lambda} \quad (3.5)$$

which when $\Delta \lambda_{SPR} \rightarrow 0$ reduces to:

$$\frac{E_{SPR}}{\lambda_{SPR}} = \frac{FWHM_E}{FWHM_\lambda} \quad (3.6)$$

Since E_{SPR} is given by:

$$E_{SPR} = \frac{\hbar c}{\lambda_{SPR}} \quad (3.7)$$

and by introducing the parameters $\lambda_1 = \lambda_{SPR} - a$ and $\lambda_2 = \lambda_{SPR} + a$ as shown in Figure 3.4, the FWHM can be expressed as $2 \cdot a$, equation 3.6 can be rewritten and worked out:

$$\begin{aligned} -\frac{\hbar c}{\lambda_{SPR}^2} &= \frac{\hbar c \cdot \left(\frac{1}{\lambda_2} - \frac{1}{\lambda_1} \right)}{\lambda_2 - \lambda_1} \\ &= \frac{\hbar c \cdot \left(\frac{\lambda_1 - \lambda_2}{\lambda_1 \cdot \lambda_2} \right)}{\lambda_2 - \lambda_1} \\ &= -\frac{\hbar c}{\lambda_1 \cdot \lambda_2} \\ &= -\frac{\hbar c}{\lambda_{SPR}^2 - a^2} \end{aligned} \quad (3.8)$$

This analytic derivation shows that FOM_E and FOM_λ are only equivalent if $a = 0$, that is, if a is small compared to the λ_{SPR} , which is the case for gold nanorods, since FWHM values are typically less than 10% of λ_{SPR} . This approximate FOM-equivalency is corroborated by the calculated results shown in Figure 3.2E and 3.2F. From these values we can see that the bulk FOM of SPP sensors is roughly one order of magnitude larger than that of LSPR sensors, even though the overall peak widths in the latter are substantially smaller. For SPP sensors, the bulk FOM exhibits a linear behavior, from which it can be deduced that the performance of this sensor improves at longer resonance wavelengths, i.e. lower excitation energies. In contrast, examination of the LSPR bulk FOM reveals a different trend, with the FOM showing a maximum located at $\lambda_{SPR} \approx 700$ nm, corresponding to $E_{SPR} \approx 1.75$ eV. Close to this value, the balance between sensitivity and resolution is maximized, resulting in an optimized sensing region. Note that from this point on, with FOM-equivalency established in energy and wavelength regimes, all figures displaying sensitivity, FWHM or FOM

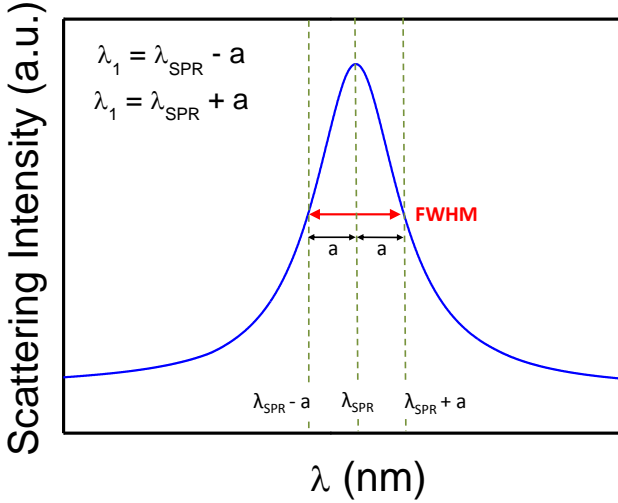


Figure 3.4: Redefinition of the FWHM of a resonance peak, introducing the parameters λ_1 and λ_2 , which are equally distanced from the resonance wavelength λ_{SPR} .

values, will be presented exclusively in wavelength scale.

3.2.2 Surface Sensitivity Comparison

From a biosensing point of view, η_{S} and its corresponding surface FOM are the relevant parameters to describe the sensing performance and, as shown in Figure 3.5, this can result in a very different behavior when compared to the η_{B} calculations. Examination of η_{S} shows that values of $\Delta\lambda_{\text{SPR}}$ for the analyzed wavelength range are larger than those calculated for the SPP configuration. For both sensor types, η_{S} consistently increases as λ_{SPR} is red-shifted, though also in both cases the slope gets smaller at longer λ_{SPR} . Again, because the evanescent field has an increased penetration depth into the dielectric at longer λ_{SPR} , the EM field is expected to be less confined near the surface, yielding a sensitivity decrease. Due to the higher η_{S} values and lower peak widths obtained for the LSPR sensors, their FOM values are typically higher than those of their SPP counterparts. As in the bulk sensitivity simulations, the surface FOM of the LSPR sensor displays a maximum, again located at $\lambda_{\text{SPR}} \approx 700$ nm. However, for the SPP sensor, the FOM values increase as λ_{SPR} is red-shifted, though signs of saturation become apparent for wavelengths above

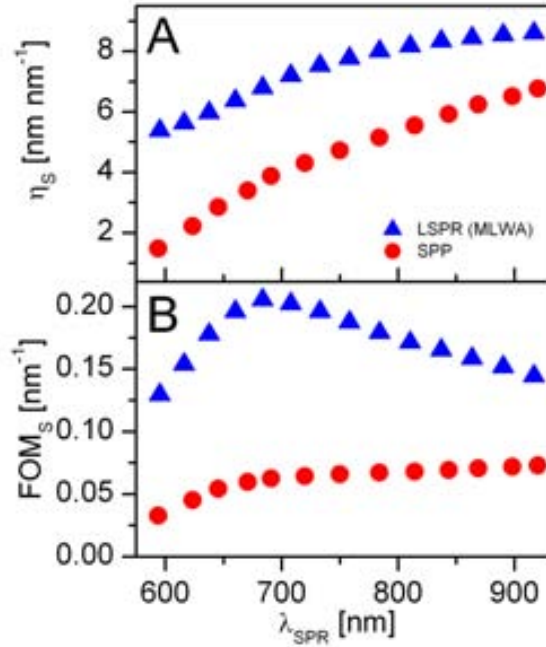


Figure 3.5: Calculated surface sensitivities η_s (A) and the corresponding FOMs (B) for the SPP (red circles) and the LSPR (blue triangles for MLWA and green stars for FDTD) sensing platforms as a function of spectral position of resonant wavelength λ_{SPR} .

$\lambda_{\text{SPR}} \approx 700$ nm. When comparing the FOM maxima of both sensing schemes, a 3-fold increase in surface FOM was found for the LSPR sensor, reflecting the stronger confinement of the EM field around the plasmonic nanostructures.

From these bulk and surface sensitivity calculations, we can conclude that, although superior bulk sensing performance was found for the SPP device, a better surface sensing performance is expected for the LSPR based sensing platform. Furthermore, the observed maximum surface FOM values suggest the existence of an optim

3.2.3 Impact of Substrate RI on LSPR Sensing Performance

So far we considered metal nanoparticles surrounded by a uniform dielectric medium and homogeneously coated with a thin dielectric layer. However, for practical biosensing applications, attachment of the nanoparticles to a solid substrate is required, thus allowing in-flow assays, kinetic analysis, surface regeneration and

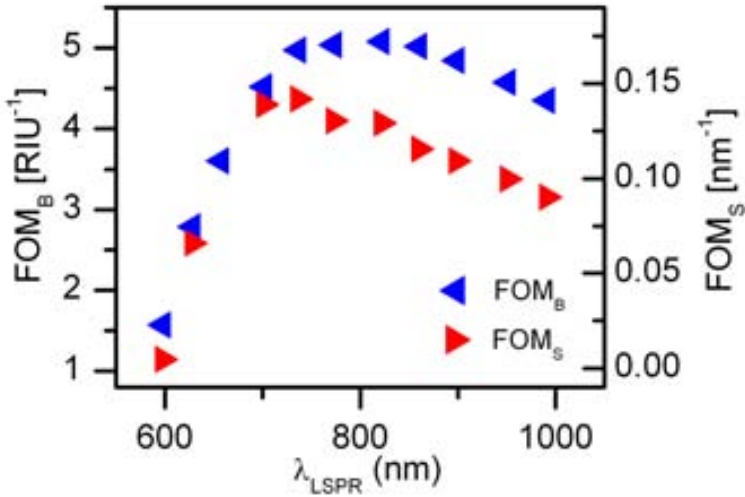


Figure 3.6: FDTD Calculated bulk and surface FOMs of a single nanorod modeled on top of a glass substrate.

multiplexing. The substrate, which generally has a higher RI than the sensing environment (the solvent), can significantly hinder the sensing performance of the nanoparticles. To identify and quantify the effect of the substrate on the performance of the LSPR based sensing scheme, we carried out FDTD calculations of the bulk and surface sensitivities of single gold nanorods lying on top of a silica substrate ($n = 1.52$). For the surface sensitivity simulations, only the part of the nanorod contacting the substrate was excluded from the modeling of a 1 nm thick layer ($n = 1.50$), assuring a total surface coverage that exceeds 95%. The resulting bulk and surface FOMs are displayed in Figure 3.6. Although the observed trends for the FOM remain unchanged, the bulk sensitivity shows that, indeed, the actual calculated values are significantly lower as compared to those obtained for particles entirely surrounded by a homogeneous dielectric medium, resulting in a 40% decrease of the bulk sensitivity FOM. However, in the case of surface sensitivity FOM, the FOM values are approximately equal. The latter can be ascribed to the almost complete surface coverage assumed in the FDTD calculations.

3.3 Experiments

In an effort to confirm these theoretical findings and elucidate the effects of the substrate on the final sensitivity of the LSPR systems, we carried out a systematic experimental study on both SPP and LSPR sensors. To compare the experimental bulk and surface sensitivities of SPP and LSPR sensors we employed an SPP sensing setup in Kretschmann configuration, which allowed us to spectrally tune the SPP resonance by varying the light incidence angle. Within an angle range between 64° and 78° , we were able to tune the SPP resonance between 600 and 900 nm (For further details, we refer to Section 2.2.1). For the LSPR sensing platform, tunability was achieved by using gold nanorods with ARs ranging from 2 up to 4.5, enabling a spectral resonance tuning from 600 to 800 nm. These nanoparticles, fabricated by wet chemistry, as discussed in Section 2.1.1, were immobilized on glass substrates via electrostatic interactions, using polyelectrolytes, and the scattering spectra from single nanoparticles were acquired using DF spectroscopy (For further details, we refer to Section 2.2.2).

3.3.1 Experimental Bulk Sensitivity Comparison

Bulk sensitivity measurements were carried out by gradually varying the RI of the external dielectric medium (For further details, we refer to Section 2.3). Figure 3.7 shows the results of these experiments for SPP (Subfigures A,C,E) and LSPR (Subfigures B,D,F). For both sensing platforms, η_B was found to linearly increase as λ_{SPR} was red-shifted. Furthermore, the obtained bulk sensitivity of the SPP sensor is an order of magnitude larger than that of its LSPR counterpart. Regarding peak widths, similar trends in the FWHM of the SPP and LSPR sensors were obtained compared to the theoretical calculations, except for the long wavelength region of the SPP sensor. Such difference stems from the surface plasmon excitation in a Kretschmann configuration via the use of a hemi-cylindrical prism. This can be readily explained by looking at a plot of the SPP resonance wavelength as a function of the incidence angle of the light, depicted in Figure 3.8. Here, it can be observed that for a given cone of incident angles (blue vertical bars in Figure 3.8), the range of accessible resonance wavelengths (red horizontal bars in Figure 3.8) increases for lower angles of incidence, that is, for larger values of λ_{SPR} . The latter explains why the experimental resonance peaks obtained for the SPP sensor are broader than expected at higher resonance wavelengths, and hence, demonstrate the apparent saturation of the FOM in this spectral region (see Figure 3.7E).

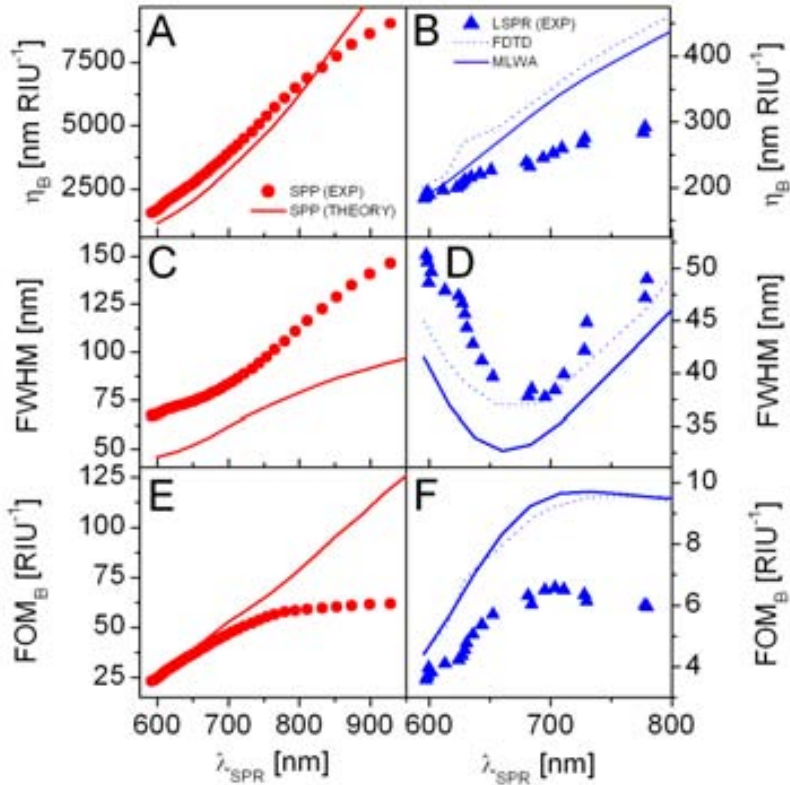


Figure 3.7: Experimental results of the bulk sensitivity measurements carried out on the SPP (Red Dots: **A,C,E**) and LSPR (Blue Triangles: **B,D,F**) sensors. The solid and dashed lines represent the corresponding theoretical values, according to Figure 3.2. The bulk sensitivity η_B , FWHM and FOM were plotted as a function of the spectral position of the resonance peak λ_{SPR} .

However, an overall quantitative FOM-agreement is obtained when comparing the theoretical and experimental results of the SPP sensors. On the other hand, a substantial experimental reduction of η_B and bulk FOM can be appreciated for the gold nanorods, when these results are compared to the theoretical calculations of these nanostructures surrounded by a uniform dielectric medium (Figure 3.2). However, when this experimental outcome is compared with the FDTD calculations of gold nanorods supported by a glass substrate (Figure 3.6), extraordinary agreement between theoretical and experimental values is obtained. The 40% reduction of

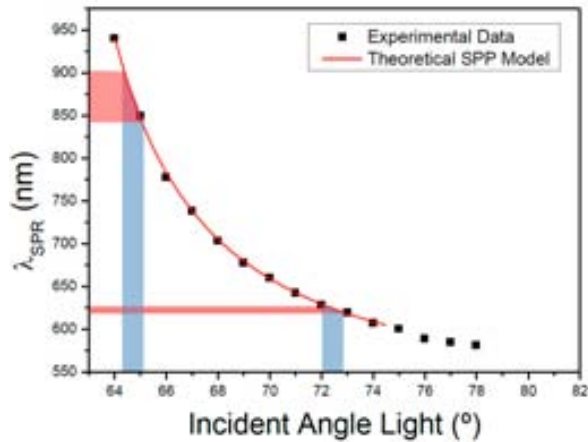


Figure 3.8: Theoretical and experimental SPP resonance wavelengths as a function of the incidence angle of the broadband excitation light.

the bulk sensitivity with respect to the nanoparticles in a homogeneous medium confirms that the nanorods *experience* a smaller effective RI change as compared to the induced external RI change, as a consequence of the high RI of the substrate and the concentration of a substantial part of the EM near field of the LSPR within the glass region.

Interestingly, as indicated from the theoretical analysis, the gathered experimental results evidence that, for bulk RI measurements, the FOM of gold nanorod based sensors exhibits a maximum at approximately $\lambda_{\text{SPR}} = 700$ nm. However, from the much longer spectral shifts obtained for the SPP sensor, one can establish that these sensors clearly outperform the LSPR sensors in bulk RI detection.

3.3.2 Experimental Surface Sensitivity Comparison

The surface sensitivity of both sensing platforms was investigated through the in-flow deposition of oppositely charged PDDA and PSS polyelectrolyte monolayers (RI ≈ 1.50), [166] exploiting the ability of such polyelectrolytes to create conformal multilayers on planar or nanostructured solid substrates (Details on the employed methodology can be found in Section 2.4.1). The results of these measurements are illustrated in Figure 3.9, where η_S and the corresponding surface FOM, averaged over four monolayers, are displayed for both sensor configurations. As an example of these measurements, the inset of Figure 3.9B shows the induced peak shifts as a consequence of the successive deposition of two polymer bilayers for a nanorod with

longitudinal surface plasmon peaking at 711 nm in water.

As becomes clear from the Figure 3.9, SPP and LSPR sensors exhibit a monotonic growth of η_S over the analyzed wavelength range and their FOMs exhibit the expected optimized sensing region for resonances located around 700 nm, confirming what was already perceived in the theoretical simulations: this maximum in the FOM defines an optimized surface sensing region for plasmonic sensing, where the ratio between the induced spectral shifts and the losses due to internal damping mechanisms is optimized. This allows for the a priori optimal determination of the rod geometry or the incidence angle, in order to fully exploit the surface sensing performance of these systems, as also has been considered by *Nusz et al.* for nanoparticles. [167]

The spectral peak shifts of the SPP sensor range from approximately 2 to 8 nm per assembled polyelectrolyte monolayer. Assuming that the refractive index of the polyelectrolytes is 1.50, a thickness around 1 nm per monolayer of polyelectrolyte can be estimated from the measurements, which permits a direct comparison with the theoretical values of the surface sensitivities and FOMs. These measurements show a drastically lower surface sensitivity for the nanoparticles, since their spectral shifts vary between 1.5 and 3 nm per polymer monolayer. This means a 60% drop of surface sensitivity and FOMs with respect to the theoretical calculations. However, we should remember that in the calculations a surface coverage of the nanorods larger than 95% was assumed (section 3.2), whereas the experimentally achieved surface coverage can be substantially smaller, around 50% or even lower. Such considerable surface coverage reduction can be due to the electrostatic repulsion generated by the molecules attached to the surface, which hinder access to the region between nanorod and the glass substrate.

This effect is very likely to be present in biosensing applications, especially for larger biomolecules, such as proteins, unless the substrate is totally inert to unspecific adsorption. Despite of the large reduction of the surface sensitivity in the LSPR sensing scheme, the overall narrower peaks compared to the SPP sensor are ultimately responsible for the resulting higher surface FOM values for the LSPR sensors. Hence, we can conclude that, for surface sensitivity measurements, nanorod based sensors have offered approximately 15% better performance than their SPP counterpart when their FOM was maximized. However, even larger FOM values could be achieved by improving the access of target molecules to the active sensing surface of the nanoparticles, towards the 3-fold enhancement predicted in the theoretical calculations. This can be envisaged through positioning gold nanoparticles on dielectric nanopillars, [168] or using low refractive index and inert substrates,

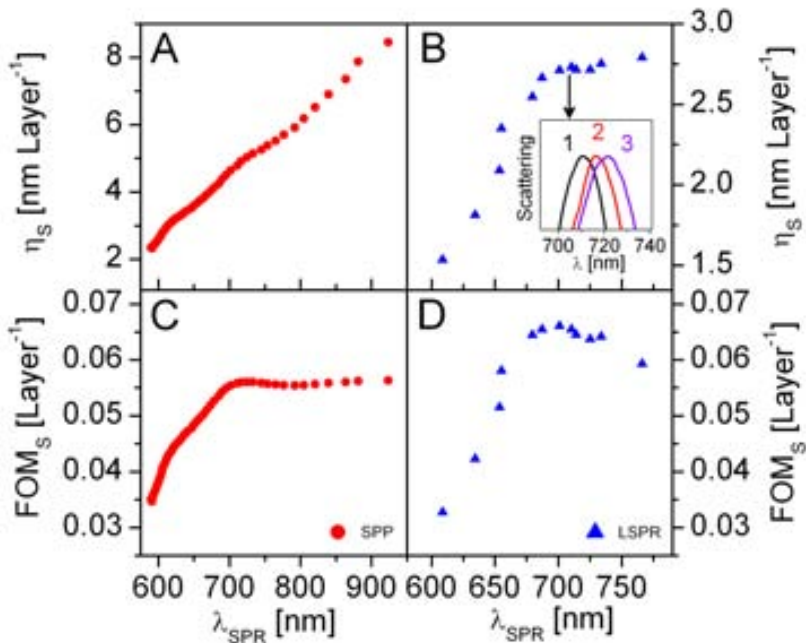


Figure 3.9: Experimental results that show the surface sensitivity η_S and the accompanying FOM as a function of λ_{SPR} for both SPP (A,C) and LSPR (B,D) sensing schemes. The inset in (B) shows the spectral peak shifts as a consequence of the deposition of PDDA/PSS bilayers for a single gold nanorod.

such as fluoropolymers. [169] Another noteworthy alternative to increase the sensor performance involves the use of silver as the plasmonic material, since its lower absorption compared to gold guarantees higher FOM values.

Judging from the surface FOM of both sensor types we can conclude that a substantial improvement of the sensor performance can be achieved by simply separating the resonance wavelength from the gold interband transitions. However, as a consequence of the optimized sensing region, no additional benefit is obtained by red-shifting the resonance indefinitely towards the infrared, which in addition involves complicating the detection systems, especially for single particle sensing. In this respect, colloidal nanorods probably offer the best sensing features in terms of sensitivity and resolution due to their particularly narrow peaks. For the same reasons, nanospheres are poor candidates for LSPR sensing, since the red-shift required to achieve higher sensitivity is accompanied by strong dephasing damping. When compared to the widely employed SPP biosensor, these results support the

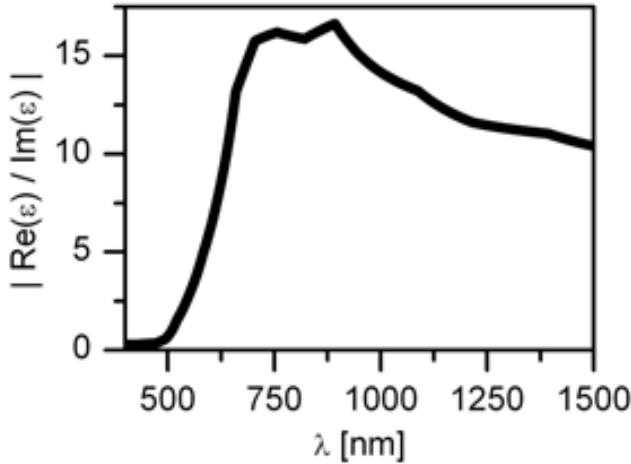


Figure 3.10: Absolute values of the ratio between real and imaginary parts of the dielectric constant of gold, displayed as a function of the wavelength λ of the light.

viable use of this LSPR based sensing scheme in biosensing applications. However, for nanoplasmonic sensors, biosensing detection should be kept within 10-15 nm from the surface. Beyond that distance, the sensitivity is strongly damped, thus limiting the biosensing application to small molecules and advising against, for example, sandwich assays.

3.4 Analytical Derivation Optimized Sensing Region

In an attempt to determine the origin of these optimized surface sensing regions, we analyzed the optical properties of plasmonic materials. In an ideal metal, the spectral plasmonic behavior is restricted to a spectral range between two boundaries: the high energy limit, given by the plasma frequency ω_p , and the low energy limit in which the metal starts acting as a perfect conductor. Above ω_p , the real part of the dielectric constant of the metal becomes positive, thus preventing the excitation of SPRs. On the other hand, for low energies, the penetration of the EM fields in the metal is very weak and the plasmonic behavior is lost. Accordingly, between these boundaries, one can expect a spectral range in which surface plasmons exhibit an optimized performance.

From the analysis of the resonance conditions of both sensor types, it can be

concluded that the real part of the dielectric constant ϵ_{Re} of the metal determines the spectral position of the resonance and according to *Miller et al.*, [77] the bulk sensitivity also depends linearly on ϵ_{Re} , while the imaginary part of the dielectric constant ϵ_{Im} is responsible for the damping. Since the FOM is a measure for the trade-off between the spectral shifts (spectral position of the resonance) and the peak widths (damping), we propose that the maximum of the ratio defined by $\epsilon_{Re}/\epsilon_{Im}$ should coincide with the optimal sensing areas as extracted from the FOMs. Figure 3.10 depicts the absolute value of this ratio as a function of λ using the optical properties of gold employed for our calculations. From this figure we can extract a peak-shaped trend with a range of maximum values located between approximately 700 and 900 nm, indicating that it is in this region, where the ratio between the sensitivity and the FWHM is optimized.

A more detailed derivation supporting this statement can be obtained starting off from a Drude model for free electrons, which represents the archetypical model of plasmonic materials. From the ratio between the real and imaginary parts of the dielectric constant, an analytical formula of the maximum value for $\epsilon_{Re}/\epsilon_{Im}$ can be derived. In this model, ϵ_{Re} and ϵ_{Im} are given by equations 3.9 and 3.10, respectively:

$$\begin{aligned}\epsilon_{Re} &= \epsilon - \frac{\frac{2}{p}}{\gamma^2 + \frac{1}{\Gamma^2}} \\ &= \epsilon - \frac{1}{\lambda_p^2 \cdot \left(\frac{1}{\lambda^2} + \frac{1}{\Gamma^2}\right)}\end{aligned}\quad (3.9)$$

$$\begin{aligned}\epsilon_{Im} &= \frac{\frac{2}{p}\gamma}{\left(\frac{1}{\lambda^2} + \frac{1}{\Gamma^2}\right)} \\ &= \frac{\lambda}{\lambda_p^2 \Gamma \cdot \left(\frac{1}{\lambda^2} + \frac{1}{\Gamma^2}\right)}\end{aligned}\quad (3.10)$$

With the help of equations 3.9 and 3.10, $\epsilon_{Re}/\epsilon_{Im}$ can be written as:

$$\frac{\epsilon_{Re}}{\epsilon_{Im}} = -\frac{\Gamma}{\lambda} + \epsilon \cdot \frac{\lambda_p^2}{\Gamma \lambda^3} \cdot \frac{\Gamma^2 + \lambda^2}{\Gamma \lambda^3}\quad (3.11)$$

By taking the partial derivative of equation 3.11 with respect to λ and setting this equal to zero, as shown in equation 3.12,

$$\frac{\left(\frac{\epsilon_{Re}}{\epsilon_{Im}}\right)}{\lambda} = -\epsilon \frac{\lambda_p^2}{\Gamma\lambda^2} + \frac{\Gamma(\lambda^2 - 3\epsilon \lambda_p^2)}{\lambda^4} = 0 \quad (3.12)$$

and solving this equation for λ , an analytical formula is found for the wavelength at which the ratio $\epsilon_{Re}/\epsilon_{Im}$ reaches its maximum value. This wavelength, defined as λ_{max} is then given by:

$$\lambda_{max} = \frac{\sqrt{3\epsilon} \Gamma \lambda_p}{\Gamma^2 - \epsilon \lambda_p^2} \quad (3.13)$$

In equation 3.13 ϵ (dimensionless) is the dielectric constant of the metal at infinite frequency, Γ (nm) is a measure for the damping of the oscillation and λ_p (nm) is the plasma wavelength of the metal. In order to estimate the necessary parameters to calculate λ_{max} , equations 3.9 and 3.10 were fitted to the experimental ϵ_{Re} and ϵ_{Im} of gold (Note that this was done for $\lambda > 550$ nm, since for lower values of λ interband transitions occur, which are not described by the Drude Model). With the obtained parameters, given by $\epsilon = 8.786$, $\Gamma = 16496$ nm and $\lambda_p = 139.9$ nm, we obtained $\lambda_{max} \approx 718.5$ nm. When comparing this λ_{max} value to the sensing FOMs, we can see that it closely corresponds to the position of the maximum derived from the LSPR FOMs and the start of the saturation observed in the SPP surface FOM. Therefore, we conclude that the overall behavior of these FOMs can be attributed to the intrinsic optical properties of the employed plasmonic material.

3.5 Influence of the Particle Shape on the Sensing Performance

Another interesting and rather surprising feature of a metal nanoparticle's η_S can be extracted from equation 1.14 that defines the polarizability of a coated ellipsoidal particle using a quasi-static MLWA approach. For clarity purposes, we rewrite this equation from Section 1.4.2, given by

$$\alpha_i = \nu \cdot \frac{(\epsilon_s - \epsilon_f)(\epsilon_s + (\epsilon_m - \epsilon_s)(L_{i1} - fL_{i2})) + f\epsilon_s(\epsilon_m - \epsilon_s)}{(\epsilon_s + (\epsilon_m - \epsilon_s)(L_{i1} - fL_{i2}))(\epsilon_d + (\epsilon_s - \epsilon_d)L_{i2}) + fL_{i2}\epsilon_s(\epsilon_m - \epsilon_s)} \quad (3.14)$$

in which

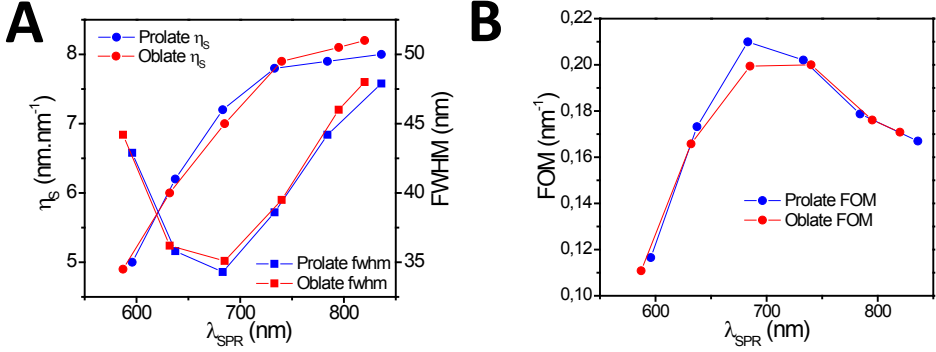


Figure 3.11: (A) Calculated surface sensitivity and FWHM values for prolate and oblate spheroids of identical volumes but with different aspect ratios, together with (B) the corresponding surface FOM.

$$\nu = \frac{a_2 b_2 c_2}{3} \quad (3.15)$$

and

$$f = \frac{a_1 b_1 c_1}{a_2 b_2 c_2} \quad (3.16)$$

being a_2 , b_2 , c_2 and a_1 , b_1 , c_1 the semi-axes of the nanoellipsoids with and without the dielectric shell, respectively, L_{i2} and L_{i1} the depolarization factors in the i direction (see equation 1.10) with and without the dielectric coating, and ϵ_s is the dielectric constant of the modeled dielectric coating. Assuming a dielectric shell that uniformly surrounds the nanoparticle and a coating thickness that is much thinner than the size of the nanoellipsoids' long-axes, the depolarization factors with and without shell are approximately equal, and the main influence exerted by the shell on this expression is embodied by the factor f , which simply represents the ratio of the nanoparticle volume with and without shell. As a direct consequence, if the total volume of the nanoparticle is preserved, nanoparticles with both oblate (disk-like) and prolate (rod-like) shapes can exhibit identical values of η_S . A proof of such behavior is represented in Figure 3.11, where η_S and FWHM-values (Figure 3.11A), together with the corresponding FOM-values (Figure 3.11B) of prolate and oblate nanoellipsoids with different ARs are depicted. These results proclaim that the surface sensitivity

and sensing performance of LSPR sensors is mainly dominated by the spectral position of the LSPR, and the shape of the nanoparticle only plays a secondary role, thereby emphasizing the presented results in this chapter even more.

3.6 Discussion and Conclusion

In this chapter a comparative theoretical and experimental analysis was presented that discusses the sensing performance of wavelength interrogated plasmonic sensors based on SPPs and LSPRs. In this regard, the tunability of both sensing platforms was exploited in order to spectrally vary the resonances for the proper analysis of their bulk and surface sensing characteristics as a function of λ_{SPR} . A FOM, which relates the sensitivity and resolving power of the sensing platforms, was used to extract a general behavior for these plasmonic sensor types. It was demonstrated that the FOMs are equivalent in both wavelength and energy scales. Furthermore, for both sensing schemes the FOM corresponding to η_{S} revealed the existence of an optimized sensing region, which can be assigned to the intrinsic optical properties of the employed plasmonic material, pushing the importance of the particle shape to a secondary plane. For the LSPR sensor, this optimized sensing region corresponds to nanorods with excitation resonances close to $\lambda_{\text{SPR}} \approx 700$ nm. On the other hand, the SPP sensor exhibits a broader optimized surface sensing region comprising resonance wavelengths between 700 and 1000 nm. Although the SPP sensor clearly benefits from η_{B} when compared to its LSPR counterpart, the latter sensor type has proven a 15% better surface sensitivity performance. However, theoretical calculations suggest that a 3-fold improvement of the FOM could be achieved for metal nanoparticles by improving the access of the molecules to the sensing surface.

Chapter 4

Overcoming Substrate Effects for Improved LSPR Sensing

Herein, a study is presented regarding adverse effects that arise when plasmonic nanoparticles are attached to solid supports. Using short-ordered arrays of Au nanodisks as a model system, it is shown that the right choice for the thin metal adhesion layer that is used to assure stable binding of the nanodisks to the substrate, is extremely important in order to achieve a competitive limit of detection. Also, it is shown that the presence of the high refractive index support results in lower bulk and surface sensitivities. In order to minimize this effect, an isotropic etch of the substrate is proposed, resulting in dielectric nanopillars which distance the nanodisks from the underlying substrate. This novel method, not only preserves the mechanical stability of the nanodisks, but also strongly increases their sensing performance. The latter is demonstrated via the label-free detection of DNA hybridization, thereby exemplifying the robustness and the surface-regenerative capabilities of these pillar-supported nanodisk arrays. Furthermore, through successful application of this methodology to more complex nanostructures (nanodisk dimers), this method profiles itself as a simple strategy to improve the limit of detection of a wide variety of nanoplasmonic sensors.

4.1 Introduction

Motivated by the possibilities that metal nanostructures offer to miniaturize and improve the sensitivity of SPP sensors, different conceptual refractometric LSPR biosensing studies have been carried out using nanopores, [170, 171] -pyramids, [126, 172] -dimers, [173] -rings, [174] -tubes, [175, 176] or -disks [177–179] as the sensing platforms. All these different approaches generally aim at a reasonable trade-off between the shape-dependent sensitivity and the fabrication difficulty of the employed nanostructures. Logically, for the creation of high-throughput robust biosensors that are compatible with microfluidics for lab-on-a-chip (LoC) applications, allowing kinetic analysis, and surface regeneration, attachment of the nanostructures to a solid substrate is a prerequisite. This can be either achieved through covalent linking of colloidal nanoparticles to chemically modified substrates or by using metal adhesion layers when lithographic nanopatterning techniques are used. The latter is necessary, since direct adhesion of noble metals on transparent substrates such as silica or organic polymers yields very poor results. However, as extensively discussed in the previous chapter, the presence of a high RI supporting substrate negatively affects the sensing performance of these nanoplasmonic sensors in several ways. Next to the problems regarding unspecific binding of biomolecules to the substrate, the mere presence of this supporting substrate and the employed linking layer can substantially reduce the sensitivity and the S/N of the biosensing measurements. [77, 180]

In this chapter, we point out the problems and limitations that inherently arise from the attachment of the nanoparticles to a solid support and, on the other hand, we provide a very simple strategy to minimize such adverse effects, maintaining the robustness of the sensing transducer intact. For the experimental proof-of-concept, we have opted for the use of short-range ordered arrays of gold nanodisks, a commonly employed nanostructured surface used for biosensing assays, due to its simple and large-scale lithographic fabrication technique. [153] The large nanopatterned area (4 cm²) permits, in addition, the assessment of the homogeneity and robustness of the proposed strategies, which is vital for large scale and high throughput assays. We present results showing that, by separating the nanodisks from the underlying substrate, sensitivities similar to those of nanodisks entirely surrounded by a homogeneous aqueous dielectric medium can be achieved. We corroborate these findings with the label-free detection of DNA strand hybridization, reflecting the high stability and exceptional surface-regenerative capabilities of these sensing substrates. Furthermore, in order to show that this sensitivity enhancing strategy can be used on a

wide variety nanoplasmonic structures, we demonstrate its successful implementation on more complex nanostructures, such as arrays of nanoparticle dimers.

4.2 Effect of Adhesion Layers on Sensing Performance

Chemical modification of the substrate can be a feasible alternative to covalently bind colloidal metal nanoparticles to a substrate. [181] In this case, the chemical link will not noticeably modify the optical properties of the nanostructure, and the main effect will be due to the high RI substrate. In contrast, most lithographic nanopatterning methods make use of thin metal layers, typically made out of Cr and Ti, to provide the mechanical stability required for biosensing applications. Although these layers typically are only a few nanometers thick, their large optical absorption is expected to influence the plasmonic response of the gold nanostructures. To analyze this effect, numerical FDTD calculations were carried out on single gold nanodisks. The nanodisks were modeled as disk-like geometries ($H = 20$ nm and $D = 100$ nm), resembling the nanostructures used throughout the experiments. Furthermore, we assumed a substrate RI of $n = 1.52$ and H_2O ($n = 1.33$) as the external dielectric medium (For further details, we refer to Section 2.5.3.2). A schematic representation of the employed nanodisk geometry is shown in Figure 4.1A.

Figure 4.1B depicts the calculated plasmonic responses of a gold nanodisk contacted to the underlying glass in the absence of any adhering metal (Black line) and via a 1 nm thick Ti (Red line) and Cr (Blue line) layer. Compared to the experimentally non-feasible case in which the gold directly contacts the substrate, these simulations show that a 1 nm thick layer of Ti is expected to result in a 54% reduction of the scattering intensity, while for the use of Cr this effect is even more dramatic (-73%). Furthermore, it can be observed that the FWHM of the scattering peak increases when adhesion layers are introduced. In the absence of an adhesion layer, $FWHM \approx 78$ nm. However, introduction of a Ti or Cr layer results in FWHM-values given by approximately 118 nm and 158 nm, respectively. Both intensity attenuation and peak broadening increase even further for thicker adhesion layers, which can be ascribed to the absorptive properties of the employed adhesion metals and the subsequent damping of the LSPR. Even though the bulk sensitivity of these structures, defined as

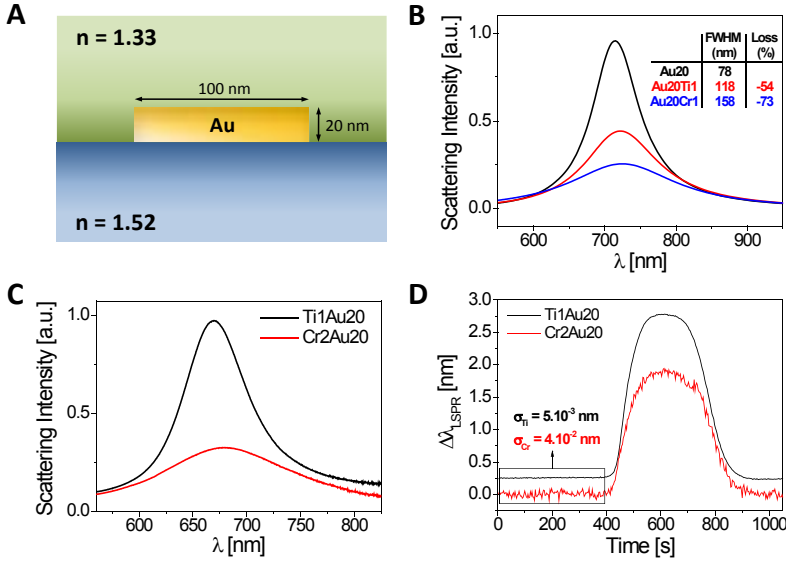


Figure 4.1: Influence of metal adhesion layers on the sensing performance of short-ordered arrays of gold nanodisks. **(A)** Schematic representation of a gold nanodisk on top of a glass substrate ($n = 1.52$), and surrounded by a dielectric medium ($n = 1.33$). **(B)** Calculated LSPR scattering spectra for a single gold nanodisk without a metal adhesion layer (black) and with a 1 nm thick Ti (red) and Cr (blue) sticking layer. **(C)** Experimental LSPR scattering spectra for short-ordered arrays of gold nanodisks, attached to the substrate via a 1 nm thick Ti (black) and a 2 nm Cr (red) adhesion layer and **(D)** the corresponding real-time tracking of the relative LSPR peak displacement ($\Delta\lambda_{LSPR}$) upon an induced bulk refractive index change of $\Delta n = 0.02$.

$$\eta_B^1 = \frac{\Delta\lambda_{LSPR}}{\Delta n_B}, \quad (4.1)$$

in which $\Delta\lambda_{LSPR}$ is the spectral shift of λ_{LSPR} and n_B is the bulk RI, is not significantly affected by the use of adhesion layers, both attenuation of the scattering intensity and peak broadening are expected to manifest themselves in much lower values of S/N, thereby reducing the resolving power of these nanoplasmonic sensors.

To confirm this effect experimentally, short-ordered arrays of gold nanodisks

¹Note that compared to Chapter 3 (equation 3.1), the expression of η_B is slightly altered since no distinction has to be made between SPP and LSPR sensors. From this point onward, only LSPR sensors are taken into account, and hence, the spectral location of the resonance peak is written as λ_{LSPR}

($H \approx 20$ nm and $D \approx 100$ nm) were fabricated by hole mask colloidal lithography (For further details, we refer to Section 2.1.2). In order to emphasize the adverse effects predicted by the simulations even more, 1 nm Ti and thicker 2 nm Cr adhesion layers were employed: samples fabricated without an adhesion layer were not mechanically stable. Figure 4.1C compares the LSPR spectra in H_2O for both latter cases, showing that, concurring with the theory, the plasmonic response is indeed strongly influenced by both the thickness and the composition of the employed metal adhesion layer. When comparing the scattering peaks, a 67% lower intensity and a much broader FWHM peak (FWHM ≈ 153 nm) is obtained for the nanodisks with the 2 nm Cr layer. In order to analyze how this affects the sensing performance of the nanodisks, η_B was tested by low angle reflectance measurements. For that purpose, a 12.7% glycerol solution ($n = 1.3522$) was employed to induce a RI change (Δn) of 0.02 refractive index units (RIUs) with respect to H_2O (For further details, we refer to Sections 2.2.3.1 and 2.3).

Figure 4.1D shows the real-time tracking of $\Delta\lambda_{LSPR}$ for both nanodisk samples, showing a clear red-shift of the LSPR while the higher RI glycerol solution flows through the flow cell. The normalized η_B -values extracted from these curves are given by $\eta_B \approx 95$ nm \cdot RIU $^{-1}$ and $\eta_B \approx 125$ nm \cdot RIU $^{-1}$ for the Cr and the Ti samples, respectively. Although the sensitivities, i.e. the absolute spectral shifts, are expected to be the same for both nanodisk substrates, the measurements indicate a different behavior. This observed discrepancy can be attributed to thickness uncertainties regarding the evaporated metal layer or different surface roughness. On top of the sensitivity, the S/N is a more critical parameter to evaluate the final LOD of the LSPR sensing platform. As shown in Figure 4.1D, the standard deviations θ of the signals for Ti and Cr linked nanodisks are given by $\theta_{Ti} = 5 \cdot 10^{-3}$ nm and $\theta_{Cr} = 4 \cdot 10^{-2}$ nm, respectively. These results clearly demonstrate that the lower intensity and larger FWHM obtained for the Cr sample deteriorate the resulting LOD an order of magnitude when compared to the case in which Ti is used. Therefore, we can conclude that although absorption of light by metal adhesion layers inevitably affects the sensing performance, the use of the less absorbing material is strongly advised in order to obtain a better refractometric sensing performance of the nanoplasmonic sensor. Therefore, we used nanodisks with a 1 nm Ti adhesion layer throughout all other experiments, whose results are discussed in this chapter.

4.3 Effect of Substrate RI on Sensing Performance

As a next step, we studied the role that the underlying substrate RI has on the sensing performance of the nanoplasmonic nanodisks. First, present theoretical results that quantitatively assess the negative influence that this parameter exerts on the sensing performance of single gold nanodisks. Then, we theoretically show how these problems can be overcome, by creating pillar-supported suspended nanodisks. Finally, we corroborate these theoretical findings with experimental results.

4.3.1 Influence of Substrate RI on Nanodisk Sensing Performance

A vast majority of transparent substrates on which plasmonic nanostructures can be fabricated have a larger RI than that of typical aqueous solutions used in biosensing assays. As a consequence, the symmetry of the EM near-field around the nanodisk is broken, shifting a large portion of such field towards the substrate, where it is almost entirely insensitive to RI changes of the external medium. Figure 4.2A, depicting the near-field EM intensity profile of a gold nanodisk, surrounded by H₂O and located on a substrate (glass, $n = 1.52$), clearly illustrates this effect. To analyze how this affects the sensing performance of these nanostructures, we calculated the sensitivity of the nanodisks for supporting substrates with different values of RI (For further details, we refer to Section 2.5.3.2).

Typically, the sensitivity of nanoplasmonic sensors is quantified by the value of η_B . When biosensing applications are considered, analyte binding takes place at the vicinity of the metal surface and, therefore, only a portion of the excited EM field is employed in the detection process. Consequently, η_B and the so-called surface sensitivity η_S , defined as the spectral resonance shift $\Delta\lambda_{LSPR}$ divided by the thickness (d) of an adsorbed biolayer (see Equation 3.2) can show very different behavior as already been described and demonstrated in Chapter 3.

Therefore, distinction between both parameters is recommendable, making η_S a more interesting parameter to quantify and compare the biosensing performance of refractometric sensors. In order to check these differences we calculated both η_B and η_S , assuming in the latter a homogeneous dielectric shell ($n = 1.50$) covering the exposed gold surface of the nanodisk. As shown in Figure 4.2B, for a glass-supported gold nanodisk, both η_B and η_S suffer a drastic reductions ($\eta_B = 225 \text{ nm}\cdot\text{RIU}^{-1}$, $\eta_S = 2.75 \text{ nm}\cdot\text{nm}^{-1}$) compared to the values corresponding to a gold nanodisk in the absence of a substrate, that is, homogeneously surrounded by H₂O. In this latter case,

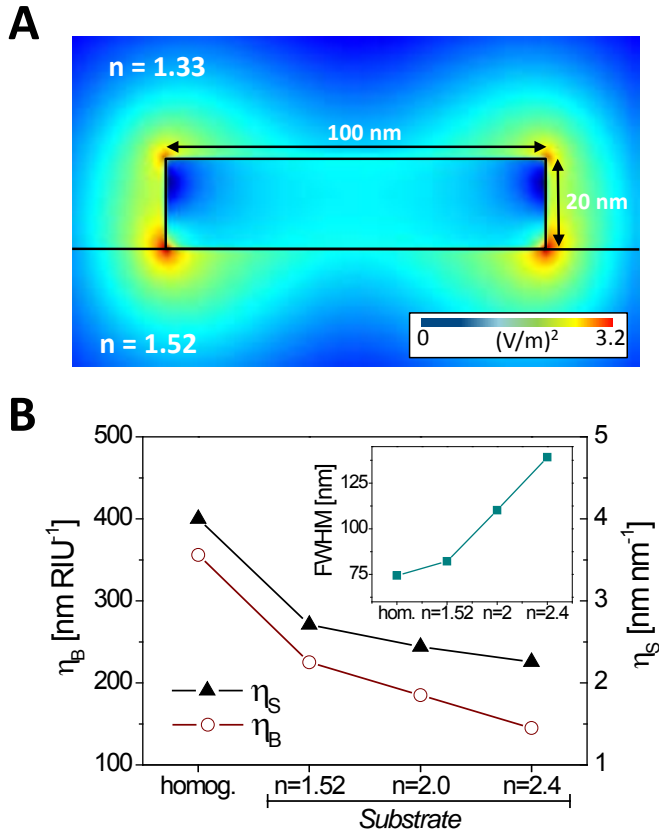


Figure 4.2: (A) Calculated near-field electric field profile of a single gold nanodisk located on a supporting substrate ($n = 1.52$), and surrounded by a homogeneous dielectric medium ($n = 1.33$). (B) Calculated bulk and surface sensitivities for a single gold nanodisk surrounded by a homogeneous dielectric surrounding ($n = 1.33$) and for nanodisks supported by substrates with different refractive indices. The inset figure shows the corresponding FWHM values of the calculated LSPR spectra.

η_B and η_S are given by $\eta_B = 356 \text{ nm} \cdot \text{RIU}^{-1}$ and $\eta_S = 4.05 \text{ nm} \cdot \text{nm}^{-1}$, respectively. For substrates with an even higher RI, such as TiO_2 ($n = 2.4$), the sensitivity decrease is even more pronounced, reaching values close to a decrease of 45% for η_S and up to a 60% decrease for η_B ($\eta_S = 145 \text{ nm} \cdot \text{RIU}^{-1}$, $\eta_S = 2.25 \text{ nm} \cdot \text{nm}^{-1}$). Moreover, these simulations also show that a larger RI of the substrate is also accompanied by a substantial increase of the FWHM of the resonance peak, (Inset of Figure 4.2B), thereby negatively affecting the ability to discriminate small spectral shifts.

4.3.2 Improving the Sensing Sensitivity Suspended Nanodisks

The previous results clearly demonstrate that, in order to achieve higher sensitivities and an improved resolving power of the sensor, the influence of the high RI substrate needs to be minimized. In order to achieve this, different strategies have been reported, such as the use of low RI substrates, [169] or bottom-up fabricated SiO₂ nanoposts. [168] Herein, we propose the isotropic wet chemical etch of the nanopatterned substrate to create suspended nanoparticles supported by dielectric pillars. The isotropic etching process not only frees up additional gold surface on the lower side of the nanodisk, it also redistributes the EM field in a more symmetrical way, thereby exposing the EM hot-spots to the dielectric environment surrounding the nanostructure, as is schematically shown in Figure 4.3A. Both factors are expected to contribute to an enhancement of the sensitivity parameters, defined by η_B and η_S . This presumption is confirmed in Figure 4.3B by the calculations of η_B and η_S as a function of the isotropic etching depth of the underlying substrate. It is worth noticing that η_B steadily increases as the etching depth becomes larger, thereby slowly tending towards the value of a non-supported, by H₂O-surrounded nanodisk, when the etching depth is around 28 nm ($\eta_B = 356 \text{ nm} \cdot \text{RIU}^{-1}$, Figure 4.2B). In contrast, η_S shows a much steeper grow for increasing etch distances. In this case, for an etching depth of 20 nm, the value of η_S is already similar to that of the same nanodisk completely embedded in H₂O ($\eta_S = 4.05 \text{ nm} \cdot \text{nm}^{-1}$, Figure 4.2B). The latter can be ascribed to the *liberation* of the high EM intensity zone initially located at the interface between the lower side of the nanodisk and the substrate, thereby making it available for surface sensing purposes. Due to the strong confinement and the exponential decay of the excited EM field, the strong effect that the removal of high RI material has on η_S becomes smaller for larger etching distances, explaining the decreased slope in Figure 4.3B for increasing pillar heights. Therefore, from an optical perspective, the nanodisk will behave as if it were *suspended* in the surrounding dielectric environment, thereby not experimenting any kind of hinder caused by a supporting substrate. In this situation, the the maximum achievable enhancement factors for η_B and η_S are given by 70% and 60%, respectively. Interestingly, keeping in mind that the the sensitivity of plasmonic nanostructures increases (decreases) as λ_{LSPR} is red-shifted (blue-shifted), [77] the obtained results show that although λ_{LSPR} is blue-shifted as the etching depth becomes larger (an inherent process caused by the removal of high RI material, see Inset of Figure 4.3B) both η_B and η_S still experience an large sensitivity-enhancing boost. Such behavior highlights the critical importance

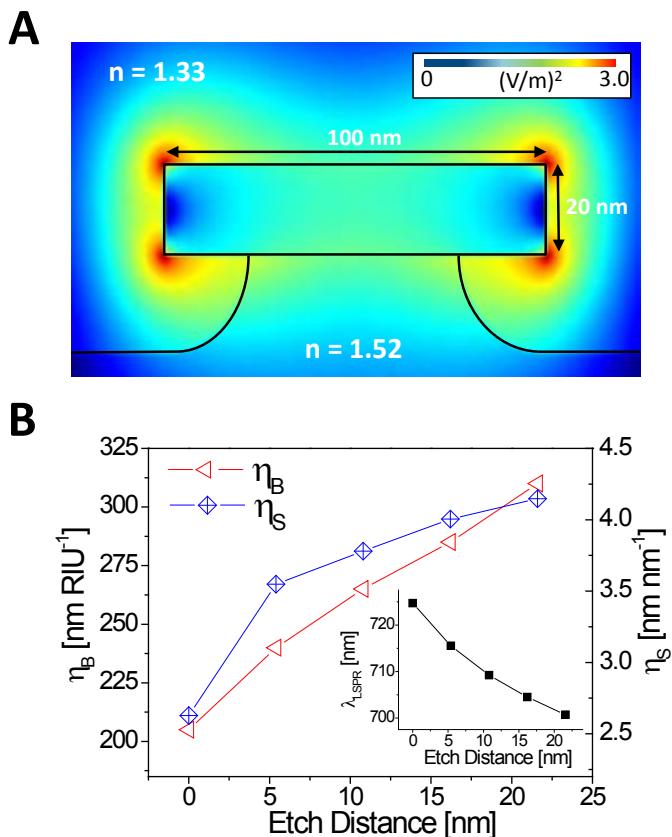


Figure 4.3: (A) Near-field electromagnetic field profile of a single gold nanodisk supported by a 22 nm isotropic pillar ($n = 1.52$), and surrounded by a dielectric medium ($n = 1.33$). (B) Calculated bulk and surface sensitivities for a single gold nanodisk supported by a dielectric pillar for different isotropic etch distances. The inset shows the corresponding LSPR spectral peak positions.

of the redistribution of the EM generated by the LSPR and the improvement of its accessibility to the local changes of RI.

4.3.3 Experimental Bulk Sensitivity Suspended Au Nanodisks

To corroborate these theoretical results, η_B was experimentally tested through low angle reflectance measurements (For further details, we refer to Section 2.2.3). As discussed in Section 2.1.2.3, HF was chosen as the desired chemical to accurately

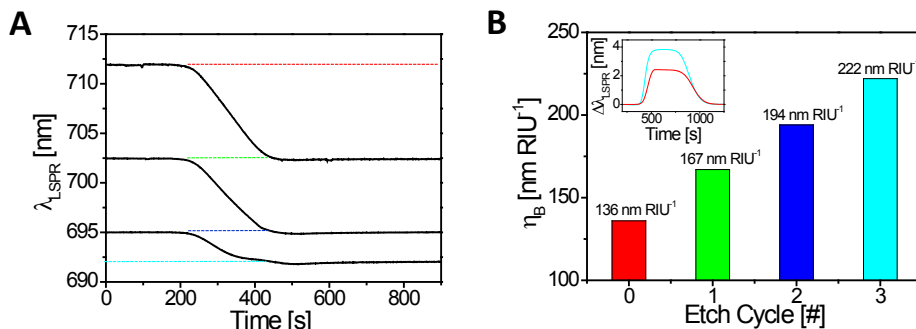


Figure 4.4: (A) Real-time tracking of the LSPR peak position (λ_{LSPR}) for subsequent in-flow hydrofluoric acid etch cycles. (B) Experimental bulk sensitivities obtained after each of the etch cycles. The inset figure displays the real-time monitoring of the relative LSPR peak displacement ($\Delta\lambda_{LSPR}$) before etching (red) and after the third etching cycle (blue).

control the isotropic etching process of the underlying SiO_2 for the creation of suspended Au nanodisks. For the assessment of the bulk sensitivity, the diluted HF solution was injected in-flow. Figure 4.4A shows the real-time tracking of λ_{LSPR} for three subsequent HF in-flow etching cycles (numbered 0 to 3). As expected, every HF etch cycle causes a blue-shift of λ_{LSPR} , in accordance with the removal of high RI material, thereby diminishing the effective RI experienced by the nanostructures. In agreement with the theoretical predictions, the first etching cycle clearly provokes the largest resonance blue-shift, given by $\Delta\lambda_{LSPR} \approx -9.5$ nm. As stated before, this effect is caused by *lifting* the EM hotspots that were originally located at the interface between the metal and the substrate into the aqueous dielectric surroundings of the nanodisks. Further substrate etching shows smaller absolute blue-shifts, since the effect of the underlying substrate becomes less dominant. A total of three consecutive etching cycles could be carried out, yielding a total absolute LSPR blue-shift given by $\Delta\lambda_{LSPR} \approx 20$ nm), before extreme LSPR peak-broadening was observed, accompanied with significant losses in scattering intensity. From this, two conclusions can be drawn. First, from the constant peak widths during the first three etching cycles we can assume that the etching of the substrate is indeed isotropic and very homogeneous, affecting all disks in the same manner. Second, after any further substrate etching, the dielectric pillars become unstable, thereby tilting the nanodisks, or even cutting them loose from the substrate.

Before and after each of the HF substrate etching steps, duplicated η_B measurements were carried out by varying the RI of the dielectric surroundings of the

nanodisks by $\Delta n = 0.02$ RIU (For further details, we refer to Section 2.2.3.1 and 2.3). The corresponding results are shown in Figure 4.4B. Here, we can observe that η_B monotonically increases after each etching cycle, from $\eta_B \approx 136 \text{ nm} \cdot \text{RIU}^{-1}$ for non-suspended to $\eta_B \approx 222 \text{ nm} \cdot \text{RIU}^{-1}$ for suspended nanodisks (3 etching cycles), yielding a total η_B -enhancement of approximately 67%.

The inset of Figure 4.4B shows the real-time tracking of $\Delta\lambda_{\text{LSPR}}$ for both of these measurements, exemplifying the enhanced η_B -values obtained for the HF etched substrates. When comparing these results to the theoretically predicted values, we can conclude that although the same approximate linear trend is observed as a function of the etching distance, the experimentally obtained η_B -values are substantially smaller. This difference can be attributed to geometrical differences between the ideal sharp-edged disks used in the simulations and the fabricated nanodisks. Surface tension of the latter causes them to re-shape, forming more oblate-shaped geometries. The accompanying rounding of the disk edges attenuates the local EM hotspots that are found at sharp particle features, thereby diminishing the sensitivity of the nanostructures.

4.3.4 DNA Hybridization Measurements

In order to test whether the sensitivity enhancement observed in the bulk sensitivity measurements also holds for η_S , real biosensing measurements were carried out using the nanodisk samples as model systems for the detection of DNA hybridization (For further details, we refer to Section 2.4.2). For that purpose, a short single-stranded DNA sequence (32-mer), part of the *iap* gene of bacteria *Listeria Innocua* encoding a major part of the extracellular protein (*p60*) was used to monitor DNA hybridization. Thiolated, 24-mer receptor probes were previously immobilized on the surface of the nanostructures using an ex-situ immobilization protocol. Using a DNA target at a concentration of 200 nM, hybridization measurements were carried out in-flow, monitoring $\Delta\lambda_{\text{LSPR}}$ as a function of time. To analyze the influence of the etching process on the surface sensing performance of the nanodisks, these measurements were carried out on both non-suspended and suspended nanodisk samples. Since an ex-situ DNA immobilization protocol was used to functionalize the nanodisks, it was necessary to suspend the nanodisks ex-situ. The latter was achieved via a 10-minute HF immersion of a nanodisk substrate, resulting in an average isotropic etch distance of approximately 10-11 nm (For further details, we refer to Section 2.1.2.3).

Figure 4.5A depicts two typical hybridization signals (green and red curves) that

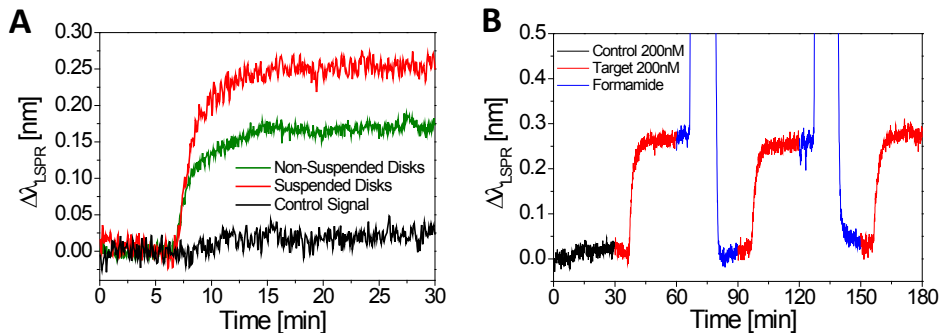


Figure 4.5: (A) Real-time tracking of the relative LSPR peak displacement ($\Delta\lambda_{LSPR}$) caused by DNA hybridization for non-suspended (green) and suspended (red) nanodisks. The black line represents a control signal of a non-specific DNA sequence. (B) Real-time monitoring of the relative LSPR peak displacement ($\Delta\lambda_{LSPR}$) for several consecutive DNA hybridization and surface regeneration cycles carried out on suspended nanodisks.

were obtained in these experiments, belonging to non-suspended and suspended nanodisks, respectively. From these graphs we can conclude that a considerable larger hybridization signal ($\Delta\lambda_{LSPR} \approx 0.25$ nm) is obtained for pillar-supported nanodisks, compared to those lying on a plain glass substrate ($\Delta\lambda_{LSPR} \approx 0.16$ nm). Injection of a non-complementary control DNA sequence (black line) resulted in a negligible small signal of ($\Delta\lambda_{LSPR} \approx 0.02$ nm), thereby ruling out non-specific adsorption of complementary DNA to the utmost extent. These hybridization measurements were carried out repeatedly on two different surfaces of both suspended and non-suspended nanodisks, showing good levels of reproducibility. Whereas for non-suspended nanodisks, the detection of specific ssDNA strands resulted in an average signal given by $\Delta\lambda_{LSPR} \approx 0.176 \pm 0.006$ nm, for the suspended nanostructures a signal of $\Delta\lambda_{LSPR} \approx 0.248 \pm 0.009$ nm was obtained, yielding an average surface sensitivity enhancement of approximately 41%. Such enhancement could probably be increased by improving the accessibility of the complementary DNA strands with the use of vertical and lateral spacers as has been shown by our group for conventional SPP sensors. [182]

An important aspect for many label-free biosensing applications is the possibility of bioreceptor regeneration. For this, the binding of the analyte with its corresponding specific immobilized receptor must be broken, keeping the immobilized layer of bioreceptors active for further measurements. In our particular application the regenerability of the functionalized nanostructured surfaces was tested by dehybridizing the

double stranded DNA with a formamide solution. The results of several consecutive hybridization and regeneration cycles, measured on an array of suspended nanodisks are shown in Figure 4.5B. As can be seen in the graph, injection of formamide causes the λ_{LSPR} to blue-shift to its initial spectral position, that is, before DNA hybridization. As displayed by the graph, these hybridization and regeneration cycles could be carried out repeatedly. Subsequent injection of the target DNA always resulted in similar signal levels, throughout the lifespan of the receptor (more than 10 cycles), thereby emphasizing the stability and robustness of these suspended nanostructures as sensing platforms for real biosensing applications.

4.3.5 Bulk Sensitivity of Suspended Au Nanodisk Dimers

Once it has been established that suspended gold nanodisks exhibit a significantly improved sensing performance, as a next step, we tested this novel sensitivity enhancing method on a more complex geometry in order to show that this technique can be easily extended to other nanoplasmonic structures. For this, short-ordered arrays of gold nanodisk ($D = 100$ nm, $H = 20$ nm) dimers were fabricated with inter-disk distances of approximately 30 nm (For further details, we refer to Section 2.1.2.2). In Figure 4.6A scattering spectra (continuous curves) of these closely distanced nanostructures are shown with the incident light polarization either parallel or perpendicular to the dimer-axis. Note that the LSPR spectra corresponding to the longitudinal polarization, i.e. along the dimer axis, is red-shifted with respect to the transversal polarization, i.e. perpendicular to the dimer axis. As expected, suspension of these nanostructures, through the creation of isotropic dielectric pillars, results in blue-shifted LSPR spectra for both polarization directions (dashed curves). These results indicate that the plasmonic properties of these suspended dimer substrates are preserved. In order to compare the sensing characteristics of these nanodimers in both polarizations and to test whether this parameter is affected upon suspension of these structures, η_{B} measurements were carried out. Figure 4.6B depicts the obtained η_{B} -values for both longitudinal and transversal polarizations, before and after suspension. When comparing both polarizations, it becomes clear that larger η_{B} -values are obtained for the direction parallel to the dimer axis. This effect can be ascribed to the high EM intensity region created in the gap between the nanodisks. The inset of Figure 4.6B shows for both polarizations the real-time tracking of $\Delta\lambda_{\text{LSPR}}$ for an induced bulk RI change of $\Delta n = 0.02$ RIU for nanodisk dimers supported by a glass substrate. The extracted η_{B} -values for the transversal and

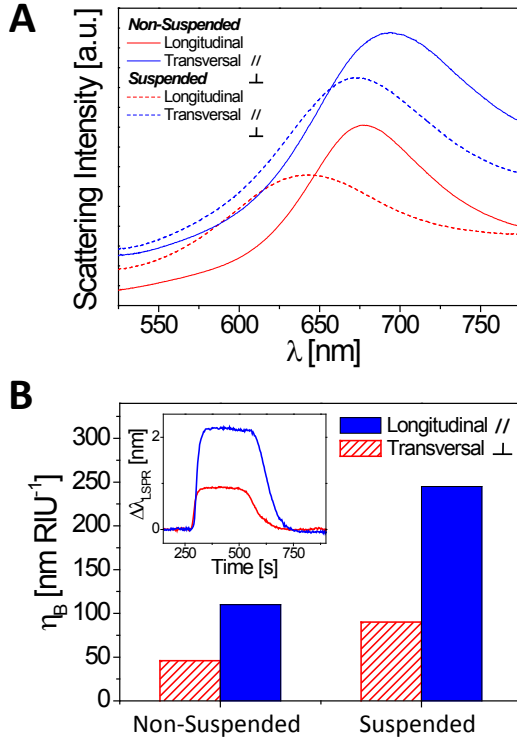


Figure 4.6: (A) Experimental scattering spectra of non-suspended and suspended gold nanodisk dimer substrates, with the polarization of the incident light both parallel and perpendicular to the dimer axis. Subfigure (B) depicts the corresponding experimental bulk sensitivities. The inset figure shows the real-time tracking of the relative LSPR peak displacement ($\Delta\lambda_{LSPR}$) for non-suspended dimers for both longitudinal (blue) and transversal (red) polarization directions upon an induced bulk refractive index change of $\Delta n = 0.02$.

longitudinal polarizations are given by $\eta_B = 46 \text{ nm}\cdot\text{RIU}^{-1}$ and $\eta_B = 110 \text{ nm}\cdot\text{RIU}^{-1}$, respectively, while suspension of these nanostructures approximately doubles these values to $\eta_B = 90 \text{ nm}\cdot\text{RIU}^{-1}$ and $\eta_B = 245 \text{ nm}\cdot\text{RIU}^{-1}$. From this, it can be concluded that, as expected, suspension of the dimers indeed improves their sensitivity. But more importantly, these results indicate that this sensitivity enhancing method can be used with more complex geometries with very short separation distances. As a consequence, this novel method presents itself as an easily applicable, general way to improve the sensitivity of a wide variety of refractometric LSPR sensing platforms.

4.4 Discussion and Conclusion

In this chapter we have analyzed the main adverse effects for biosensing applications associated to the attachment of plasmonic nanostructures to a solid supporting substrate. First, we have shown how the thin metal adhesion layer typically used to attach plasmonic nanostructures to the supporting substrate negatively influences the refractometric sensing performance, inducing a drastic reduction of S/N of the refractometric measurement. To diminish the consequences of this problem it is strongly advised to keep this layer as thin as possible and use a low absorptive metal. We have shown that 1 nm of Ti provides enough mechanical stability to allow in-flow biosensing measurements and surface regeneration. Moreover, the refractometric sensitivity is also severely affected by the presence of the high RI supporting substrate. Herein, an isotropic wet chemical etching process to distance the plasmonic nanostructures from the underlying substrate is introduced as a novel method to diminish the negative impact that the substrate has on the sensing sensitivity. Due to its facile implementation, this method can be easily extended to a wide variety of nanostructure geometries and substrates, exemplified in this manuscript with the use of short-ordered arrays of gold nanodisk dimers. To emphasize the potential use of these suspended nanostructures for real applications, the etched nanodisk platforms were used as model systems for DNA hybridization measurements. Duplex DNA formation was detected in both suspended and non-suspended gold nanodisk arrays. In these experiments, a sensitivity enhancement of 41% was established for suspended nanodisks, providing clear proof of the sensitivity improving properties of these dielectric nanopillars. The excellent surface-regenerative properties of the suspended nanostructures and the reproducibility of the measurements emphasize their robustness and stability, making them very suitable candidates for more exhaustive or even multiplexed biosensing assays.

Chapter 5

Far-Field Guided Modes for Improved LSPR Sensing

Encouraged by the capacity of surface plasmons to confine and propagate EM fields, waveguiding concepts have been developed, including combinations of continuous metal films or ordered arrays of metal nanoparticles. So far, waveguiding in the latter systems has been based on near-field or diffractive coupling. Herein, we show that monolayers of sparse and disordered gold nanodisks support a novel TE guided mode that contrary to previous work, relies on the strong enhancement of the polarizability upon excitation of the nanoparticle LSPR, creating an effective refractive index sufficiently high to support light guidance over a large range of frequencies. Excitation of this guided mode offers interesting nanophotonic features and applications such as a tunable total absorption spectral band, attractive for light harvesting applications, or the generation of a large amplification of the sensitivity to refractive index changes, accompanied with striking enhancement of the limit of detection in real biosensing experiments.

5.1 Introduction

The ability of Surface Plasmons (SPs) to confine and transport EM energy has boosted the development of integrated nanophotonic circuitry combining sub-wavelength EM field localization and moderate propagation distances. When using thin metal films or stripes as waveguides, a trade-off between confinement and propagation is necessary. Whereas short-range SPPs offer strong confinement, their propagation distance is strongly suppressed by inherent ohmic losses. [108, 132] Contrary, long-range SPPs exhibit propagation distances longer than one cm in the infra-red (IR) at the cost of poor spatial mode localization. [183–185] In order to tackle this trade-off, other waveguiding schemes have been proposed, such as metal-insulator-metal-, [186] hybrid-, [187, 188] and channel waveguides, [189] offering both low propagation losses and strong mode confinement up to telecommunication frequencies. In order to achieve additional mode confinement and miniaturization, an alternative approach for nanoplasmonic waveguiding is offered by ordered arrays of metal nanoparticles. For interparticle separation distances lower than the size of the nanostructures, near-field optical coupling assures inter-particle energy transfer with EM confinement well below the diffraction-limit. Following this path, linear chains of ordered nanoparticles have indeed proven their potential as nanoplasmonic waveguides. [8] Extension of these linear chains into 2D arrays of metal nanostructures revealed the existence of in-plane plasmon modes based on either EM near-field interactions or diffractive far-field effects, [175, 190–195] and out-of-plane subradiant lattice modes. [196] However, in all these cases the necessity of short inter-particle distances and/or precise particle ordering puts serious demands on the employed fabrication techniques, typically requiring expensive methods that inhibit the patterning of large surface areas.

In this chapter, we discuss a novel type of in-plane guided mode present in extremely thin monolayers of short-ordered arrays of gold nanodisks. Compared to previous works, due to the large inter-particle distances and their random distribution, no EM near-field or diffractive effects lie on the basis of this waveguiding behavior. Instead, these guided modes arise as a consequence of the large enhancement of the effective RI of the monolayer, thus creating an effective medium of plasmonic meta-atoms with large polarizability. Excitation of these guided modes in TIR can drastically increase light-matter interaction leading to interesting effects such as tunable total absorption of the incident photons with an extremely low quantity of plasmonic material, or large amplification of the sensitivity and the LOD in biosensing measurements. The interest of these applications is boosted by the possibility to

fabricate the random plasmonic monolayers with robust, low-cost and wafer-scale self-assembled colloidal lithography techniques, such as those already described in Section 2.1.2.

5.2 TE Guided Modes in Thin Monolayers of Au Oblate Spheroids

The waveguiding properties 2D nanoparticle arrays can be modeled by different theoretical models, among which those based on Generalized Sheet Transition Conditions (GSTC), [197] or dipolar approximations can be highlighted. [198] However, in our particular case the optical properties of a random and sparse distribution of sub-wavelength sized nanoparticles are accurately described by the MG effective medium theory, in which the inhomogeneous medium is treated as a homogeneous medium with an effective RI (For further details, we refer to Section 2.5.4). This approach is justified given the very low density of nanodisks to neglect near-field interactions. We model these disk-shaped nanostructures as infinitely small gold oblate ellipsoidal geometries, with an AR of 5:1 between the long and short axis, respectively, being buried in a homogeneous dielectric ($n = 1.33$), as schematically depicted in Figure 5.1A.

5.2.1 Mode Dispersion and Reflectivity Spectra

The shape anisotropy of the nanoparticles creates an effective optical birefringence and, therefore, distinction has to be made between the in- and out-of-plane effective RI ($n_e = \eta + i\kappa$). Figure 5.1B shows the calculated real (η_{in}) and imaginary part (κ_{in}) of the in-plane n_e of the anisotropic medium for different nanoellipsoid surface densities (F) as a function of λ . The spectra exhibit a typical resonance shape with a large increase of η_{in} and κ_{in} near the LSPR of a single ellipsoid ($\lambda_{LSPR} \approx 660$ nm). Over the entire analyzed wavelength range, higher values of F are accompanied by higher values of η_{in} and κ_{in} . For surface occupation densities as low as 6%, the effective RI in the vicinity of λ_{LSPR} is already substantially larger than that of most materials found in nature. In contrast, the out-of-plane n_e reveals much smaller values of η_{out} and κ_{out} with a blue-shifted peak, consequence of the weak polarizability of the ellipsoids in this direction (Figure 5.1C). Such behavior unambiguously shows the fundamental role that the LSPR plays in the optical properties of the MG effective medium.

The large enhancement of in-plane n_e suggests the ability of these effective media

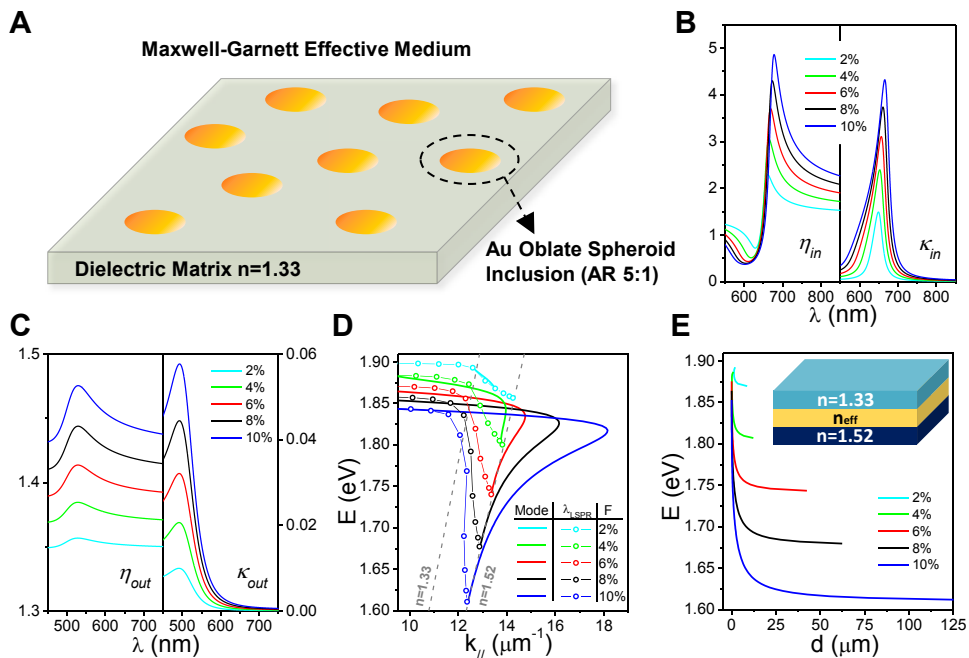


Figure 5.1: Calculated optical properties corresponding to monolayers of sparse and randomly ordered arrays of gold nanoellipsoids for different nanoparticle densities ($F = 2$ - 10%). (A) schematics of the modeled Maxwell-Garnett effective medium, showing gold oblate spheroids in an otherwise homogeneous dielectric layer ($n = 1.33$) (B) real η and imaginary part κ of the of the in-plane and (C) out-of-plane refractive indices as a function of the wavelength λ . (D) TE Guided mode dispersion curves (straight lines) and spectral resonance positions of angle-dependent reflectivity spectra (dash-dotted lines). (E) Calculated theoretical propagation distances of TE guided modes as a function of the energy E . The inset shows waveguide schematics.

to act as nanophotonic waveguides, as long as the RI of the effective layer is larger than that of its cladding layers. This requirement is easily met for $\lambda \geq 650$ nm and $F \geq 2\%$, assuming the effective medium to be confined between SiO_2 ($n = 1.52$) and H_2O ($n = 1.33$). To confirm the capacity of the effective media to support guided waves, wavelength-dependent mode solutions are calculated for different polarizations via a Transfer Matrix formalism valid for arbitrary anisotropic multilayers (For further details, we refer to Section 2.5.4). In order to model a nanoplasmonic waveguide we assume that the thickness of the monolayer is only 20 nm, comprised between two cladding layers (SiO_2 , $n = 1.52$ and H_2O , $n = 1.33$). The chosen layer thickness of 20 nm, together with the imposed AR of 5:1, therefore inherently results in nanoellipsoid diameters of $D = 100$ nm. The low values of η_{out} and κ_{out} rule out

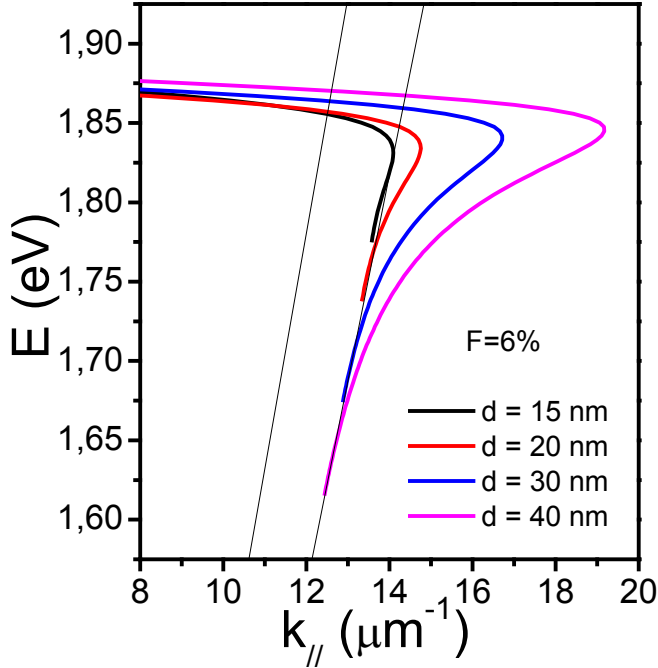


Figure 5.2: Calculated dispersion relation for a fixed nanoellipsoid density of $F = 6\%$ and aspect ratio (5:1), as a function of different effective layer thicknesses, ranging from $d = 15$ nm to $d = 40$ nm.

the existence of TM modes, however, the TE polarization only depends on η_{in} and κ_{in} , which are both greatly amplified near the LSPR. As a consequence, guided mode solutions and their associated dispersion relation can be found for TE polarization when $F \geq 2\%$, as shown by the solid lines in Figure 5.1D.

For low concentrations ($F \approx 2\%$) the guided mode is restricted to a very short energy range. Due to the overall increase of n_e for larger values of F , the dispersion curves nicely illustrate that denser nanoparticle layers are expected to sustain waveguiding behavior over a longer energy range. The dispersion relations exhibit a region of anomalous dispersion ($dE/dk_{\parallel} < 0$ and $dn/d\lambda > 0$) in the high energy range, typically characterized by quasi-bound, leaky modes. This region transitions into a regime of normal dispersion ($dE/dk_{\parallel} > 0$ & $dn/d\lambda < 0$) showing large wave-vector values (k_{\parallel}) near the resonance energy of single nanoellipsoids. In these regions, κ_{in} is greatly amplified (Figure 5.1B), yielding strong damping and

hence very short propagation distance d (Figure 5.1E). However, at lower energies ($E < 1.77$ eV and $\lambda > 700$ nm) guided modes with propagation distances larger than $100 \mu\text{m}$ can be achieved, owed to the drastic reduction of κ_{in} while keeping large values of η_{in} . For all concentrations there is a cut-off energy below which the guided mode is transformed into a leaky mode that is radiated towards the high RI substrate. Interestingly, near the cut-off energy the dispersion relation lies within the glass light cone, suggesting the possibility of excitation via prism-coupling in TIR. It should be noted that for effective medium layers thinner than 20 nm, the mode solutions are restricted to narrower energy ranges at similar values of F , as depicted in Figure 5.2. In contrast, thicker layers impose larger values of k_{\parallel} for the supported guided modes, which restricts the prism coupling excitation to incidence angles very close to $\theta \approx 90^\circ$. As a consequence, in our approach we set the layer thickness at 20 nm, assuring both strong dispersion and the possibility of prism-coupled excitation at lower incidence angles ($\theta \approx 70^\circ\text{-}80^\circ$). This selection will also allow the experimental verification with monolayers of nanoparticles with low volume to minimize their scattering cross-sections and dephasing effects. This excitation mechanism is demonstrated in Figure 5.3A and 5.3C, where the θ -dependent TE reflectivity spectra are calculated for $F = 2\%$ and $F = 8\%$, respectively. In both cases, reflectivity spectra exhibit a transition from a shallow peak at low values of θ to a pronounced dip above TIR ($\theta_{\text{TIR}} > 61^\circ$). Below this critical angle, a stationary resonance is expected at $\lambda \approx 660$ nm ($E \approx 1.87$ eV), corresponding to the LSPR of a single nanoellipsoid excited along its long axis. However, when θ_{TIR} is surpassed, the observed dip is shifted towards higher wavelengths, showing strong dispersion. In agreement with the dispersion curves of Figure 5.1D this phenomenon is more pronounced for $F = 8\%$, resulting in a total red-shift of $\Delta\lambda_{\text{LSPR}} \approx 75$ nm at $\theta = 85^\circ$. As expected, this strong dispersion is not observed when TM excitation is used, as can be observed in Figure 5.4.

Such drastic changes in the TE reflectivity spectra already suggest the existence and possibility of excitation of a guided mode. However, this effect can be unambiguously shown depicting the resonances energies of the reflectivity spectra in Figure 5.1D (dash-dotted curves). Although the high- k_{\parallel} region is inaccessible via TIR, the energy position of the reflectivity dips can match the dispersion relation of the guided mode in the vicinity of the cut-off energy for all nanoellipsoid concentrations ($F = 2\text{-}10\%$). Only at this point, the phase matching condition is fulfilled and 100% of the energy is transferred to the guided mode. The latter is clearly illustrated in Figure 5.3A and 5.3C, where the dark blue areas in the TIR region correspond to

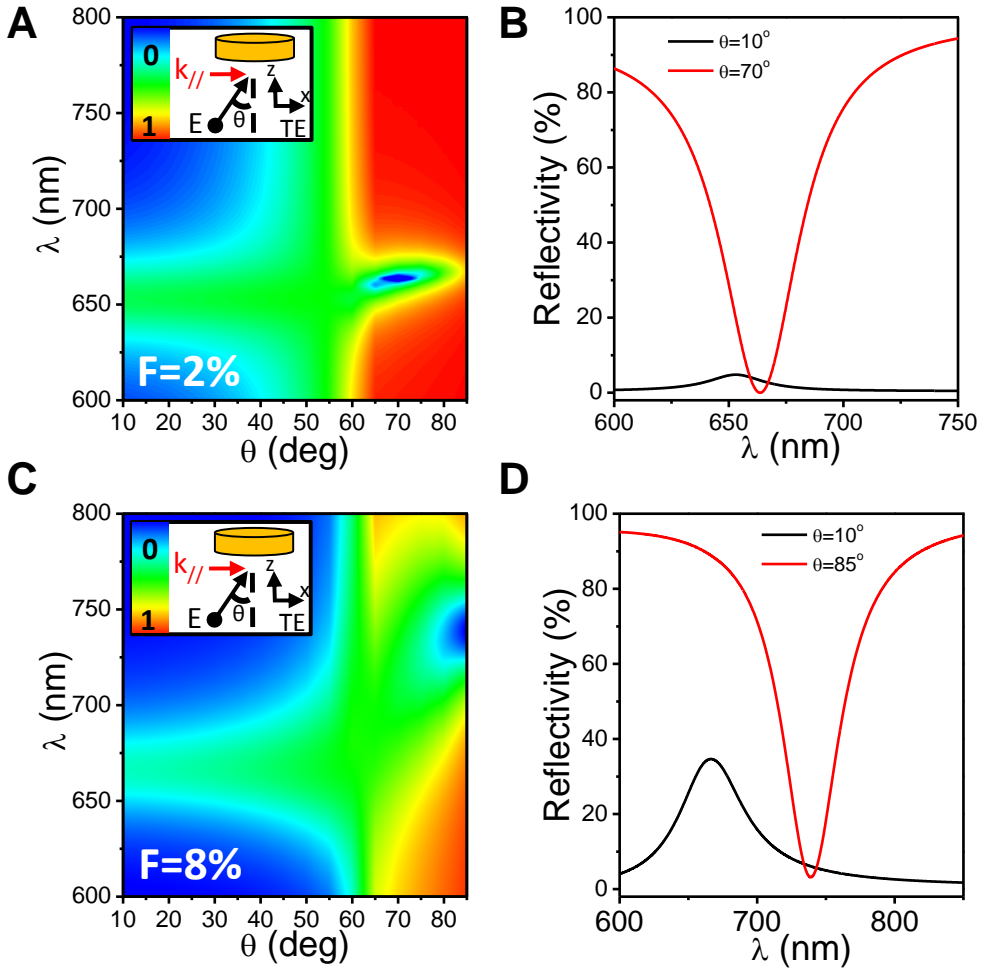


Figure 5.3: Calculated reflectivity spectra corresponding to monolayers of sparse and randomly ordered arrays of gold nanoellipsoids for $F = 2\%$ and $F = 8\%$. **(A)** TE reflectivity spectra for $F = 2\%$ as a function of the incidence angle θ and the wavelength λ . **(B)** Reflectivity spectra corresponding to $\theta = 10^\circ$ and $\theta = 70^\circ$ for $F = 2\%$, depicting the reflectivity as a function of the wavelength λ . **(C)** TE reflectivity spectra for $F = 8\%$ as a function of the incidence angle θ and the wavelength λ . **(D)** Reflectivity spectra corresponding to $\theta = 10^\circ$ and $\theta = 85^\circ$ for $F = 8\%$, depicting the reflectivity as a function of the wavelength λ .

reflectivity values close to 0%. For low concentrations this phase matching occurs at $\theta = 70^\circ$ at a wavelength that is slightly red-shifted compared to the LSPR of a single ellipsoid. In contrast, the dispersion relation at higher concentrations imposes larger values of θ and substantially longer wavelengths to satisfy the phase

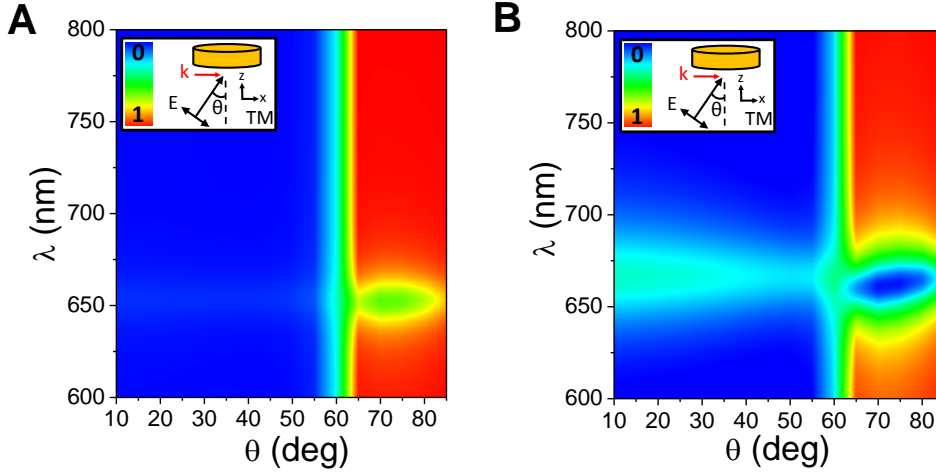


Figure 5.4: Calculated TM dispersion relations. (A) Angle-dependent TM reflectivity spectra for $F = 2\%$ and (B) $F = 6\%$, clearly demonstrating that contrary to the case of TE polarization, no mode dispersion is observed.

matching condition, thus explaining the strong red-shift of the reflectivity dip for $F = 8\%$ ($\theta = 85^\circ$). Note that for θ -values other than those corresponding to perfect light coupling, wave excitation is still possible, but the latter will occur less efficiently, resulting in less pronounced resonance reflectivity dips. The graphs in Figure 5.3B and 5.3D exemplify the extraordinary coupling of light into the guided modes, and moreover show that by using θ as a variable, the optical behavior of the effective medium can be tuned from that of an homogeneous ensemble of isolated nanoparticles, dominated by their LSPR, into a nanoplasmonic waveguiding medium characterized by extremely high levels of light absorption. This expected extraordinary degree of light uptake is unprecedented, especially considering the random ordering, low surface density, and the limited thickness (20 nm) of the modeled effective medium. In analogy, complete light absorption can also be achieved with SPPs that propagate along a planar 50 nm gold film. [44] Given the low nanoellipsoid densities ($F = 2\text{-}10\%$) needed to achieve the same result, it becomes apparent that this effective medium requires up to $125 \times$ less plasmonic material to absorb the same amount of light. Indeed, even for very low particle densities ($F = 2\%$) the absorbance of the plasmonic monolayer can be amplified from 20% at normal incidence to total absorption at $\theta = 70^\circ$ incidence, which combined with very short mode propagation makes these effective layers very suitable as light harvesting devices. Energy harvesting generally

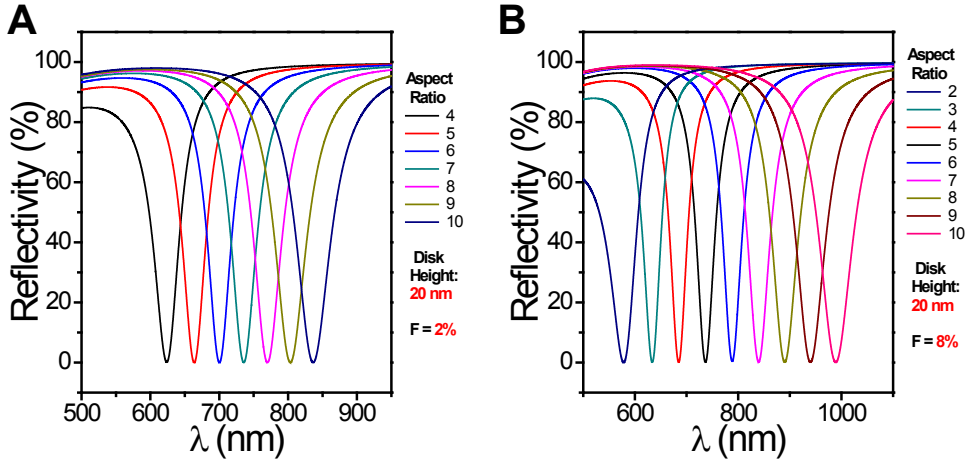


Figure 5.5: *Theoretical tunability of the absorption band using the aspect ratio of the nanodisks as a variable for (A) $F = 2\%$ and (B) $F = 8\%$.*

aims for heat generation via nano-scale energy confinement, requiring the employed plasmonic structures to be tunable over a broad spectral range, thereby maintaining their light absorption efficiency. [199] Interestingly, the total absorption band can be tuned over the entire visible and NIR spectral ranges by changing the AR, density or composition of the employed nanoellipsoids, as well as the external RI. This spectral tuning using the AR as a variable is theoretically shown in Figure 5.5. Herein, we maintained the thickness of the effective medium layer constant at 20 nm, and used the AR as the desired tuning parameter. The depicted reflectivity spectra for each value of AR correspond to θ -values that assure perfect phase matching, and hence, 100% energy transfer of the incidence light into the guided mode. Although it can be observed that for both analyzed values of F , the absorption band can be spectrally tuned along a wide range of the VIS and NIR light spectrum, it becomes apparent that for small nanodisks ($AR < 4$) at low concentrations ($F = 2\%$) the effective RI of the MG effective medium becomes too small to support guided waves, explaining the absence of absorption bands at these ARs.

5.2.2 Bulk Sensitivity Analysis

Another property that highlights the drastic change of the optical properties when the guided mode is excited is embodied by η_B , that is, the sensitivity of the nanoplasmonic

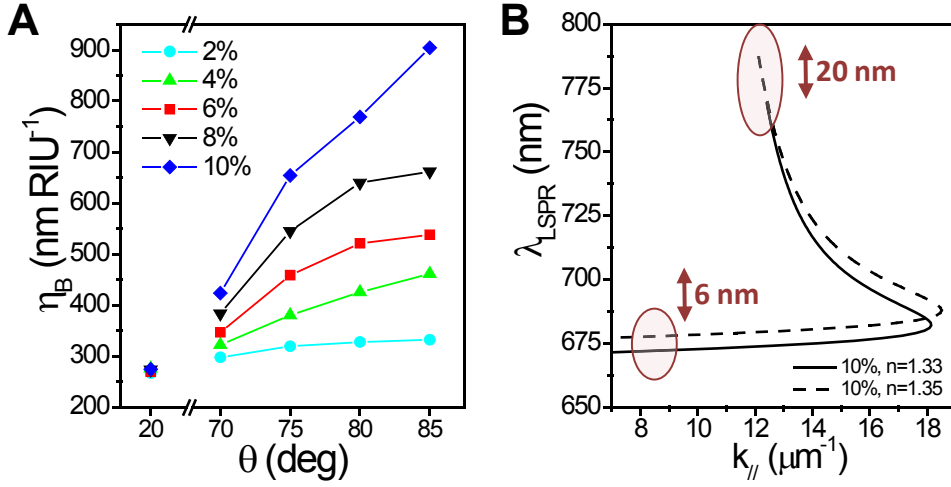


Figure 5.6: Theoretical bulk sensitivity analysis for monolayers of sparse and randomly ordered arrays of gold nanoellipsoids ($F = 2$ -10%). (A) Bulk sensitivities η_B calculated for $F = 2$ -10% as a function of the incidence angle θ . (B) Calculated spectral mode dispersion curves ($F = 8\%$), depicting the resonance wavelength λ_{LSPR} as a function of the wave-vector $k_{||}$ for bulk dielectric environments given by $n = 1.33$ (straight line) and $n = 1.35$ (dashed line).

MG effective medium layer to RI changes of the external dielectric medium, which constitutes the well-known basis of biosensing applications. In Figure 5.6A η_B is calculated as a function of both the θ and F . As can be observed in this figure, below the critical angle, η_B exactly fits the sensitivity of a single nanoellipsoid, the latter given by $\eta_B \approx 275 \text{ nm} \cdot \text{RIU}^{-1}$, [200] being in agreement with the localized nature of the resonance in this regime. Most interestingly, once the waveguiding behavior sets in, η_B shows an extraordinary increasing trend. Clearly, this sensitivity enhancement is more pronounced for larger particle densities, surpassing $\eta_B \approx 900 \text{ nm} \cdot \text{RIU}^{-1}$ for $F = 10\%$ at $\theta = 85^\circ$, resulting in a more than 3-fold amplification of η_B with respect to isolated nanoellipsoids. Such sensitivity amplification is a clear sign of the waveguiding behavior, as can be deduced from the variation of the dispersion relation of the guided mode under a RI change, as depicted in Figure 5.6B. Herein, the dispersion relation is calculated for $F = 10\%$, depicting λ_{LSPR} as a function of $k_{||}$ for bulk dielectric environments given by $n = 1.33$ (straight line) and $n = 1.35$ (dashed line). In the low $k_{||}$ regime, where λ_{LSPR} is expected to be of localized nature, the expected red-shift caused by the change of RI equals $\Delta\lambda_{LSPR} \approx 6 \text{ nm}$, thereby being approximately the same as the bulk sensitivity of a single nanoellipsoid

($\eta_B \approx 300 \text{ nm}\cdot\text{RIU}^{-1}$). In contrast, close to the cut-off wavelength, where the guided mode can be excited perfectly, the change in the dispersion relation generates a red-shift which is more than three times larger: $\Delta\lambda_{\text{LSPR}} \approx 20 \text{ nm}$. This explains the drastic enhancement of η_B upon mode excitation. Next to such valuable amplification of η_B , the extremely pronounced dips achieved when the phase matching condition is fulfilled also have striking effects on the S/N of biosensing measurements, even with very low density of plasmonic nanoparticles, as will be demonstrated in the experimental results that will follow in the next section.

5.3 Experimental Results

In order to experimentally proof the presented theoretical results, short-ordered arrays of gold nanodisks ($D = 100 \text{ nm}$, $H = 20 \text{ nm}$) with different nanodisk surface densities were prepared on SiO_2 substrates by hole-mask colloidal lithography (For further details, we refer to Section 2.1.2.1). The θ -dependency of the nanodisk samples was investigated by carrying out reflectivity measurements (For further details, we refer to Section 2.2.3.2).

5.3.1 Experimental Mode Dispersion and Reflectivity Spectra

Figure 5.7A and 5.7B show the experimental TE reflectivity spectra as a function of θ for two nanostructured layers of gold nanodisks with distinct nanodisk surface densities, given by $F \approx 5\%$ (sample A) and $F \approx 7.5\%$ (sample B). These results clearly exemplify all predicted signatures related to the excitation of guided modes. Firstly, the shallow reflectivity peaks located at $\lambda_{\text{LSPR}} \approx 710 \text{ nm}$ below the critical angle, which correspond to the λ_{LSPR} -value of a single nanodisk seating on glass, are transformed into profound dips in TIR. This transformation is accompanied by a substantial red-shift of the dip position for increasing values of θ , given by $\Delta\lambda_{\text{LSPR}} \approx 44 \text{ nm}$ (sample A) and $\Delta\lambda_{\text{LSPR}} \approx 75 \text{ nm}$ (sample B) at $\theta = 85^\circ$. This experimental dispersion relation is depicted in Figure 5.7C in energy-scale, where the encircled points correspond to reflectivity spectra where the phase matching condition is satisfied, resulting in almost zero reflection. The amount of scattered light trespassing the nanodisk arrays is extremely small compared to the light used for mode excitation, as shown by the normalized reflectivity and transmission spectra displayed in Figure 5.8 for sample A at $\theta = 85^\circ$. It is therefore safely to state that almost all in-coupled light is harvested by these nanostructured layers, yielding extremely

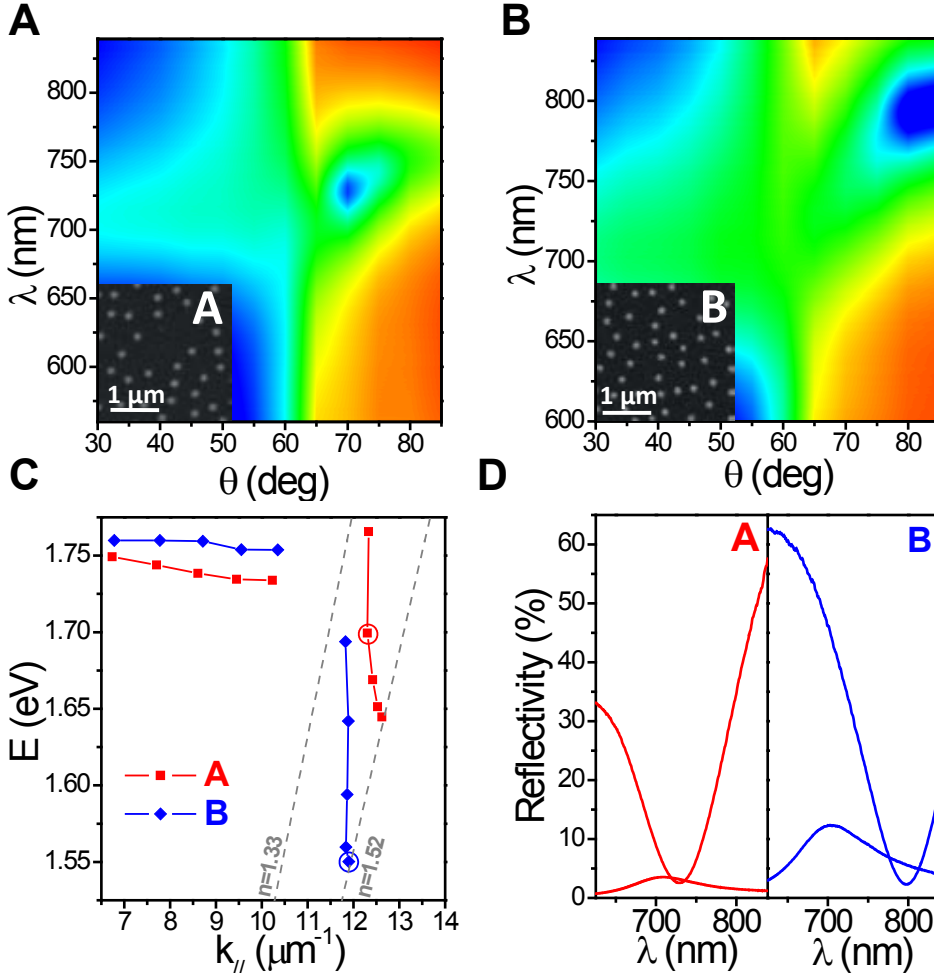


Figure 5.7: Experimental dispersion relations corresponding to sparse nanodisk arrays with disk densities given by $F = 5\%$ (Sample A) and $F = 7.5\%$ (Sample B). **(A)** TE reflectivity spectra showing the reflectivity as a function of the incidence angle θ and the wavelength λ , together with SEM image (inset) for nanodisk Sample A and **(B)** Sample B. **(C)** Experimental dispersion relations corresponding to the reflectivity spectra of samples A and B, depicting the resonance energy E as a function of the wave-vector $k_{||}$. **(D)** Dip-shaped reflectivity spectra upon perfect mode excitation for Sample A ($\theta = 70^\circ$) and Sample B ($\theta = 85^\circ$), together with their peak-shaped spectral response obtained at $\theta = 30^\circ$.

high absorbance coefficients of approximately 96%-97% (Figure 5.7D). Note that all the experimental results are red-shifted with respect to the theoretical predictions due to near-field interaction of the nanodisks with the substrate, which is not taken

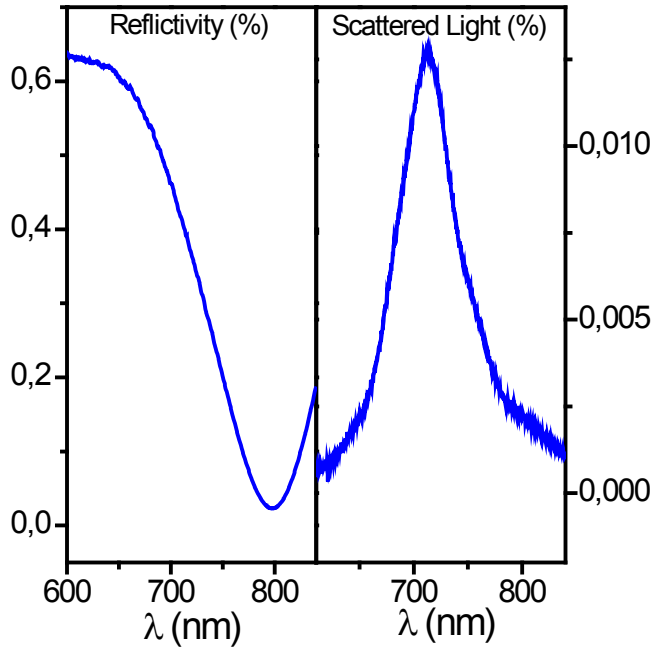


Figure 5.8: *Experimental Spectra taken at $\theta = 85^\circ$, depicting the reflectivity (Left Panel) and the transmitted light (Right Panel) for Sample B ($F = 7.5\%$) normalized with respect to the broadband white light excitation spectrum.*

into account in the MG formalism. Furthermore, compliant to the expectations, no mode-dispersion is observed for the TM polarization, as can be clearly observed in Figure 5.9, where the θ -dependent TM reflectivity spectra are shown for samples A and B. Conclusively, this observed spectral behavior undisputedly shows the different response exhibited by the nanodisks depending on the excitation conditions.

5.3.2 Experimental Bulk Sensitivity Assessment

The waveguiding behavior is further demonstrated by the drastic changes of η_B -values caused by RI changes of the dielectric surrounding. To this end, an assessment of η_B was carried out for nanodisk samples with different particle surface densities, by carrying out real-time and in-flow reflectivity measurements, thereby varying ($\Delta n = 0.02$ RIU) the bulk dielectric surrounding of the nanodisks (For further details, we refer to Section 2.3). Figure 5.10A shows that below the critical angle

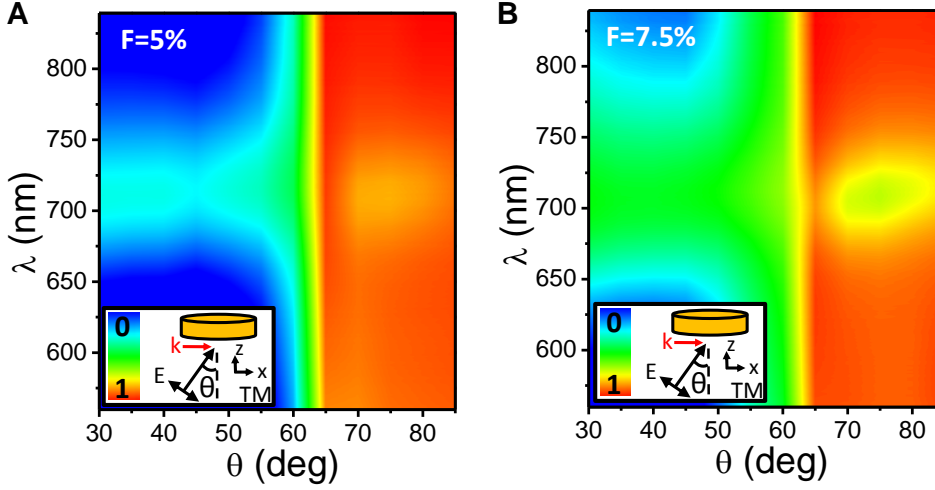


Figure 5.9: *Experimental TM dispersion relations corresponding to sparse nanodisk arrays with disk densities given by (A) $F = 5\%$ and (B) $F = 7.5\%$. The angle-dependent TM reflectivity spectra show that, contrary to TE polarization, no dispersion of the mode is observed.*

$\eta_B \approx 150 \text{ nm} \cdot \text{RIU}^{-1}$, being comparable to the bulk sensitivity of similar nanodisk arrays fabricated on SiO_2 . [179, 200] As a direct result of the interaction of the nanodisks with the high RI SiO_2 substrate ($n = 1.52$), this value is substantially smaller than the theoretical η_B -values of a nanoellipsoid totally surrounded by H_2O . [180] Interestingly, the bulk sensitivity in TIR (at $\theta = 80^\circ$) for TM polarized light is similar to the η_B -value corresponding to low angle TE measurements, as shown in Figure 5.10A, which underlines the localized behavior of the nanodisks for this polarization and the impossibility to excite guided modes. In contrast, Figure 5.10A shows that once the modal dispersion regime is launched in TIR for TE polarization, a steep rise of η_B is measured, increasing for larger values of θ , with an overall larger η_B -enhancement for higher values of F . Strongly influenced by the mode propagation at high incidence angles, it becomes thus possible to experimentally achieve an exceptional four-fold increase of η_B for sample B, that is, the sample with the highest nanodisk surface density ($F \approx 7.5\%$). The real-time measurement traces of both nanodisk samples A and B, corresponding to their highest measured value of η_B (at $\theta = 85^\circ$), are depicted in Figure 5.10B, thereby unambiguously illustrating this strong improvement of the sensing performance. Consequently, these guided modes in random arrays of gold nanodisks profile themselves as very promising sensing

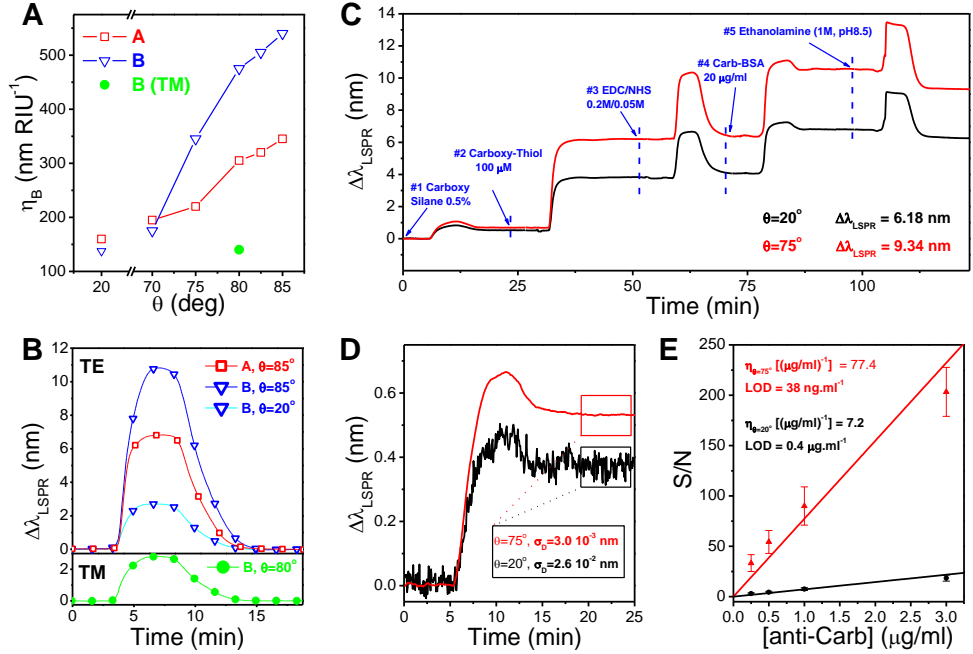


Figure 5.10: Experimental results involving label-free bulk- and biosensing features. (A) Angle-dependent TE and TM bulk sensitivities η_B of nanodisk arrays with disk densities given by $F = 5\%$ (Sample A) and $F = 7.5\%$ (Sample B). (B) Tracking of the spectral resonance shifts $\Delta\lambda_{LSPR}$ for Sample A ($\theta = 85^\circ$) and Sample B ($\theta = 20^\circ$, $\theta = 85^\circ$, $\theta = 80^\circ$ /TM) as a function of time. (C) Real-time simultaneous tracking ($\theta = 20^\circ$ and $\theta = 80^\circ$) of the spectral resonance shift $\Delta\lambda_{LSPR}$ corresponding to the 5-step immobilization protocol of Carb-BSA. (D) Detection curves of anti-Carb [$3 \mu\text{g}\cdot\text{mL}^{-1}$] at $\theta = 20^\circ$ & $\theta = 80^\circ$, showing the time-dependent resonance shift $\Delta\lambda_{LSPR}$. (E) Calibration curve of the anti-Carb detection assay, depicting the signal-to-noise ratio S/N as a function of the antiCarb concentration.

platforms for real label-free biosensing applications.

5.3.3 Carb/Anti-Carb Immunoassay

On the other hand, even more important than the amplification of the sensitivity, the transition from weak reflectivity peaks below the critical angle into extremely profound dips in TIR can provide outstanding enhancements of the S/N for biosensing measurements. To illustrate this capability of guided modes we selected a low density nanodisk monolayer ($F \approx 5\text{-}6\%$) and carried out a biosensing immunoassay, based on the specific detection of monoclonal antibodies previously produced against carbaryl (Carb), [201–203] a relevant and widely used pesticide (For further details, we refer

to Section 2.4.3). For these experiments, simultaneous real-time monitorization of $\Delta\lambda_{\text{LSPR}}$ was conducted at two different values of θ , given by $\theta = 20^\circ$ and $\theta = 75^\circ$, using the same white light illumination intensity and identical acquisition conditions (For further details, we refer to Section 2.2.3.2). Based on previously discussed results, $\theta = 20^\circ$ corresponds to a regime dictated by the LSPR of isolated nanodisks, while effective excitation of a guided mode is guaranteed at $\theta = 75^\circ$. In order to create a self-assembled biological receptor layer for the specific detection of the antibody (anti-Carb), a five-step covalent immobilization protocol was carried out, whose corresponding real-time tracking of $\Delta\lambda_{\text{LSPR}}$ is shown in Figure 5.10C. As can be observed, $\Delta\lambda_{\text{LSPR}}$ is approximately 50% larger in TIR, which fits the expected enhancement of the sensitivity at that nanodisk concentration and illumination angle (Figure 5.10A), proving the improved sensing performance of the guided modes. However, next to the larger absolute $\Delta\lambda_{\text{LSPR}}$ -values measured at $\theta = 75^\circ$, this signal exhibits a noise level as low as 3 pm, despite of an acquisition performed with a low cost portable CCD spectrophotometer at room temperature with short integration time (< 1 sec), and the employment of only one third of the pixels in the tracking algorithm. In Figure 5.10D, where simultaneous immunodetection signals of anti-Carb ($3 \mu\text{g}\cdot\text{mL}^{-1}$) at $\theta = 20^\circ$ and $\theta = 75^\circ$ are depicted, such dramatic noise suppression is nicely exemplified. The calculated standard deviations for both θ -values are given by $2.6\cdot 10^{-2}$ nm and $3.0\cdot 10^{-3}$ nm, showing a noise level difference of more than one order of magnitude favouring the higher incidence angle. This strong noise decrease is caused by the larger absolute signals of the resonance dips when perfect phase matching is achieved. Despite of the almost perfect absorption band in TIR configuration, the total amount of photons used in the tracking algorithm is $30\times$ larger than below the critical angle. Since the noise level sets a limit to the discrimination of the smallest possible value of $\Delta\lambda_{\text{LSPR}}$, the S/N is the desired variable to characterize the sensing performance of these nanoplasmonic structures. Following this path, and exploiting the regeneration potential of the immobilized biological receptor layer, detection of anti-Carb was carried out for a range of different concentrations varying between $0.25 \mu\text{g}\cdot\text{mL}^{-1}$ and $3 \mu\text{g}\cdot\text{mL}^{-1}$. The obtained calibration curve, depicting S/N as a function of the antibody concentration is shown in Figure 5.10E. Here, it can be seen that for $\theta = 75^\circ$, a much high slope is measured, and hence, an improved sensing performance compared to the value obtained for $\theta = 20^\circ$ can be extracted. From these sensing performances, quantitatively expressed by the slope of the graph, and given by $7.2 (\mu\text{g}/\text{mL})^{-1}$ for $\theta = 20^\circ$ and $77.4 (\mu\text{g}/\text{mL})^{-1}$ for $\theta = 80^\circ$, a S/N enhancement of more than one order of magnitude can be deduced. From this, a corresponding LOD,

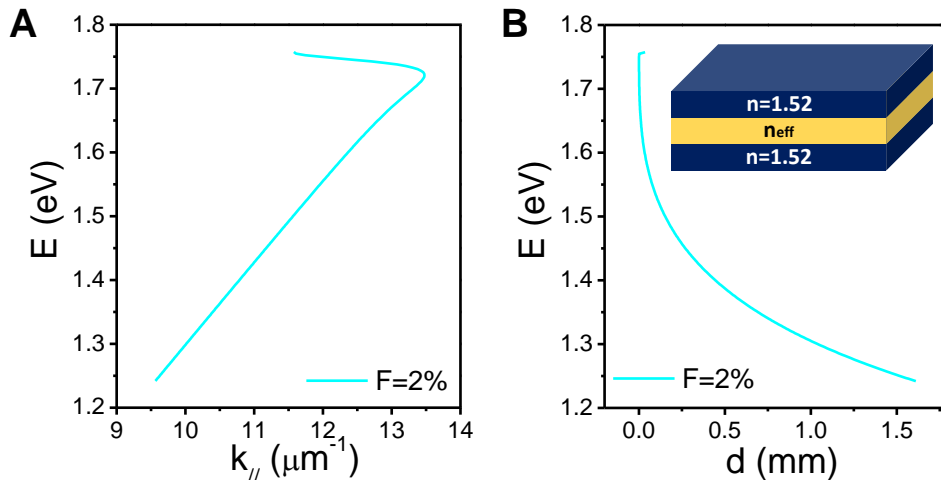


Figure 5.11: Mode properties of a 20 nm thick effective monolayer ($F = 2\%$) comprised between two equal dielectric media ($n = 1.52$). (A) TE Dispersion Curve. (B) Energy dependent propagation distance of the TE guided mode.

defined as three times the noise level, as low as $38 \text{ ng}\cdot\text{mL}^{-1}$ can be calculated. The response of this system thus shows the great potential that the guided modes in these sparse arrays of gold nanodisks have as biosensing platforms.

5.4 Discussion and Conclusion

It should be noted that the novel guiding mechanism presented in this chapter is not restricted to gold nanodisks and can be extrapolated to any sparse and random distribution of plasmonic nanoparticles, such as nano-prisms, nano-rods or core-shell nanostructures. The inherent higher η_B of these nanostructures when compared to nanodisks, allows for the expectation of unprecedented sensitivities when the guided mode is launched. In addition, the waveguiding concept based on monolayers of plasmonic nano-disks could also be expanded to achieve more exotic nanophotonic features with the introduction of plasmonic meta-molecules, such as interacting plasmonic dimers, [173,200] or nanosandwiches. [204,205] These hybrid systems could combine the generation of additional effective birefringence effects, the creation of EM hotspots or dark modes within the meta-molecules, with the excitation of the guided mode to amplify light-matter interaction, thus opening the path to envisage novel nanophotonic applications in light harvesting, biosensing or enhanced light

emission/detection. Finally, it is worth noticing that the propagation distance of the analyzed guided modes can be substantially enhanced in a homogeneous configuration with similar RI in substrate and cladding layers. In this configuration propagation distances larger than one millimeter are expected even for very low concentration nanoparticles for wavelengths in the NIR, as shown by Figure 5.11, thus enabling integrated-optics applications.

Chapter 6

Towards a LSPR Biosensor with Multiplexing Capabilities

Herein, the great biosensing potential of short-range ordered arrays of Au nanodisks is exploited for the fabrication of stand-alone and user-friendly LSPR biosensors. We present a highly miniaturized and stable high-angle excitation LSPR sensor with a single flow channel. Next, this concept is taken a step further, thereby adding multiplexing capabilities to the sensing platform. To this end, a new measuring scheme is designed, whose (ongoing) development process is discussed extensively. This measuring setup is compatible with in-house fabricated Polydimethylsiloxane (PDMS) microfluidics and possesses multiple flow channels that can be subsequently interrogated via motorized optics.

6.1 Introduction

In the previous chapters we have shown that the sensing performance of short-range ordered arrays of Au nanodisks have great potential for biosensing applications. Redistribution of the EM near-field resulted in enhanced RI sensitivities, while the far-field radiation could be improved via the excitation of guided TE modes in these thin layers of plasmonic material. The latter gave rise to very competitive biosensing LODs, being directly caused by a great improvement in S/N. However, as becomes apparent by simply looking at the photographs of the measurement setups described in Chapter 2, all these experiments involved proof-of-concepts, characterized by very basic and bulky equipment, mounted on large optical tables. Logically, these devices are not viable for out-of-laboratory use. For this to be possible, compact devices are preferred in which the used (non-)optical components are integrated to the utmost extent, thereby creating a compact device with a minimum number of adjusting variables in order to increase its robustness and ease-of-use. With these things in mind, we created a both compact and low-cost, stand-alone, single-channel, and easy to use LSPR biosensor, that allows for real-time data read-out. This apparatus, currently used for the execution of extensive biosensing assays in the laboratory, clearly exemplifies the potential for the creation of compact and integrated LSPR sensing platforms, that could be commercialized in the near future. This device, containing both commercial and custom-made components, in combination with an in-house developed software program for real-time data readout, is described in Section 6.2. Currently, we took this idea a step further, trying to add another interesting and potential property to the device: **multiplexing capabilities**. Although this device still finds itself in a state of development, the pathway describing the fabrication of biosensor is discussed in Section 6.3 Herein, we will focus on the design of the sensor, its fabrication, the software and the combination of the Au nanodisk sample fabrication together in-house fabricated PDMS microfluidics.

6.2 Miniaturized High-Angle LSPR Sensor

Exploiting both the enhanced sensitivity and the improvement in S/N that are obtained when the TE guided mode of short-range ordered arrays of Au nanodisks is excited at high angles of incidence (θ), a miniaturized system based on these results was devised for extensive laboratory use. Top-view and bird-view photographs of this system are shown in Figures 6.1A and 6.1B, respectively. Based on the experimental

outcome dictating that both η_B and η_S increase for larger θ , we designed two systems based on an excitation angles given by $\theta = 70^\circ$ and $\theta = 80^\circ$, since these angles assure good trade-off between high measurement angles and non-deformed light spots reaching the nanodisk substrate. Here, the design and working of this sensing concept will be illustrated by the hand of the LSPR sensor in which an angle of $\theta = 70^\circ$ is used. For this sensor, a triangular aluminum platform was created, as depicted in Figure 6.1A, with lateral sides designed at an angle of $\theta = 70^\circ$. On this platform, next to the attachment of a custom-made flow cell (#7, Delrin, $V = 5 \mu\text{L}$) and a specifically designed trapezoidal prism (#4, FocTek, BK7, $\theta = 70^\circ$), rails are attached for the mounting of the optical components necessary for the TE mode excitation and the collection of the reflected light. These optical rails are attached perpendicular to the lateral sides of the aluminum base platform, thereby assuring incoming and outgoing optical paths at an angle given by $\theta = 70^\circ$. The combination of all optical components mounted on the left of the base platform, assure the excitation of the TE plasmonic mode with a collimated broadband light source. To this end, the light source is fiber-coupled to a multi-mode fiber with a small core (#1, Thorlabs, $\varnothing_F = 50 \mu\text{m}$, M14L01) to decrease the size of the resulting light spot and subsequently collimated with a collimation lens (#2, Thorlabs, C330TME-B) mounted inside a lens tube. It should be noted that the fiber is mounted on a platform that allows for tilt-correction. Finally, the collimated light beam is polarized (TE) with a UV-VIS polarizer (#3, Thorlabs, LPVIS050). The reflected light is collected by a fiber-coupled (Thorlabs, $\varnothing_F = 1 \text{ mm}$, M35L01) light collection lens (#6, Thorlabs, F230SMA-B), that is attached to a XY translator mount (#5, Thorlabs, SCP05) in order to allow for the manual optimization of the collected light signal. Spectral analysis is carried out with a low-cost, CCD spectrometer (Ocean Optics, Spectrasuite Jaz Module). Once the signal acquisition is optimized, all manually adjustable components can be blocked to increase the robustness of the sensors, and avoid problems regarding misalignment.

Given the fact that both optics rails and the prism are fabricated at the same angle, light enters and leaves the prism normal to its lateral sides. As a direct consequence, the simplicity of the system is further enhanced, by providing a relatively large margin in the x-direction for the placement of the prism (precise centering of the prism is not necessary). Nanodisk samples are clamped between the prism and the flow cell, while sealing is assured with a thin parafilm layer that contains an opening whose shape and size approximately resemble that of the flow channel. Complete sealing of the fluidics is achieved by applying a light pressure on the prism with the depicted screw. The flow cell and the microfluidics are connected by two M6 screw flow

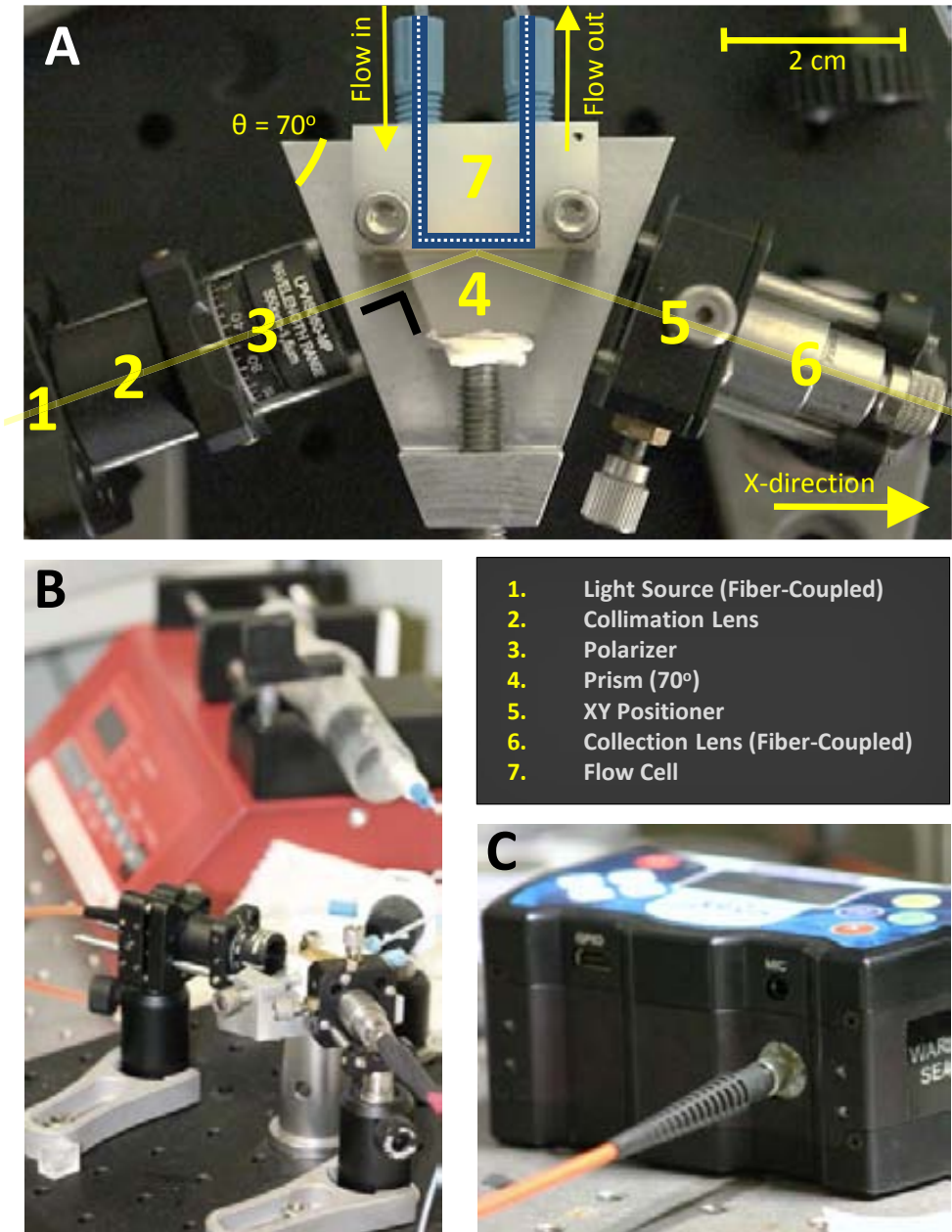


Figure 6.1: (A) Top-view and (B) bird-view photographs of the miniaturized high-angle LSPR sensor, together with (C) an image of the Jaz Module CCD spectrometer.

connectors that assure proper in- and outflow of liquid in the system. As can be seen in Figures 6.1A and 6.1B, the optical components and a (not displayed) manually operated injection valve (IDEX Health and Science, V-451), do not occupy more than 100 cm², and are mounted on a portable 20 cm × 20 cm portable breadboard, illustrating the portability and the small size of the system. However, several external - not integrated - components such as a syringe pump (Figure 6.1B, New Era, NE-1000), a halogen light source (Micropack, HL-2000) and the employed spectrometer (Figure 6.1C) are still needed for the proper functioning of the system. Whereas the sizes of the light source and the spectrometer are small and allow for potential further system-integration into a *black box*, a more elegant alternative should be found for the large and bulky syringe pump.

6.2.1 Standalone Real-time Readout Software

In the proof-of-concept measurements, documented in Section 2.2.3, and whose results are discussed in Chapters 4 and 5, extraction of the relative - and time-dependent - spectral LSPR peak position ($\Delta\lambda_{\text{LSPR}}$) was carried out *a posteriori*, that is, after the measurements were finished. For this, a high-degree polynomial was fitted to the previously acquired reflectivity spectra, [154] using a script made with the commercially available Wolfram Mathematica software. The obtained reflectivity spectra were obtained by addressing the CCD spectrometer with a commercial software issued by the spectrometer manufacturer (Ocean Optics, Spectrasuite Software). Obviously, this process does not improve the usability of the sensing platform, since besides the fact that two independent software packages need to be used for data acquisition and analysis, the involved processes are complicated, thereby offering the user a non-intuitive and very poor user interface. Besides, the *a posteriori* data treatment does not offer real-time information to the user, since $\Delta\lambda_{\text{LSPR}}$ typically embodies sub-nanometer values that are not observable by simply looking at the resonance peak with the naked eye. The latter makes a measurement extremely time-consuming, since regardless of the outcome of an experiment, a user is forced to wait until a measurement is finished before he or she can rationally assess its result.

To overcome these problems and provide the user with a simple and friendly user-interface that allows for real-time data analysis, a standalone software executable was created that integrates both the acquisition of the reflectivity spectra and the real-time extraction of $\Delta\lambda_{\text{LSPR}}$. The software program was written in a Labview environment

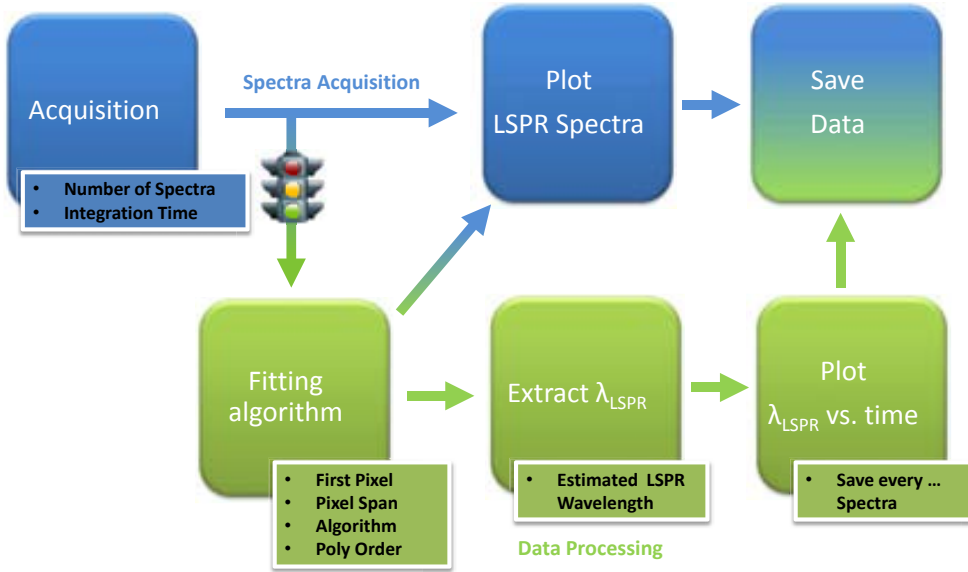


Figure 6.2: Flow diagram depicting the logic of the employed software.

(Labview 2010, National Instruments), exploiting the provided DLL driver database of the employed spectrometer. Figure 6.2 displays the schematics corresponding to the implemented software logic. First, the spectrometer is addressed in order to acquire a spectrum. For this, the spectrometer only needs to receive a desired integration time, being the exposure time of a single spectrum, and the number of accumulated spectra for a single acquisition. These accumulative spectra are then automatically plotted, as shown in a screenshot of the user interface in Figure 6.3A (blue line), and can be saved if required. By triggering the fitting algorithm, a polynomial can be fitted to the acquired spectrum. This fitting process can be optimized using four parameters. The *First Pixel* and *Pixel Span* parameters determine the range of CCD pixels on which the fitting algorithm is executed. In our case, this pixel range, that is dictated by the employed spectrometer, can vary between 1 and 2048. Furthermore, the *Algorithm* parameter points towards one of the fitting algorithm provided by Labview (0-5), while the *Polynomial Order* defines the order of the polynomial. The resulting fit is then displayed as a function of the wavelength, in the same plot as the data provided by the spectrometer (Red line, Figure 6.3A). From the resulting polynomial fit, the resonance can be extracted by calculating the wavelength corresponding to the extremes of the fitted peak. To noticeably simplify this calculation an *Estimated LSPR wavelength*

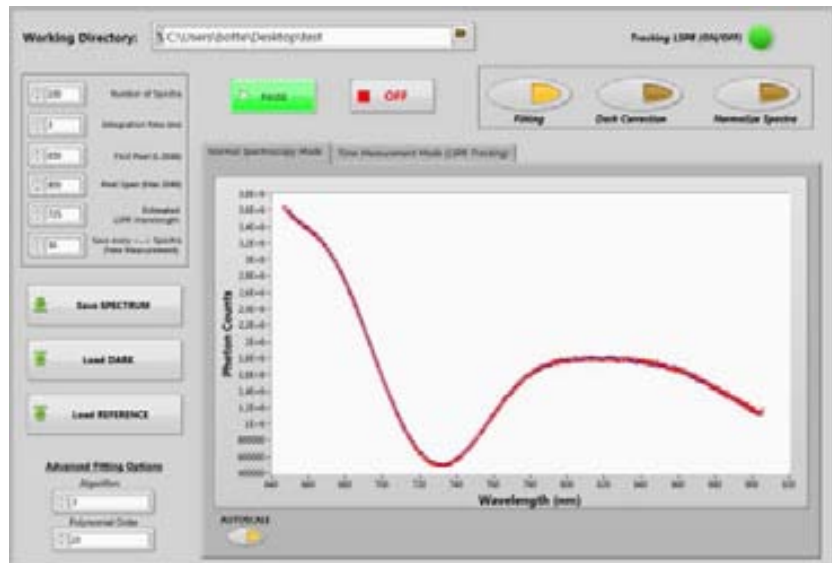
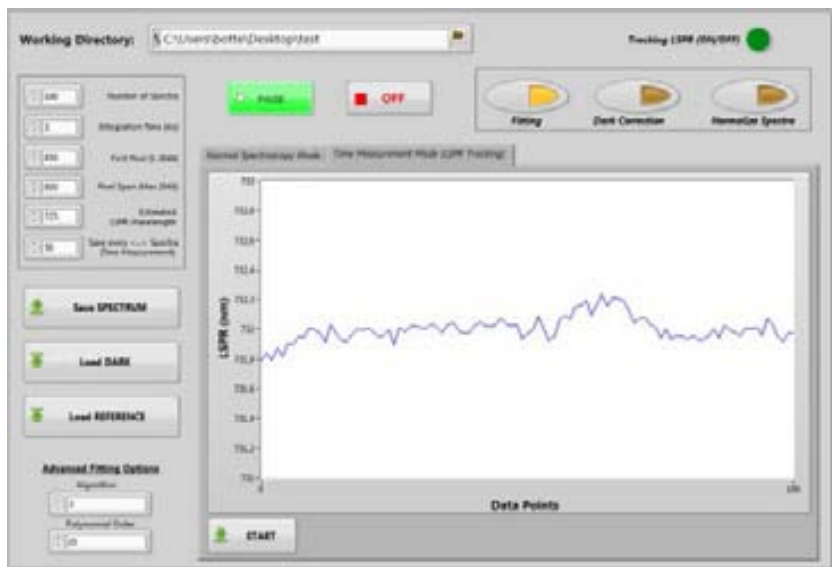
A**B**

Figure 6.3: Screenshots of the standalone software program depicting the (A) spectroscopy mode and (B) the time measurement mode.

needs to be provided by the user. These calculated resonance positions can then be saved and displayed as a function of time, as shown by Figure 6.3B. Furthermore, the software contains two other non-discussed parameters, namely *Dark Correction* and *Normalized*. When enabled, the former option subtracts a previously stored dark spectrum from the data received from the spectrometer, while the latter option divides the data received by from the spectrometer by a previously stored reference spectrum. If no dark or reference spectrum is stored/loaded, they are replaced by arrays filled with zeros or ones, respectively, thereby not affecting the raw data delivered by the spectrometer. In conclusion, this very intuitive program integrates both the acquisition and the time-dependent extraction of $\Delta\lambda_{\text{LSPR}}$. This is done by limiting the number of user-manageable variables to a number as low as 8, creating a very user-friendly environment for the execution of extensive biosensing assays.

6.3 Towards a Multiplexed LSPR Sensor

After creating a stand-alone and robust LSPR sensor with a single sensing channel, we tried to take this sensing concept to a next level by adding multiplexing capabilities to the devised LSPR sensing platform. Multiplexing allows the parallel read-out of several sensing spots in a simultaneous or quasi-simultaneous manner, thereby allowing for high-throughput sample analysis. Although different options can be implemented for multiplexing, such as for example the use differently functionalized and subsequently immobilized nanoparticles, or sensing platforms based on contrast measurements of different immobilized sensing spots, such as applied in SPI, in our approach, we opted for the creation of microfluidic channels on top of our nanostructured substrates, for which we devise a scanning methodology that enables the spectral interrogation of each channel in a subsequent manner. This way, every channel can be used as an independent channel for studies that involve biomolecular interactions. In this section, we describe our approach towards the creation of such a device.

6.3.1 Fabrication

Herein, we opt for the fabrication of a device, whose conceptual schematics are shown in Figures 6.4A and 6.4B. First, we consider a rectangular substrate on which short-range ordered arrays of Au nanodisks are fabricated via HCL. Placement of a prism ($\theta = 70^\circ$) underneath the substrate proclaims a geometry that allows for TIR

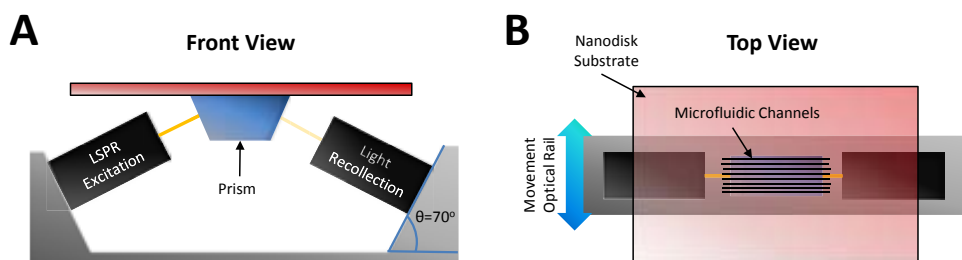


Figure 6.4: Schematics depicting the working concept of the LSPR biosensor with multiplexing capabilities.

excitation and the subsequent collection of the reflected light from below the nanodisk substrate. This can be accomplished by mounting the necessary optics for LSPR excitation and light collection on fixed optical rails, the latter being positioned at the same incidence angle as the prism (Figure 6.4A). As a direct consequence, light enters and leaves the prism at normal angle with respect to its lateral planes. Then, after fabrication of microfluidic channels on top of the nanostructured surface, movement of the optical axis, in a direction normal to the microfluidic channels (Figure 6.4B), should enable the possibility of scanning each of the flow channels in a subsequent manner.

6.3.1.1 Design

To implement this methodology, a design was made, whose schematics are depicted in Figures 6.5A and 6.5B. As can be seen in the figure, the measurement scheme consists of 3 independent parts. First, there is a prism holder, attached to a vertical translation stage for vertical movement of the prism, opening up a path to contact the prism to the lower part of the Au nanodisk array via RI matching oil or a more rigid optical gel (Cargille, 081160, $n = 1.517$). Next, there is an aluminum stage - supported by 4 posts - meant to act as a holder for the rectangular Au nanodisk substrate, the latter being clamped between the aluminum stage and a PMMA component. This piece of PMMA serves as a bridge between the PDMS microfluidics located on top of the nanodisks sample (Section 6.3.3) and the external flow tubing. Besides 12 M6-threaded holes for the creation of 8 horizontal and 1 vertical flow channels (Section 6.3.3), 6 additional holes are fabricated for the introduction of small magnets. These magnets are attracted to six other magnets located inside the aluminum stage. The attractive force between those magnets is supposed to seal the nanostructured

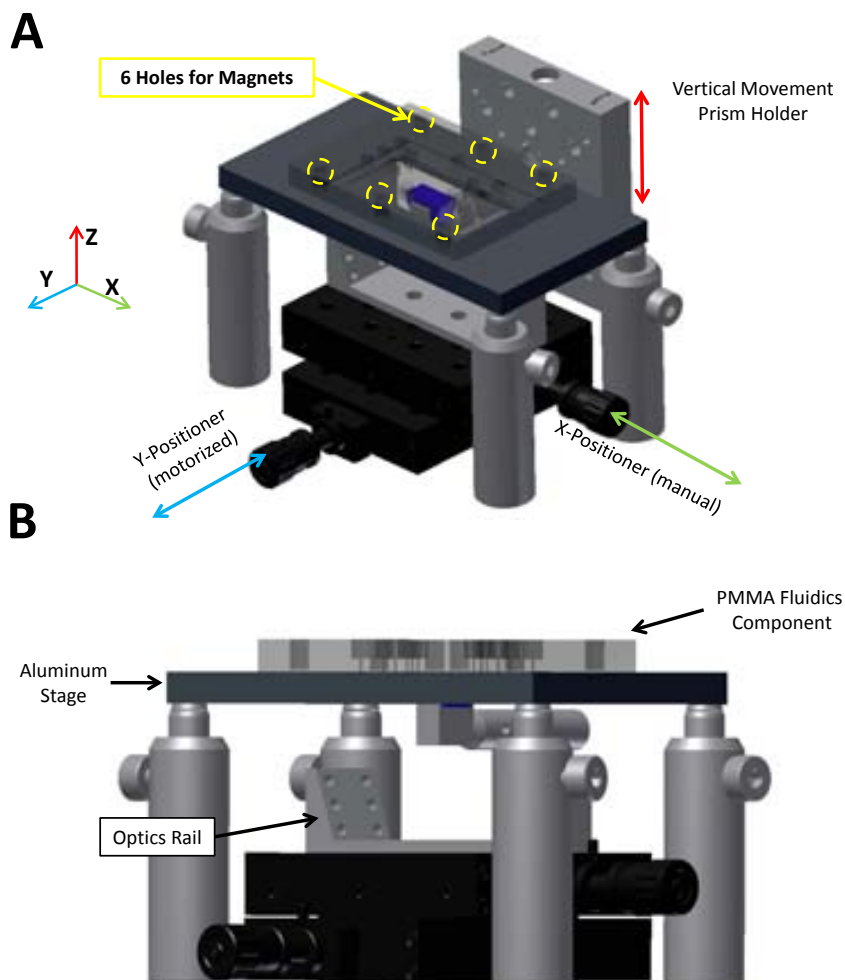


Figure 6.5: (A,B) Three-dimensional design drawings of the LSPR biosensor device, illustrating its different components.

sample and the PDMS microfluidics located on top of the latter, thereby preventing any leakage of liquid. The last part of the system consists of two translation stages located below the prism, that serve for the attachment of the optical rail. The manual stage assures movement in the x-direction, in order to center the excitation and light collection optical paths with respect the prism. Next, a motorized translation stage that moves in the y-direction is introduced for the mechanical movement of the optical components, thereby scanning the microfluidic channels subsequently.

6.3.1.2 Instrumentation

The assembly of all the custom-made components described in the previous section, together with the necessary commercially available optical components, resulted in a device, whose photograph is depicted in Figure 6.6A, resembling in every bit the intended design (Figure 6.5). Also, it can be observed that we opted for the low cost CCD spectrometer (Figure 6.1C), while a more detailed image of the fabricated PMMA fluidics component is shown in Figure 6.6B. Furthermore, it can be observed in Figure 6.6A that movement in the y-direction is motorized via the use of a single-axis translation motor (Thorlabs, PT1/M-Z8). A detailed photograph, depicting the optical paths for LSPR excitation and light collection is shown in Figure 6.6C. In a similar manner as described in Section 6.2, two optical paths responsible for LSPR excitation and collection of the reflected light, are centered at a specific angle with respect to a glass prism (#4, FocTek, BK7, $\theta = 70^\circ$). First, a fiber-coupled halogen light source (Micropack, HL-2000) is collimated (#2, Thorlabs, C110MP-B) and subsequently focused (#3, Thorlabs, C280TME-B) with two aspheric lenses mounted inside a lens tube. A small fiber core is used (#1, Thorlabs, $\varnothing_F = 50 \mu\text{m}$, M14L01), to assure the smallest possible light spot reaching the sample, nicely falling within the bounds of the microfluidic channel. The reflected light passes through a polarizer in TE-mode (#5, Thorlabs, LPVIS050), after which the light is focused onto the core of a multi-mode fiber (#6, Thorlabs, $\varnothing_F = 200 \mu\text{m}$, M25L01), using a mirrored lens-pair combination as the one used in the excitation arm. Both excitation and light collection paths are mounted on tilt platforms, turning the angle at which the optical arms are mounted into a variable for precise signal optimization.

6.3.2 Software

In order to create a software that is compatible with the employed motorized translation stage, and allows for the sequential scanning of the microfluidic channels, the software described in Section 6.2.1 was modified. To this end, the the software logic, displayed in the schematics in Figure 6.2, was altered by adding an additional step to the flow diagram. As can be readily visualized in Figure 6.7A, this extra step involves motor movement. In this case, every time data is saved, in which it does not matter whether the fitting algorithm is triggered or not, the motor is ordered to sequentially move to the next channel, before a new acquisition starts. As depicted in Figure 6.7B, where a screen shot of the new software user-interface is shown, 3 more variables are added to the software: *Channels*, *Graph Offset (nm)* and *Interchannel*

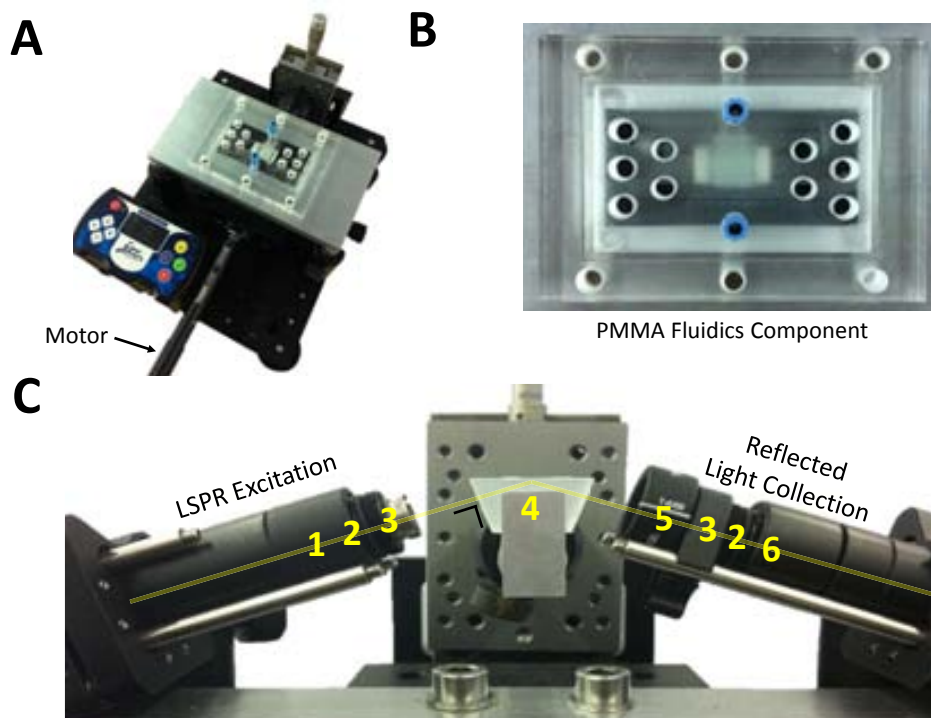


Figure 6.6: (A) Bird-view photograph of the LSPR sensor with multiplexing capabilities. (B) Photograph of the PMMA fluidics component and (C) photograph showing the employed optical components for LSPR excitation and collection of the reflected light.

Distance (μm). The first parameter defines the number of channels, which depending on the number of fabricated microfluidic channels, can be any integer value. The latter parameter defines the center-to-center distance between two subsequent flow channels, and hence, the relative stepping distance of the motor. In the case the last channel is reached in the subsequent channel scanning procedure, the motor is ordered to move back to its initial position, that is, to the first channel, after which the whole channel interrogation cycle starts again. This methodology thus allows for the real-time tracking of λ_{LSPR} in every channel. The remaining parameter, *Graph Offset* (nm), is nothing more than an offset parameter to offset λ_{LSPR} -values in every channel for their proper visualization. An example of λ_{LSPR} -tracking in the case of 8 channels with interchannel distances given by $50 \mu\text{m}$ is can be observed in Figure 6.7B. It should be noted that the read-out speed is limited by two parameters: the speed of the motor, and, the internal data processing of the spectrometer. In our case,

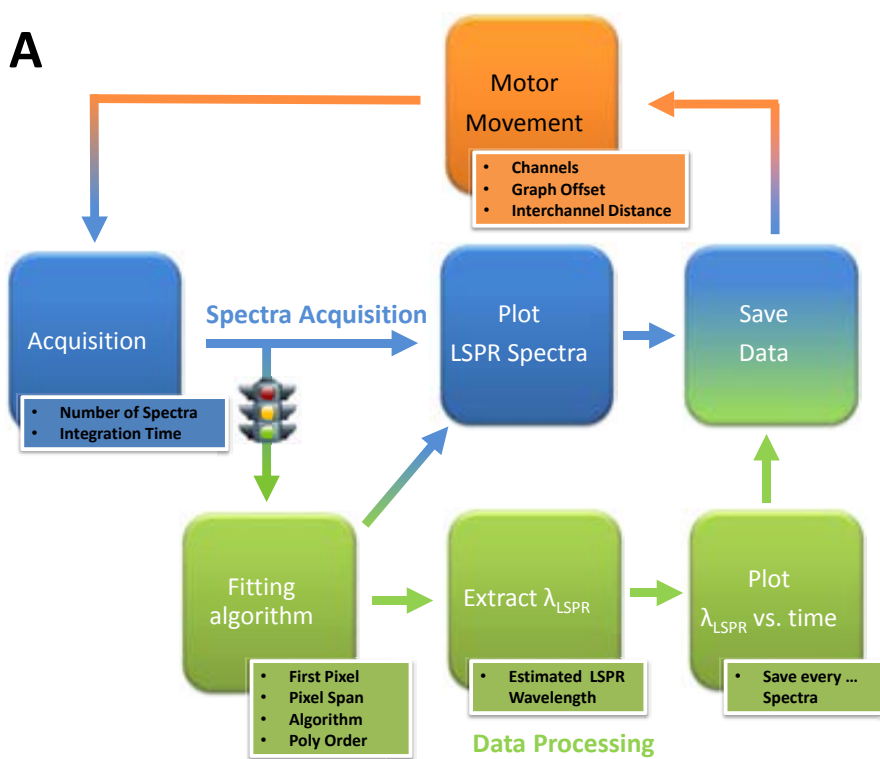
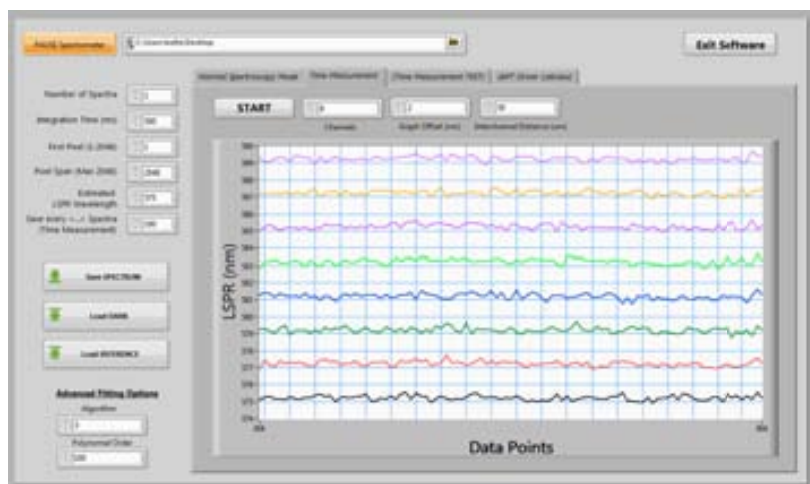
**B**

Figure 6.7: Software schematics and software user interface.

especially the latter parameter strongly affects the read-out speed in a very negative manner: with this particular setup, and assuring a relatively good S/N, between 2 and 5 sec are needed for the data processing of a single channel.

6.3.3 Au Nanodisk Samples and PDMS Microfluidics

After having created a motorized sensing platform with suitable, user-friendly software, the last piece of the puzzle involves the fabrication of the short-range ordered arrays of Au nanodisks, together with the accompanying microfluidics. Fabrication of the Au nanodisk arrays is very straightforward. In this particular case, we fabricate the nanodisk arrays on $7.5\text{ cm} \times 5\text{ cm}$ glass slides, via HCL (Section 2.1.2), taking advantage of this techniques' ease with which large surface areas can be patterned. The size of the glass substrate is chosen in such a manner that it can be precisely embedded in an aluminum stage that fixes its position. However, a more challenging task is the creation of the microfluidics. In our approach, we choose for the patterning of microfluidic channels in a slab of PDMS, using a SU8 patterned substrate as a negative template. This process is described in detail in the next subsection, after which we discuss how the final nanodisk sample, with the PDMS microfluidics on top, is sandwiched between the aluminum stage and the PMMA fluidics component (Section 6.3.3.2).

6.3.3.1 Fabrication of PDMS micro uidics

The fabrication of the PDMS microfluidics is carried out by the subsequent execution of the following 3 steps.

1. Design of a Photolithography Mask

First, a photolithography mask is designed, defining the microfluidic channels that will be fabricated in the subsequent lithographic process. Given the fact that SU8 is a negative resist, only the non-exposed areas remain present after the resist undergoes exposure. Hence, the design motif of the mask exhibits dark areas where flow channel patterning is required, while all other remaining areas are transparent. These masks are constructed by simply printing the desired design onto a transparent sheet at high resolution. A schematic drawing of the employed mask is depicted in Figure 6.8A. The dimensions of the mask are $7.5\text{ cm} \times 5\text{ cm}$, thereby exhibiting the same size as the nanodisk substrate. As a consequence, the mask's corners and those belonging of the same-sized substrate on which the mask will be patterned can be used as mask-alignment

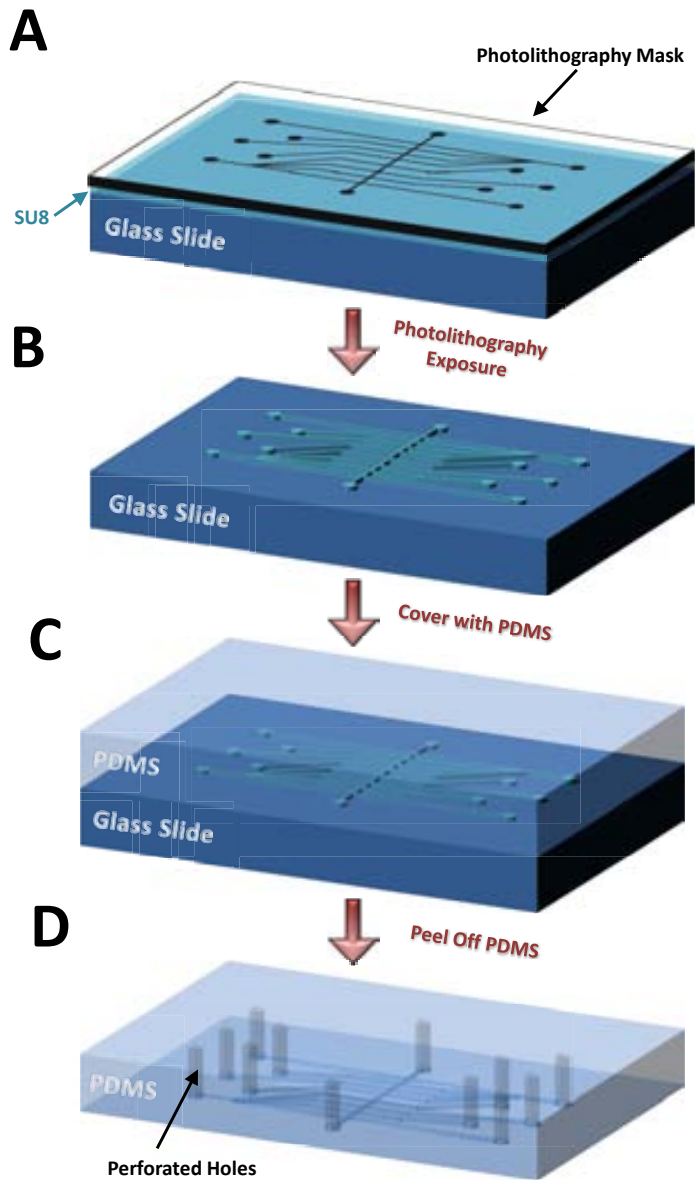


Figure 6.8: Schematics depicting the employed fabrication steps for the creation of the PDMS microfluidics.

markers. As shown in the schematics, this particular mask exhibits 8 horizontal and 1 vertical microfluidic flow channels, all with a width of $300\ \mu\text{m}$. The larger (1 mm diameter) spots at the start- and ending points of the channels coincide exactly with the flow channels fabricated in the PMMA microfluidics component (Figure 6.6B). The larger size of these spots, compared to the channel widths, are intended to facilitate alignment of the resulting PDMS microfluidics and this PMMA microfluidics component.

2. Fabrication of a SU8 Negative Template

Next, the photolithographic process is carried out. Starting out from a clean $7.5\ \text{cm} \times 5\ \text{cm}$ glass substrate, first, an approximately $65\ \mu\text{m}$ thick layer of SU8-2025 resist is spin-coated on the clean glass surface (1500 rpm, $300\ \text{r}\cdot\text{s}^{-2}$, 40 s). In this case, the thickness of the SU8 layer defines the resulting microfluidic channel height. After UV exposure ($180\ \text{mJ}\cdot\text{cm}^{-2}$) and resist development, the final result is a clean glass slide, with the SU8 microfluidics patterned on top. The schematics of this entire photolithographic process are shown in Figures 6.8A and 6.8B.

3. Fabrication of the PDMS Microfluidics

Finally, the PDMS microfluidics are fabricated by using the obtained SU8 patterned glass as a negative mold. For this, the SU8 patterned glass is positioned in a Delrin custom-made open-box with the same dimensions ($7.5\ \text{cm} \times 5\ \text{cm}$), after which a 15 mL mixture of liquid PDMS (Dow Corning, Sylgard® Silicone Elastomer Kit) and its corresponding hardening agent are poured on top at a ratio of 10:1, respectively (This liquid PDMS mixture is previously placed during 15 min in a desiccator in order to remove all the remaining air). This process is schematically depicted in Figures 6.8C. The entire assembly is then located in a preheated oven (60 min, 95°C) to accelerate the curing process of PDMS. When cured, the PDMS can be peeled off the SU8 patterned glass slide, leaving an approximately 4 mm thick PDMS slab, with hollow microfluidic channels patterned on its bottom side, as shown in Figures 6.8D. Finally, a 0.7 mm diameter flat needle is used to perforate the PDMS slab at the positions where the in- and outlets of the microfluidic channels are located.

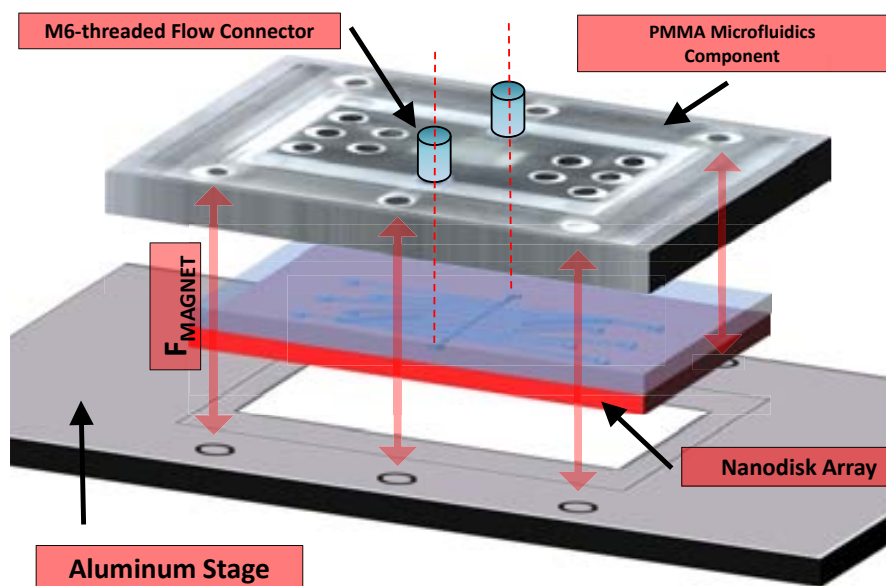


Figure 6.9: Schematic representation of the assembly of the nanodisks/microfluidics combination into the measurement setup of the biosensor.

6.3.3.2 Sample Assembly

The final step consists of the assembly of the nanodisk substrate and the PDMS microfluidics into the measurement scheme. For this, the PDMS microfluidics are placed on top of the nanostructured substrate, and the perforated holes that serve as in- and outlets for liquids, are aligned with the corresponding holes present in the PMMA microfluidics component. This process is schematically depicted in Figures 6.9. The nanodisk/microfluidics combination is then sandwiched between the PMMA component and the aluminum stage, via the attractive force exerted by 6 small magnets (Supermagnete, S-05-05-N, NdFeB, N45) present in both of the latter components. The small magnets, each applying a force of approximately 9 N, press the PDMS microfluidics against the nanodisk sample, thereby providing enough force for proper a sealing of the flow channels. Plastic flow tubing, with slightly larger outer diameters than the perforated holes in the PDMS microfluidics are then squeezed inside the the corresponding holes of the microfluidics. These tubes trespass the PMMA microfluidics component through their corresponding openings and are

attached to the latter via M6-threaded flow connectors, thereby forming a bridge between the microfluidics and the external fluidics of the system.

6.4 Discussion and Conclusion

In this chapter a prototype of a LSPR biosensor with multiplexing capabilities is presented. Interestingly, the proposed measurement setup allows the separation between the employed optics and the microfluidics in two different planes, thereby strongly increasing the accessibility of the system compared to other measurement schemes. Although the measurement setup and the software are finished and ready for use, the work involving the the proper fabrication of the PDMS microfluidics is still in progress. Regarding the microfluidics, preliminary work has shown that the planned idea, in which flow channels are sealed by the simple application of pressure via attractive magnets, indeed works. This methodology is interesting, since it enables re-usability of the PDMS microfluidics. In contrast, although probably better flow-channel sealing can be achieved by permanently bonding the PDMS to the nanodisk substrate, new microfluidics need to be fabricated for every sample. The latter can be easily achieved by a plasma bonding treatment.

Currently, the correct alignment of the holes between the PDMS and the PMMA component form a major challenge. In this regard, we observed that the PDMS contracts once it is peeled off the SU8 mold, making the distances between the in- and outlets different from those defined in the PMMA microfluidics component. To overcome this problem, the initial photolithography mask should be adjusted by this *shrinking factor*, thereby making the designed microfluidic mask larger than intended. In this regard, documented work revealed that thick layer PDMS features shrink by approximately 1.5% when the PDMS is peeled off the SU8 mold. [206] Once this problem is solved, the next step involves investigation regarding the actual flow properties of the PDMS channels, especially paying attention the hydrophobicity of this elastomer, and how the latter affects the proper flow of liquid. Surface modification treatments of the inner walls of the microfluidics, such as silanization or the bonding of Poly-L-Lysine (PLL), [207] might be necessary in order to increase the hydrophilicity and the inertness of the channel walls.

Furthermore, the presented proof-of-concept sensor still offers a lot of room for further optimization and system integration. In an effort to miniaturize and integrate the sensor even more, several alternative hardware components can be found on the market. Firstly, the large syringe pump could be replaced by a very compact

peristaltic pump (Instech, P720-series) that fits into the palm of a hand. However, this replacement goes at the cost of a significant amount of added system noise, caused by the peristaltic nature of this pumping device. Also, coin-sized OEM CMOS spectrometers (Hamamatsu, C11708MA) could replace the employed CCD spectrometer, thereby miniaturizing the system even more. These extremely small spectrometers, not only decrease the device size, they also push down the costs. Besides, an inherent property of CMOS detectors, is their higher signal saturation levels when compared to CCD detectors. As a direct consequence, more photons can be acquired in a single acquisition. Due to these higher saturation levels of CMOS detectors, and taking into account that the internal data processing of both CMOS and CCD spectrometers often is their time-limiting factor, CMOS detectors need spectra, and thus less time, to acquire and process the same amount of photons, when compared to their CCD counterparts. For a fixed number of employed microfluidic channels, the latter automatically leads to faster inter-channel read-out speeds. On the other side, for a fixed read-out time, these faster read-out speeds assure that more microfluidic channels can be addressed, increasing the number of microfluidic channels that can be employed in the sensor.

For all these reasons, the presented device can be seen as a promising model system for the creation of a fast and compact LSPR sensor with multiplexing capabilities. Motivated by its robustness and the fabrication of PDMS microfluidics with cheap laboratory equipment, thereby avoiding expensive clean-room fabrication methods, we strongly believe that device could result in a stable and user-friendly LSPR biosensing platform, which can be used for extensive, fast and high-throughput sensing assays.

General Conclusions

Conclusions

The main conclusions that can be drawn from the theoretical and experimental studies involving refractometric nanoplasmonic sensing that are presented in this manuscript, are the following:

- A FOM parameter that relates the sensitivity and the resolving power of plasmonic refractometric sensors can be used as a measure of their sensing performances. The use of this quantity for the spectral characterization of gold-based SPP sensors and single-nanorod LSPR sensors revealed an optimized spectral sensing region, which can be assigned to the intrinsic optical properties of the employed plasmonic material. For the LSPR sensor, this optimized region corresponds to nanorods with excitation resonances around $\lambda_{\text{LSPR}} \approx 700$ nm. Therefore, accurate choice of particle geometry, allows for the maximization of the sensing performance. For SPP sensors, this optimized sensing region is broader (700 - 1000 nm).
- Using the FOM parameter, it is shown that although the bulk sensing performance of a conventional SPP sensor outclasses that of a single-nanorod LSPR sensor, the surface sensitivity shows a contrary behavior. In this regard, the gold nanorod exhibits an experimentally determined 15% better surface sensing performance compared to its SPP-counterpart. However, supported by theoretical results, this improvement could be boosted towards an enhancement of 300%. For this, access of the molecules to the sensing surface have to be improved, while negative near-field substrate effects have to be suppressed.
- The underlying substrate on which nanoplasmonic structures are fabricated negatively influences their sensing performance. In this regard, plasmonic

damping by a thin metal adhesion layer, which is typically used as a bridging layer for the solid attachment of nanostructures to the substrate, drastically reduces the S/N of the measurements. This negative effect can be greatly suppressed by minimizing the thickness of this layer (1 nm), while using low-absorptive materials, such as titanium.

- The high RI of the substrate (SiO_2 , $n = 1.52$) negatively affects the sensitivity of nanoplasmonic structures. This drawback can be overcome by distancing the nanostructures from the substrate. Using short-range ordered arrays of gold nanodisks as a model system, this distancing process is accomplished by placing the nanodisks on dielectric nanopillars, created via an isotropic wet etch of the SiO_2 . Following this path, DNA hybridization measurements show a sensitivity enhancement of 41% for pillar-supported nanodisks. Due to the facile implementation of this pillar-fabrication technique, its use can be extended towards a great variety of other plasmonic nanostructures.
- When excited by prism-coupling, short-range ordered arrays of gold nanodisks, exhibit a TE guided mode that strongly modifies the far-field radiation properties of these nanostructured substrates. This guided mode is based on strong polarizability-enhancement directly caused by the excitation of the nanodisks' LSPR, thereby behaving as an effective medium with very high RI that allows for light guidance. The presence of this plasmonic guided mode is accompanied by a large improvement of the refractometric sensing sensitivity, yielding a strong enhancement of the LOD in real biosensing experiments.

Considerations and Future Perspectives

One could argue that refractometric nanoplasmonic biosensing is nothing more than the logical consequence of nanotechnology pushing conventional SPP plasmonic biosensing towards new frontiers. Nevertheless, the big question that needs to be answered is whether this evolution is worth the effort. The benefits offered by metal nanostructures, such as sensor miniaturization, multiplexing opportunities and the ability to detect smaller analytes, offer without a doubt possibilities that can difficultly be met by SPP sensors. However, the most important factor that defines a biosensor and puts a measure on its sensing performance is its sensitivity. The results presented herein, attributing a better surface sensing performance to single gold nanorods compared to their SPP counterparts, confirm the potential of nanoplasmonic LSPR

sensors. Although much margin is available for improvement, these results can be considered to be a good basis that motivates further development within the field of nanoplasmonic biosensing. In this regard, the improvement of the sensing performance of short-range ordered arrays of gold nanodisks by overcoming substrate related drawbacks and the enhancement of their far-field radiation properties, as discussed in this work, has profiled these nanostructures as stable, sensitive, and cheap model system for nanoplasmonic biosensing applications, thereby justifying their use in the presented conceptual LSPR sensor with multiplexing capabilities.

Currently, and most probably caused by the youth of this research field, the work published related to nanoplasmonic sensing is often of a very fundamental nature. In this regard, examples that report improved biosensing capabilities are typically accompanied by novel nanoplasmonic structures with enhanced sensitivities, that often rely on new material properties. In this category, the emergence of plasmonic (meta-)materials with unprecedented optical phenomena, such as guided modes, [175, 176, 208] or very sharp Fano resonances, [196, 209] offers great potential for biosensing applications. Nevertheless, in most of these works, the novelty of these *new* materials, pushes their use as biosensing platforms to a secondary plane. In this regard, these studies are often accompanied by - far from optimized - standard proof-of-concept biosensing assays.

As a direct consequence, nowadays, the use of nanoplasmonic sensors as commercial biosensing platforms is still not very realistic. In order to accelerate this technology-transfer process, more research effort should be focused on one of the most underexposed aspects of nanoplasmonic biosensing: *the surface chemistry*. In this regard, proper biofunctionalization of the surface (with or without complementing microfluidic systems) has lead to significant sensitivity enhancements of nanoplasmonic sensing platforms, mainly caused by suppressing non-specific interactions of molecules and forcing biomolecular interactions to take place solely at EM hot-spots of the nanostructures. [170, 200, 210–213] Either way, examples that point towards this direction are few in number. Therefore, in order to dethrone conventional SPP sensing (and its well-studied planar surface chemistry), the current knowledge regarding nanoparticle biofunctionalization should expand drastically. It will not be until then, when accompanied by low cost and large-scale fabrication techniques, commercial nanoplasmonic sensing platforms with integrated microfluidics hit the market, thereby being considered as viable alternatives for conventional SPP sensors.

List of Publications

- **Surface Plasmon Resonance Biosensors for Highly Sensitive Detection in Real Samples**
B. Sepúlveda, L. G. Carrascosa, D. Regatos, M. A. Otte, D. Fariña, and L. M. Lechuga, *Proceed. SPIE Photonics and Optics*, **7397**, 2009, 73970Y-11.
- **Identification of the Optimal Spectral Region for Plasmonic and Nanoplasmonic Sensing**
M. A. Otte, B. Sepúlveda, W. Ni, J. Pérez-Juste, L. M. Liz-Marzán, and L. M. Lechuga, *ACS Nano*, **4** (1), 2010, 349-357.
- **Improved Biosensing Capability with Novel Suspended Nanodisks**
M. A. Otte, M.-C. Estévez, L. G. Carrascosa, A. B. González-Guerrero, L. M. Lechuga, and B. Sepúlveda, *Journal of Physical Chemistry C*, **115** (13), 2011, 5344-5351.
- **Guiding Light in Monolayers of Sparse and Random Plasmonic Meta-atoms**
M. A. Otte, M.-C. Estévez, D. Regatos, L. M. Lechuga, and B. Sepúlveda, *ACS Nano*, **5** (11), 2011, 9179-9186.
- **Figures of Merit for Refractometric LSPR Biosensing**
M. A. Otte, and B. Sepúlveda, *Nanoplasmonic Sensors*, Springer Ed., 2012, 317-331.
- **Review on Nanoplasmonic Biosensing**
M. A. Otte, M.-C. Estévez, B. Sepúlveda, and L. M. Lechuga, *Analytica Chimica Acta*, in preparation.

List of Figures

| | | |
|------|--|----|
| 1.1 | Examples of Advances in Nanotechnology. | 6 |
| 1.2 | Publications in Nanotechnology and Lycurgus Cup. | 7 |
| 1.3 | Schematic Representation Biosensor. | 10 |
| 1.4 | Schematic Representation of Different Bioassays | 11 |
| 1.5 | Schematics of Evanescent Wave Sensors. | 13 |
| 1.6 | Schematics and Field Distribution of a SPP. | 16 |
| 1.7 | SPP Dispersion Relation. | 17 |
| 1.8 | SPP coupling methods, including prism coupling, grating coupling and waveguide coupling. | 18 |
| 1.9 | Schematics Prism-coupled SPP Sensor. | 19 |
| 1.10 | Schematic SPP Resonance Curves and Real-time Tracking of Curve Displacement. | 20 |
| 1.11 | MLWA Calculations of LSPR of Spherical Nanoparticles. | 24 |
| 1.12 | Prolate and Oblate Spheroids. | 26 |
| 1.13 | MLWA Calculations on Ellipsoidal Particles. | 27 |
| 1.14 | Refractometric Sensing Concept LSPR Sensors. | 29 |
| 1.15 | Solutions of Colloidal Nanoparticles. | 31 |
| 1.16 | SEM Images of Nanostructured Surfaces. | 33 |
| 1.17 | Schematic Representation of a Colorimetric LSPR Sensor. | 37 |
| 1.18 | Schematics of Nanoparticle-labeled Sensing Assay. | 38 |
| 2.1 | UV-Visible Transmission Spectra Nanorod Colloids. | 44 |
| 2.2 | Colloidal Hole-Mask Lithography. | 45 |
| 2.3 | Nanodimer Fabrication Schematics and SEM Images of Nanodisks and Nanodimers | 46 |

| | | |
|------|--|-----|
| 2.4 | Schematics of a Pillar-supported Nanodisk. | 48 |
| 2.5 | AFM Top-view Images and Height Profiles of Non-Suspended and Suspended Gold Nanodisks. | 49 |
| 2.6 | Schematics and Photographs of SPP Sensor. | 50 |
| 2.7 | Dark-Field Microscopy Schematics. | 52 |
| 2.8 | Dark-Field Microscopy Measurement Setup. | 53 |
| 2.9 | Fixed Angle LSPR Excitation Setup. | 54 |
| 2.10 | Low and High Angle LSPR Excitation Setup. | 56 |
| 2.11 | Schematics representing SPP and Single Particle LSPR Simulations. | 60 |
| 2.12 | Schematics representing the Maxwell-Garnett Effective Medium Simulations | 62 |
| | | |
| 3.1 | Experimental Setups SPP and LSPR Sensors. | 69 |
| 3.2 | Calculated Bulk Sensing Performances SPP and LSPR Sensors. | 71 |
| 3.3 | Calculated EM-field Penetration Depths of Gold Nanoellipsoids with Varying Aspect Ratios. | 72 |
| 3.4 | Redefinition of the Full Width Half Maximum of a Resonance Peak. | 75 |
| 3.5 | Calculated Surface Sensing Performances SPP and LSPR Sensors. | 76 |
| 3.6 | Bulk and Surface LSPR Sensing Performance of a Nanorod on a Glass Substrate. | 77 |
| 3.7 | Experimental Bulk Sensing Performances SPP and LSPR Sensors | 79 |
| 3.8 | SPP resonance wavelength vs. Light Incident Angle. | 80 |
| 3.9 | Experimental Surface Sensing Performances SPP and LSPR Sensors. | 82 |
| 3.10 | Ratio Between Real and Imaginary Part of the Dielectric Constant of Gold. | 83 |
| 3.11 | Theoretical Surface Sensitivity Parameters Prolate and Oblate Spheroids. | 86 |
| | | |
| 4.1 | Influence of Metal Adhesion Layers on Sensing Performance Gold Nanodisks. | 93 |
| 4.2 | Calculated Substrate-Induced Near Field Effects on the Sensing Performance of a Single Gold Nanodisk Located on top of a Planar Dielectric Substrate. | 96 |
| 4.3 | Calculated Substrate-Induced Near Field Effects on the Sensing Performance of a Dielectric Pillar-Supported Gold Nanodisk. | 98 |
| 4.4 | Experimental Bulk Sensitivity Analysis of Suspended Gold Nanodisks. | 99 |
| 4.5 | DNA Hybridization Measurements on Suspended Gold Nanodisks. | 101 |
| | | |
| 5.1 | Calculated Optical Properties Corresponding to Monolayers of Sparse and Randomly Ordered Arrays of Gold Nanoellipsoids ($F = 2-10\%$). | 109 |
| 5.2 | Calculated Dispersion Relation for a Fixed Nanoellipsoid Density for Different Effective Layer Thicknesses. | 110 |
| 5.3 | Calculated Reflectivity Spectra Corresponding to Monolayers of Sparse and Randomly Ordered Arrays of Gold Nanoellipsoids for $F = 2\%$ and $F = 8\%$ | 112 |
| 5.4 | Calculated TM Dispersion Relations for $F = 2\%$ and $F = 8\%$ | 113 |

| | | |
|------|---|-----|
| 5.5 | Theoretical Tunability of the Absorption Band Using the Aspect Ratio of the Nanoparticles as a Variable for $F = 2\%$ and $F = 2\%$ | 114 |
| 5.6 | Theoretical Bulk Sensitivity Analysis for Monolayers of Sparse and Randomly Ordered Arrays of Gold Nanoellipsoids ($F = 2-10\%$). | 115 |
| 5.7 | Experimental Dispersion Relations of Sparse Nanodisk Arrays with Disk Densities of $F = 5\%$ and $F = 7.5\%$ | 117 |
| 5.8 | Experimental Reflectivity and Transmission Spectra of a Sparse Array of Gold Nanodisks ($F = 7.5\%$). | 118 |
| 5.9 | Experimental TM Dispersion Relations of Sparse Nanodisk Arrays with Disk densities of $F = 5\%$ and $F = 7.5\%$ | 119 |
| 5.10 | Experimental Results Involving Label-free Bulk- and Biosensing Features of Sparse Nanodisk Arrays. | 120 |
| 5.11 | Mode Properties of 20 nm Thick Effective Medium ($F = 2\%$) Comprised Between Equal Dielectrics ($n = 1.52$). | 122 |
| 6.1 | Miniaturized High-Angle LSPR Sensor. | 129 |
| 6.2 | Software Schematics. | 131 |
| 6.3 | Screenshots of Standalone Software Program. | 132 |
| 6.4 | Working Concept Multiplexing LSPR Biosensor. | 134 |
| 6.5 | Design Drawings Multiplexing LSPR Biosensor. | 135 |
| 6.6 | Photographs of Multiplexing LSPR Biosensor. | 137 |
| 6.7 | Software Schematics Multiplexing Biosensor. | 138 |
| 6.8 | Schematics Fabrication of PDMS Microfluidics. | 140 |
| 6.9 | Assembly of Nanodisks/Microfluidics into Multiplexing LSPR Biosensor . . . | 142 |

Abbreviations and Acronyms

| | |
|------|---|
| AFM | Atomic Force Microscopy |
| AR | aspect ratio |
| CCD | charge-coupled device |
| CL | Colloidal Lithography |
| DDA | diallyldimethylammonium chloride |
| DF | dark-field |
| EBL | Electron Beam Lithography |
| EM | electro-magnetic |
| FDTD | finite-difference time-domain |
| FET | Forster Energy Transfer |
| FIB | Focused Ion Beam |
| FOM | figure of merit |
| FWHM | full-width half-maximum |
| GSTC | Generalized Sheet Transition Conditions |
| HCL | Hole-Mask Colloidal Lithography |
| HF | hydrofluoric acid |

| | |
|-------|---|
| IR | infra-red |
| LoC | lab-on-a-chip |
| LOD | limit of detection |
| LSPR | Localized Surface Plasmon Resonance |
| MG | Maxwell-Garnett |
| MLWA | modified long-wavelength approximation |
| MO | magneto-optic |
| MOSPR | Magneto-Optic Surface Plasmon Resonance |
| N.A. | Numerical Aperture |
| NIR | near infra-red |
| NSL | Nanosphere Lithography |
| PDDA | poly(diallyldimethylammonium chloride) |
| PDMS | Polydimethylsiloxane |
| PMMA | poly(methyl methacrylate) |
| PSS | poly(sodium 4-styrenesulfonate) |
| QD | quantum dot |
| RET | Resonant Energy Transfer |
| RI | refractive index |
| RIU | refractive index unit |
| RS | Raman Scattering |
| S/N | signal-to-noise ratio |
| SEF | Surface Enhanced Fluorescence |
| SEM | Scanning Electron Microscopy |
| SERS | Surface Enhanced Raman Scattering |
| SP | Surface Plasmon |
| SPI | Surface Plasmon Imaging |
| SPP | Surface Plasmon Polariton |
| SPR | Surface Plasmon Resonance |

| | |
|-----|----------------------------------|
| STM | Scanning Tunneling Microscopy |
| TE | transverse-electric |
| TEM | Transmission Electron Microscopy |
| TIR | total internal reflection |
| TM | transverse-magnetic |
| VIS | visible |

Symbols

| | |
|--------------------------------|---|
| ΔE_{SPR} | Spectral shift in energy scale of a generic surface plasmon resonance (SPP or LSPR) |
| $\Delta \lambda_{\text{LSPR}}$ | Spectral LSPR resonance shift |
| $\Delta \lambda_{\text{SPR}}$ | Spectral shift in wavelength scale of a generic surface plasmon resonance (SPP or LSPR) |
| Γ | Measure for the electron oscillation in the Drude model |
| α | Polarizability |
| ϵ | Dimensionless dielectric constant of a metal at infinite frequency |
| ϵ_{Im} | Imaginary part of the dielectric constant of a metal |
| ϵ_{Re} | Real part of the dielectric constant of a metal |
| ϵ_{d} | Dielectric constant of a dielectric |
| ϵ_{m} | Dielectric constant of a metal |
| ϵ_{p} | Dielectric constant of a prism |
| ϵ_{s} | Dielectric constant of a coated shell surrounding a nanoellipsoid |
| η | Generic sensitivity parameter of a plasmonic sensor |
| η_{B} | Bulk sensitivity |
| η_{S} | Surface sensitivity |
| η_{in} | Real part of the in-plane n_{e} of a MG effective medium |
| η_{out} | Real part of the out-of-plane n_{e} of a MG effective medium |
| κ_{in} | Imaginary part of the in-plane n_{e} of a MG effective medium |
| κ_{out} | Imaginary part of the out-of-plane n_{e} of a MG effective medium |
| λ | Wavelength |
| λ_{LSPR} | LSPR resonance wavelength |

| | |
|-------------------------------|--|
| λ_{SPP} | SPP resonance wavelength |
| λ_{SPR} | Resonance wavelength of a generic SPR sensor (SPP or LSPR) |
| λ_{max} | Wavelength at which $\epsilon_{\text{Re}}/\epsilon_{\text{Im}}$ is maximized for a metal |
| λ_{p} | Plasma wavelength of a metal |
| ω_{p} | Plasma frequency of a metal |
| κ | Standard deviation |
| θ | Angle |
| θ_{SPP} | SPP resonance angle |
| θ_{TIR} | Angle that triggers TIR |
| \varnothing_{F} | Fiber diameter |
| C_{abs} | Absorption cross-section of a nanoparticle |
| C_{ext} | Extinction cross-section of a nanoparticle |
| C_{sca} | Scattering cross-section of a nanoparticle |
| d | Propagation distance of a guided/propagating plasmonic mode |
| d_{Layer} | Thickness of a dielectric coating layer |
| E_{SPR} | Resonance energy of a generic SPR sensor (SPP or LSPR) |
| F | Theoretical or experimental surface occupation density of nanostructures |
| F_{MLWA} | Correction factor MLWA method |
| FOM_{λ} | Figure of merit in wavelength scale |
| FOM_{E} | Figure of merit in energy scale |
| FWHM_{λ} | Full-width half maximum in wavelength scale |
| FWHM_{E} | Full-width half maximum in energy scale |
| $k_{\text{x}}^{\text{Light}}$ | Wave vector of light |
| $k_{\text{x}}^{\text{SPP}}$ | SPP wave vector |
| k_{\parallel} | Wave-vector of a guided/propagating plasmonic mode |
| L_i | Shape-dependent depolarization factor of an ellipsoid |
| M_{W} | Molecular Weight |

| | |
|------------------|---|
| n_B | Bulk refractive index |
| n_d | Refractive index of a dielectric |
| n_e | Effective refractive index of a MG effective medium |
| n_S | Refractive index of a dielectric shell |
| P | Dipole moment |
| P_{SPR} | Generic peak position of a resonance, defined in wavelength- or energyscale |

Bibliography

- [1] R. P. Feynman. *The Feynman Lectures on Physics*. Addison Wesley, 2005.
- [2] K. E. Drexler. *Engines of Creation*. Oxford University Press, 1992.
- [3] G. Binnig and H. Rohrer. Scanning tunneling microscopy. *IBM J. Res. Dev.*, 30:355–369, 1986.
- [4] G. Binnig, C. F. Quate, and C. Gerber. Atomic force microscope. *Phys. Rev. Lett.*, 56:930–933, 1986.
- [5] R. D. Piner, J. Zhu, F. Xu, S. Hong, and C. A. Mirkin. Dip-pen nanolithography. *Science*, 283:661–663, 1999.
- [6] G. Mie. Beiträge zur optik trüber medien, speziell kolloidaler metallösungen. *Ann. Phys.*, 25:377, 1908.
- [7] S. A. Maier. *Plasmonics: Fundamentals and Applications*. Springer, 2007.
- [8] S. A. Maier, P. G. Kik, H. A. Atwater, S. Meltzer, E. Harel, B. E. Koel, and A. A. G. Requicha. Local detection of electromagnetic energy transport below the diffraction limit in metal nanoparticle plasmon waveguides. *Nat. Mater.*, 2:229–232, 2003.
- [9] W. Dickson, A. Krasavin, G. Wurtz, and A. Zayats. Nonlinear plasmonics: Controlling light with light. *SPIE Newsroom*, 2009.
- [10] B. Sepúlveda, P. C. Angelomé, L. M. Lechuga, and L. M. Liz-Marzán. LSPR-based nanobiosensors. *Nano Today*, 4:244–251, 2009.
- [11] J. N. Anker, W. P. Hall, O. Lyandres, N. C. Shah, J. Zhao, and R. P. Van Duyne. Biosensing with plasmonic nanosensors. *Nat. Mater.*, 7:442–453, 2008.
- [12] K. M. Mayer and J. H. Hafner. Localized surface plasmon resonance sensors. *Chem. Rev.*, 111:3828–3857, 2011.
- [13] J. Wang. Glucose biosensors: 40 years of advances and challenges. *Electroanal.*, 13:983–988, 2001.
- [14] M.-C. Estévez, M. Álvarez, and L. M. Lechuga. Integrated optical devices for lab-on-a-chip biosensing applications. *Laser Phot. Rev.*, 6:463–487, 2012.

- [15] W. K. Kwong. *Catalytic biosensors : novel analytical tools and their applications in sports, food and environmental monitoring*. PhD Thesis, 2000.
- [16] K. Rogers and A. Mulchandani. *Affinity Biosensors: Techniques and Protocols*. Humana Press, 2011.
- [17] D. Grieshaber, R. MacKenzie, J. Vörös, and E. Reimhult. Electrochemical biosensors - sensor principles and architectures. *Sensors*, 8:1400 1458, 2008.
- [18] N. J. Ronkainen, H. B. Halsall, and W. R. Heineman. Electrochemical biosensors. *Chem. Soc. Rev.*, 39:1747 1763, 2010.
- [19] A. B. González-Guerrero, E. Mendoza, E. Pellicer, C. Alsina, C. Fernández-Sánchez, and L. M. Lechuga. Discriminating the carboxylic groups from the total acidic sites in oxidized multi-wall carbon nanotubes by means of acid-base titration. *Chem. Phys. Lett.*, 462:256 259, 2008.
- [20] C. B. Jacobs, M. J. Peairs, and B. J. Venton. Review: Carbon nanotube based electrochemical sensors for biomolecules. *Anal. Chim. Acta.*, 662:105 127, 2010.
- [21] G. N. M. Ferreira, A.-C. da Silva, and B. Tomé. Acoustic wave biosensors: physical models and biological applications of quartz crystal microbalance. *Trends in Biotechnol.*, 27:689 697, 2009.
- [22] L. G. Carrascosa, M. Moreno, M. Álvarez, and L. M. Lechuga. Nanomechanical biosensors: a new sensing tool. *TrAC*, 25:196 206, 2006.
- [23] J. Llandro, J. J. Plafreyman, A. Ionescu, and C. H. W. Barnes. Magnetic biosensor technologies for medical applications: a review. *Med. Biol. Eng. Comput.*, 48:977 998, 2010.
- [24] C. H. Marrows. *Magnetic Biosensor Techniques*. John Wiley and Sons, 2008.
- [25] M. J. Muehlbauer, E. J. Guilbeau, and B. C. Towe. Applications and stability of a thermoelectric enzyme sensor. *Sens. and Act. B: Chemical*, 2:223 232, 1990.
- [26] Y. Zhang and S. Tadigadapa. Calorimetric biosensors with integrated micro uidic channels. *Biosens. Bioelectron.*, 19:1733 1743, 2004.
- [27] S.-C. Park, E.-J. Cho, S.-Y. Moon, S.-I. Yoon, Kim Y.-J., D.-H. Kim, and J.-S. Suh. A calorimetric biosensor and its application for detecting a cancer cell with optical imaging. *World Cong. Med. Phys. Biomed. Eng.*, 14:637 640, 2007.
- [28] F. S. Ligler. *Optical biosensors: today and tomorrow*. Elsevier, 2008.
- [29] L. J. Blum, S. M. Gautier, and P. R. Coulet. Fibre optic biosensors with immobilized bioluminescence enzymes. *J. Mater. Sci. Mater. Med.*, 2:202 204, 1991.
- [30] J. R. Astles, W. G. Miller, C. M. Hanbury, and F. P. Anderson. Fiberoptic immunosensors with continuous analyte response. *Affin. Biosens.*, 7:99 120, 1998.
- [31] D. Marcuse and American Telephone Telegraph Company. *Theory of dielectric optical waveguides*. Academic Press, 1991.
- [32] X. Fan, I. M. White, S. I. Shopova, H. Zhu, J. D. Suter, and Y. Sun. Sensitive optical biosensors for unlabeled targets: A review. *Anal. Chim. Acta*, 620:8 26, 2008.
- [33] F. Xu, P. Horak, and G. Brambilla. Optical micro ber coil resonator refractometric sensor. *Opt. Express*, 15:9385, 2007.

-
- [34] M. Zourob, S. Elwary, X. Fan, S. Mohr, and N. J. Goddard. Label-free detection with the resonant mirror biosensor. *Biosens. Biodelect.*, 503:89–138, 2009.
- [35] K. E. Zinoviev. Integrated bimodal waveguide interferometric biosensor for label-free analysis. *J. Lightwave Technol.*, 29:1926–1930, 2011.
- [36] P. V. Lambeck. Integrated optical sensors for the chemical domain. *Meas. Sci. Technol.*, 19:R93–R116, 2006.
- [37] K. Zinoviev, L. G. Carrascosa, J. Sanchez del Rio, B. Sepúlveda, C. Dominguez, and L. M. Lechuga. Silicon photonic biosensors for lab-on-a-chip applications. *Adv. Opt. Technol.*, 2008:383927–383933, 2008.
- [38] A. Brandenburg, R. Krauter, C. Kunzel, M. Stefan, and H. Schulte. Interferometric sensor for detection of surface-bound bioreactions. *Appl. Opt.*, 39:6396–6405, 2000.
- [39] K. Schmitt, B. Schirmer, C. Hoffmann, Brandenburg, and P. A., Meyrueis. Interferometric biosensor based on planar optical waveguide sensor chips for label-free detection of surface bound bioreactions. *Biosens. Bioelec.*, 22:2591–2597, 2007.
- [40] J. Xu, D. Suarez, and D. S. Gottfried. Detection of avian influenza virus using an interferometric biosensor. *Anal. Bioanal. Chem.*, 389:1193–1199, 2007.
- [41] B. Cunningham, P. Li, B. Lin, and J. Pepper. Colorimetric reaction as a direct biochemical assay technique. *Sens. Act. B-Chem.*, 81:316–328, 2002.
- [42] M. S. Luchansky, A. L. Washburn, T. A. Martin, M. Iqbal, L. C. Gunn, and R. C. Bailey. Characterization of the evanescent field profile and bound mass sensitivity of a label-free silicon photonic microring resonator biosensing platform. *Biosens. Bioelec.*, 26:1283–1291, 2010.
- [43] M. Iqbal, M. A. Gleeson, B. Spaugh, F. Tybor, W. G. Gunn, M. Hochberg, R. C. Baehr-Jones, R. C. Bailey, and L. C. Gunn. Label-free biosensors arrays based on silicon ring resonators and high-speed optical scanning instrumentation. *IEEE J. Sel. Top. Quant. Elec.*, 16:654–661, 2010.
- [44] J. Homola. Surface plasmon resonance sensors for detection of chemical and biological species. *Chem. Rev.*, 108:462–493, 2008.
- [45] A. Leung, P. M. Shankar, and R. Mutharasan. A review of fiber-optic biosensors. *Sens. Act. B-Chem.*, 125:688–703, 2007.
- [46] N. J. Goddard, D. Pollard-Knight, and C. H. Maule. Real-time biomolecular interaction analysis using the resonant mirror sensor. *Analyst*, 119:583–588, 1994.
- [47] A. Brandenburg. Differential refractometry by an integrated-optical Young interferometer. *Sens. and Act. B: Chem.*, 39:266–271, 1997.
- [48] A. Brandenbrug, R. Edelhäuser, W. Konz, W. Ott, and H. Wölfelshneider. A refractometer with fully packaged integrated optical sensor head. *Proc. Opt. Fib. Sens.*, 6:443–447, 1989.
- [49] R. G. Heideman, R. P. H. Kooyman, and J. Greve. Performance of a highly sensitive optical waveguide Mach-Zehnder interferometer immunosensor. *Sens. Act. B: Chem.*, 10:209–217, 1993.
- [50] F. Prieto, B. Sepúlveda, A. Calle, A. Llobera, C. Domínguez, and L. M. Lechuga. Integrated Mach-Zehnder interferometer based on arrow structures for biosensor applications. *Sens. Act. B: Chem.*, 92:151–158, 2003.

- [51] B. H. Schneider, J. G. Edwards, and N. F. Hartman. Hartman interferometer: versatile integrated optic sensor for label-free, real-time quantification of nucleic acids, proteins, and pathogens. *Clin. Chem.*, 43:1757–1763, 1997.
- [52] M. R. Lee and P. M. Fauchet. Two-dimensional silicon photonic crystal based biosensing platform for protein detection. *Opt. Express*, 15:4530–4535, 2007.
- [53] C. J. Choi, I. D. Block, B. Bole, D. Dralle, and B. T. Cunningham. Label-free photonic crystal biosensor integrated microfluidic chip for determination of kinetic reaction rate constants. *IEEE Sens. J.*, 9:1697–1704, 2009.
- [54] A. Ramachandran, S. Wang, J. Clarke, S.J. Ja, D. Goad, L. Wald, E.M. Flood, E. Knobbe, J.V. Hryniewicz, S.T. Chu, D. Gill, W. Chen, O. King, and B.E. Little. A universal biosensing platform based on optical micro-ring resonators. *Biosens. Bioelectron.*, 23:939–944, 2008.
- [55] I. M. White and X. Fan. On the performance quantification of resonant refractive index sensors. *Opt. Express.*, 16:1020–1028, 2008.
- [56] E. Kretschmann. Die bestimmung optischer konstanten von metallen durch anregung von oberflächenplasmaschwingungen. *Z. Phys.*, 241:313–324, 1971.
- [57] S. Park, G. Lee, S. H. Song, C. H. Oh, and P. S. Kim. Resonant coupling of surface plasmons to radiation modes by use of dielectric gratings. *Opt. Lett.*, 28:1870–1872, 2003.
- [58] R. Kashyab and G. Nemova. Surface plasmon resonance-based fiber and planar waveguide sensors. *J. Sens.*, 1:1–9, 2009.
- [59] J. Homola, I. Koudela, and S. S. Yee. Surface plasmon resonance sensors based on diffraction gratings and prism couplers: sensitivity comparison. *Senc. Act. B-Chem.*, 54(1-2):16–24, 1999.
- [60] J. Dostalek, J. Ctyroky, J. Homola, E. Brynda, M. Skalsky, P. Někviňdová, J. Spirková, J. Skvor, and J. Schrofel. Surface plasmon resonance biosensor based on integrated optical waveguide. *Sens. Act. B-Chem.*, 76:8–12, 2001.
- [61] R. Slavik, J. Homola, J. Ctyroky, and E. Brynda. Novel spectral fiber optic sensor based on surface plasmon resonance. *Senc. Act. B-Chem.*, 74(1-3):106–111, 2001.
- [62] O. Telezhnikova and J. Homola. New approach to spectroscopy of surface plasmons. *Opt. Lett.*, 31(22):3339–3341, 2006.
- [63] R. Slavik and J. Homola. Simultaneous excitation of long and short range surface plasmons in an asymmetric structure. *Opt. Comm.*, 259:507–512, 2006.
- [64] R. Slavik, J. Homola, and H. Vaisocherova. Advanced biosensing using simultaneous excitation of short and long range surface plasmons. *Meas. Science Technol.*, 17(4):932–938, 2006.
- [65] B. Rothenhausler and W. Knoll. Surface-plasmon microscopy. *Nature*, 332:615–617, 1988.
- [66] J. Dostalek, H. Vaisocherova, and J. Homola. Multichannel surface plasmon resonance biosensor with wavelength division multiplexing. *Sens. Act. B-Chem.*, 108:758–764, 2005.
- [67] J. Homola, H. Vaisocherova, J. Dostalek, and M. Piliarik. Multi-analyte surface plasmon resonance biosensing. *Methods*, 37(1):26–36, 2005.
- [68] M. Piliarik, H. Vaisocherova, and J. Homola. A new surface plasmon resonance sensor for high-throughput screening applications. *Biosens. Bioelec.*, 20(10):2104–2110, 2005.

-
- [69] S. Y. Wu, H. P. Ho, W. C. Law, C. L. Lin, and S. K. Kong. Highly sensitive differential phase-sensitive surface plasmon resonance biosensor based on the mach-zehnder configuration. *Opt. Lett.*, 29(20):2378–2380, 2004.
- [70] I. R. Hooper and J. R. Sambles. Differential ellipsometric surface plasmon resonance sensors with liquid crystal polarization modulators. *Appl. Phys. Lett.*, 85(15):3017–3019, 2004.
- [71] W. C. Kuo, C. Chou, and H. T. Wu. Optical heterodyne surface-plasmon resonance biosensor. *Opt. Lett.*, 28(15):1329–1331, 2003.
- [72] B. Sepúlveda, L. M. Lechuga, and G. Armelles. Magneto-optic effects in surface-plasmon-polaritons slab waveguides. *J. Lightwave Technol.*, 24:945, 2006.
- [73] D. Regatos, D. Fariña, A. Calle, A. Cebollada, B. Sepúlveda, G. Armelles, and L. M. Lechuga. Au/fe/au multilayer transducers for magneto-optic surface plasmon resonance sensing. *J. Appl. Phys.*, 108:054502, 2010.
- [74] C. F. Bohren and D. R. Huffman. *Absorption and Scattering of Light by Small Particles*. Wiley-VCH, 1983.
- [75] P. B. Johnson and R. W. Christy. Optical constants of the noble metals. *Phys. Rev. B.*, 6:4370–4379, 1972.
- [76] T. Jensen, L. Kelly, A. Lazarides, , and G. C. Schatz. Electrodynamics of noble metal nanoparticles and nanoparticle clusters. *J. Cluster Sci.*, 10:295–317, 1999.
- [77] M. M. Miller and A. A. Lazarides. Sensitivity of metal nanoparticle surface plasmon resonance to the dielectric environment. *J. Phys. Chem. B*, 109:21556–21565, 2005.
- [78] J. Turkevich, P. C. Stevenson, and J. Hillier. A study of the nucleation and growth processes in the synthesis of colloidal gold. *Discussions of the Faraday Society*, (11):55, 1951.
- [79] P. C. Lee and D. Meisel. Adsorption and surface-enhanced raman of dyes on silver and gold sols. *J. Phys. Chem.*, 86(17):3391–3395, 1982.
- [80] D. V. Goia. Preparation and formation mechanisms of uniform metallic particles in homogeneous solutions. *J. Mater. Chem.*, 14(4):451–458, 2004.
- [81] M. Giersig and P. Mulvaney. Preparation of ordered colloid monolayers by electrophoretic deposition. *Langmuir*, 9(12):3408–3413, 1993.
- [82] M. Brust, M. Walker, D. Bethell, D. J. Schiffrin, and R. Whyman. Synthesis of thiol-derivatized gold nanoparticles in a 2-phase liquid-liquid system. *J. Chem. Soc.-Chem. Comm.*, 7:801–802, 1994.
- [83] C. Radloff and N. J. Halas. Enhanced thermal stability of silica-encapsulated metal nanoshells. *Appl. Phys. Lett.*, 79(5):674–676, 2001.
- [84] S. O. Obare, N. R. Jana, and C. J. Murphy. Preparation of polystyrene- and silica-coated gold nanorods and their use as templates for the synthesis of hollow nanotubes. *Nano Lett.*, 1(11):601–603, 2001.
- [85] M. C. Daniel and D. Astruc. Gold nanoparticles: Assembly, supramolecular chemistry, quantum-size-related properties, and applications toward biology, catalysis, and nanotechnology. *Chem. Rev.*, 104:293–346, 2004.

- [86] C. J. Murphy, T. K. San, A. M. Gole, C. J. Orendor , J. X. Gao, L. Gou, S. E. Hunyadi, and T. Li. Anisotropic metal nanoparticles: Synthesis, assembly, and optical applications. *J. Phys. Chem. B*, 109(29):13857–13870, 2005.
- [87] N. R. Jana, L. Gearheart, and C. J. Murphy. Seed-mediated growth approach for shape-controlled synthesis of spheroidal and rod-like gold nanoparticles using a surfactant template. *Adv. Mater.*, 13(18):1389–1393, 2001.
- [88] N. R. Jana. Gram-scale synthesis of soluble, near-monodisperse gold nanorods and other anisotropic nanoparticles. *Small*, 1(8-9):875–882, 2005.
- [89] N. R. Jana, L. Gearheart, and C. J. Murphy. Wet chemical synthesis of high aspect ratio cylindrical gold nanorods. *J. Phys. Chem. B*, 105(19):4065–4067, 2001.
- [90] C. J. Johnson, E. Dujardin, S. A. Davis, C. J. Murphy, and S. Mann. Growth and form of gold nanorods prepared by seed-mediated, surfactant-directed synthesis. *J. Mater. Chem.*, 12(6):1765–1770, 2002.
- [91] B. Nikoobakht and M. A. El-Sayed. Preparation and growth mechanism of gold nanorods using seed-mediated growth method. *Chem. Mater.*, 15:1957–1962, 2003.
- [92] R. C. Jin, Y. W. Cao, C. A. Mirkin, K. L. Kelly, G. C. Schatz, and J. G. Zheng. Photoinduced conversion of silver nanospheres to nanoprisms. *Science*, 294(5548):1901–1903, 2001.
- [93] G. S. Metraux and C. A. Mirkin. Rapid thermal synthesis of silver nanoprisms with chemically tailorable thickness. *Adv. Mater.*, 17(4):412–415, 2005.
- [94] Y. A. Sun and Y. N. Xia. Triangular nanoplates of silver: Synthesis, characterization, and use as sacrificial templates for generating triangular nanorings of gold. *Adv. Mater.*, 15(9):695–699, 2003.
- [95] H. Petrova, J. P. Juste, I. Pastoriza-Santos, G. V. Hartland, L. M. Liz-Marzan, and P. Mulvaney. On the temperature stability of gold nanorods: comparison between thermal and ultrafast laser-induced heating. *Phys. Chem. Chem. Phys.*, 8(7):814–821, 2006.
- [96] R. D. Averitt, D. Sarkar, and N. J. Halas. Plasmon resonance shifts of au-coated au2s nanoshells: Insight into multicomponent nanoparticle growth. *Phys. Rev. Lett.*, 78:4217–4220, 1997.
- [97] S. J. Oldenburg, R. D. Averitt, S. L. Westcott, and N. J. Halas. Nanoengineering of optical resonances. *Chem. Phys. Lett.*, 288(2-4):243–247, 1998.
- [98] H. Wang, D. W. Brandl, F. Le, P. Nordlander, and N. J. Halas. Nanorice: A hybrid plasmonic nanostructure. *Nano Lett.*, 6(4):827–832, 2006.
- [99] J. Y. Chen, B. Wiley, Z. Y. Li, D. Campbell, F. Saeki, H. Cang, L. Au, J. Lee, X. D. Li, and Y. N. Xia. Gold nanocages: Engineering their structure for biomedical applications. *Adv. Mater.*, 17:2255–2261, 2005.
- [100] J. Liu and Y. Lu. Stimuli-responsive disassembly of nanoparticle aggregates for light-up colorimetric sensing. *JACS*, 127(36):12677–12683, 2005.
- [101] N. Nath and A. Chilkoti. A colorimetric gold nanoparticle sensor to interrogate biomolecular interactions in real time on a surface. *Anal. Chem.*, 74(3):504–509, 2002.
- [102] C. Xue, Z. Li, and C. A. Mirkin. Large-scale assembly of single-crystal silver nanoprism monolayers. *Small*, 1(5):513–516, 2005.

-
- [103] K. Fujiwara, H. Watarai, H. Itoh, E. Nakahama, and N. Ogawa. Measurement of antibody binding to protein immobilized on gold nanoparticles by localized surface plasmon spectroscopy. *Anal. Bioanal. Chem.*, 386(3):639–644, 2006.
- [104] M. P. Kreuzer, R. Quidant, G. Badenes, and M. P. Marco. Quantitative detection of doping substances by a localized surface plasmon sensor. *Biosens. Bioelec.*, 21(7):1345–1349, 2006.
- [105] J. J. Mock, D. R. Smith, and S. Schultz. Local refractive index dependence of plasmon resonance spectra from individual nanoparticles. *Nano Lett.*, 3(4):485–491, 2003.
- [106] L. Olofsson, T. Rindzevicius, I. Pfeifer, M. Käll, and F. Höök. Surface-based gold-nanoparticle sensor for specific and quantitative dna hybridization detection. *Langmuir*, 19(24):10414–10419, 2003.
- [107] T. Endo, K. Kerman, N. Nagatani, Y. Takamura, and E. Tamiya. Label-free detection of peptide nucleic acid-dna hybridization using localized surface plasmon resonance based optical biosensor. *Anal. Chem.*, 77:6976–6984, 2005.
- [108] Y. Alaverdyan, B. Sepúlveda, L. Eurenium, E. Olsson, and M. Käll. Optical antennas based on coupled nanoholes in thin metal films. *Nat. Phys.*, 3:884–889, 2007.
- [109] L. Gunnarsson, T. Rindzevicius, J. Prikulis, B. Kasemo, M. Käll, S. L. Zou, and G. C. Schatz. Coupled plasmons in nanofabricated single silver particle pairs: Experimental observations of strong interparticle interactions. *J. Phys. Chem. B*, 109(3):1079–1087, 2005.
- [110] A. N. Grigorenko, H. F. Gleeson, Y. Zhang, N. W. Roberts, A. R. Sidorov, and A. A. Pantelev. Antisymmetric plasmon resonance in coupled gold nanoparticles as a sensitive tool for detection of local index of refraction. *Appl. Phys. Lett.*, 88(12), 2006.
- [111] A. G. Brolo, R. Gordon, B. Leathem, and K. L. Kavanagh. Surface plasmon sensor based on the enhanced light transmission through arrays of nanoholes in gold films. *Langmuir*, 20:4813–4815, 2004.
- [112] J. Dintinger, S. Klein, and T. W. Ebbesen. Molecule-surface plasmon interactions in hole arrays: Enhanced absorption, refractive index changes, and all-optical switching. *Adv. Mater.*, 18:1267–1270, 2006.
- [113] T. R. Jensen, M. L. Duval, K. L. Kelly, A. A. Lazarides, G. C. Schatz, and R. P. Van Duyne. Nanosphere lithography: Effect of the external dielectric medium on the surface plasmon resonance spectrum of a periodic array of silver nanoparticles. *J. Phys. Chem. B*, 103:9846–9853, 1999.
- [114] J. Prikulis, P. Hanarp, L. Olofsson, D. Sutherland, and M. Käll. Optical spectroscopy of nanometric holes in thin gold films. *Nano Lett.*, 4(6):1003–1007, 2004.
- [115] P. Hanarp, M. Käll, and D. S. Sutherland. Optical properties of short range ordered arrays of nanometer gold disks prepared by colloidal lithography. *J. Phys. Chem. B*, 107(24):5768–5772, 2003.
- [116] J. Aizpurua, P. Hanarp, D. S. Sutherland, M. Käll, G. W. Bryant, and F. J. G. de Abajo. Optical properties of gold nanorings. *Phys. Rev. Lett.*, 90:057401, 2003.
- [117] S. Kim, J. M. Jung, D. G. Choi, H. T. Jung, and S. M. Yang. Patterned arrays of au rings for localized surface plasmon resonance. *Langmuir*, 22(17):7109–7112, 2006.

- [118] V. Malyarchuk, F. Hua, N. H. Mack, V. T. Velasquez, J. O. White, R. G. Nuzzo, and J. A. Rogers. High performance plasmonic crystal sensor formed by soft nanoimprint lithography. *Opt. Express*, 13(15):5669–5675, 2005.
- [119] M. E. Stewart, N. H. Mack, V. Malyarchuk, Jant Soares, T. W. Lee, S. K. Gray, R. G. Nuzzo, and J. A. Rogers. Quantitative multispectral biosensing and 1d imaging using quasi-3d plasmonic crystals. *Proc. Nat. Ac. Sc. USA*, 103(46):17143–17148, 2006.
- [120] N. Nath and A. Chilkoti. Label-free biosensing by surface plasmon resonance of nanoparticles on glass: Optimization of nanoparticle size. *Anal. Chem.*, 76(18):5370–5378, 2004.
- [121] F. Frederix, J. M. Friedt, K. H. Choi, W. Laureyn, A. Campitelli, D. Mondelaers, G. Maes, and G. Borghs. Biosensing based on light absorption of nanoscaled gold and silver particles. *Anal. Chem.*, 75(24):6894–6900, 2003.
- [122] S. F. Cheng and L. K. Chau. Colloidal gold-modified optical fiber for chemical and biochemical sensing. *Anal. Chem.*, 75:16–21, 2003.
- [123] K. Mitsui, Y. Handa, and K. Kajikawa. Optical fiber array biosensor based on localized surface plasmon resonance. *Appl. Phys. Lett.*, 85(18):4231–4233, 2004.
- [124] G. Raschke, S. Kowarik, T. Franzl, C. Sönnichsen, T. A. Klar, J. Feldmann, A. Nichtl, and K. Kürzinger. Biomolecular recognition based on single gold nanoparticle light scattering. *Nano Lett.*, 3:935–938, 2003.
- [125] C. L. Baciú, J. Becker, A. Jansho, and C. Sönnichsen. Protein-membrane interaction probed by single plasmonic nanoparticles. *Nano Lett.*, 8:1724–1728, 2008.
- [126] A. J. Haes and R. P. Van Duyne. A nanoscale optical biosensor: Sensitivity and selectivity of an approach based on the localized surface plasmon resonance spectroscopy of triangular silver nanoparticles. *JACS*, 124:10596–10604, 2002.
- [127] J. C. Riboh, A. J. Haes, A. D. McFarland, C. R. Yonzon, and R. P. Van Duyne. A nanoscale optical biosensor: Real-time immunoassay in physiological buffer enabled by improved nanoparticle adhesion. *J. Phys. Chem. B*, 107:1772–1780, 2003.
- [128] C. R. Yonzon, E. Jeoungf, S. L. Zou, G. C. Schatz, M. Mrksich, and R. P. Van Duyne. A comparative analysis of localized and propagating surface plasmon resonance sensors: The binding of concanavalin a to a monosaccharide functionalized self-assembled monolayer. *JACS*, 126(39):12669–12676, 2004.
- [129] A. J. Haes, L. Chang, W. L. Klein, and R. P. Van Duyne. Detection of a biomarker for alzheimer's disease from synthetic and clinical samples using a nanoscale optical biosensor. *JACS*, 127(7):2264–2271, 2005.
- [130] T. Endo, S. Yamamura, N. Nagatani, Y. Morita, Y. Takamura, and E. Tamiya. Localized surface plasmon resonance based optical biosensor using surface modified nanoparticle layer for label-free monitoring of antigen-antibody reaction. *Sc. Technol. Adv. Mater.*, 6:491–500, 2005.
- [131] T. Endo, K. Kerman, N. Nagatani, H. M. Hiepa, D. K. Kim, Y. Yonezawa, K. Nakano, and E. Tamiya. Multiple label-free detection of antigen-antibody reaction using localized surface plasmon resonance-based core-shell structured nanoparticle layer nanochip. *Anal. Chem.*, 78:6465–6475, 2006.

-
- [132] T. Rindzevicius, Y. Alaverdyan, B. Sepúlveda, T. Pakizeh, M. Käll, R. Hillenbrand, J. Aizpurua, and F. J. García de Abajo. Nanohole plasmons in optically thin gold films. *J. Phys. Chem. C*, 111:1207–1212, 2006.
- [133] T. W. Ebbesen, H. J. Lezec, H. F. Ghaemi, T. Thio, and P. A. Wolff. Extraordinary optical transmission through sub-wavelength hole arrays. *Nature*, 391:667–669, 1998.
- [134] Y. S. Jung, Z. Sun, J. Wuenschell, H. K. Kim, P. Kaur, L. Wang, and D. Waldeck. High-sensitivity surface plasmon resonance spectroscopy based on a metal nanoslit array. *Appl. Phys. Lett.*, 88(24), 2006.
- [135] A. Dahlin, M. Zach, T. Rindzevicius, M. Käll, D. S. Sutherland, and F. Höök. Localized surface plasmon resonance sensing of lipid-membrane-mediated biorecognition events. *JACS*, 127:5043–5048, 2005.
- [136] T. Rindzevicius, Y. Alaverdyan, A. Dahlin, F. Höök, D. S. Sutherland, and M. Käll. Plasmonic sensing characteristics of single nanometric holes. *Nano Lett.*, 5:2335–2339, 2005.
- [137] R. Elghanian, J. J. Storho, R. C. Mucic, R. L. Letsinger, and C. A. Mirkin. Selective colorimetric detection of polynucleotides based on the distance-dependent optical properties of gold nanoparticles. *Science*, 277:1078–1080, 1997.
- [138] J. Yguerabide and E. E. Yguerabide. Light-scattering submicroscopic particles as highly fluorescent analogs and their use as tracer labels in clinical and biological applications - i. theory. *Anal. Biochem.*, 262(2):137–156, 1998.
- [139] J. Yguerabide and E. E. Yguerabide. Light-scattering submicroscopic particles as highly fluorescent analogs and their use as tracer labels in clinical and biological applications - ii. experimental characterization. *Anal. Biochem.*, 262(2):157–176, 1998.
- [140] S. Schultz, D. R. Smith, J. J. Mock, and D. A. Schultz. Single-target molecule detection with nonbleaching multicolor optical immunolabels. *Proc. Nat. Ac. Sc. USA*, 97:996–1001, 2000.
- [141] E. Hutter, S. Cha, J. F. Liu, J. Park, J. Yi, J. H. Fendler, and D. Roy. Role of substrate metal in gold nanoparticle enhanced surface plasmon resonance imaging. *J. Phys. Chem. B*, 105(1):8–12, 2001.
- [142] H. X. Xu. Theoretical study of coated spherical metallic nanoparticles for single-molecule surface-enhanced spectroscopy. *Appl. Phys. Lett.*, 85(24):5980–5982, 2004.
- [143] K. Kneipp, Y. Wang, H. Kneipp, L. T. Perelman, I. Itzkan, R. Dasari, and M. S. Feld. Single molecule detection using surface-enhanced raman scattering (sers). *Phys. Rev. Lett.*, 78(9):1667–1670, 1997.
- [144] S. M. Nie and S. R. Emery. Probing single molecules and single nanoparticles by surface-enhanced raman scattering. *Science*, 275(5303):1102–1106, 1997.
- [145] H. X. Xu, E. J. Bjerneld, M. Käll, and L. Borjesson. Spectroscopy of single hemoglobin molecules by surface enhanced raman scattering. *Phys. Rev. Lett.*, 83(21):4357–4360, 1999.
- [146] P. Anger, P. Bharadwaj, and L. Novotny. Enhancement and quenching of single-molecule fluorescence. *Phys. Rev. Lett.*, 96:113002, 2006.
- [147] J. R. Lakowicz. Radiative decay engineering: Biophysical and biomedical applications. *Anal. Biochem.*, 298(1):1–24, 2001.

- [148] D. Boyer, P. Tamarat, A. Maali, B. Lounis, and M. Orrit. Photothermal imaging of nanometer-sized metal particles among scatterers. *Science*, 297:1160–1163, 2002.
- [149] L. R. Hirsch, J. B. Jackson, A. Lee, N. J. Halas, and J. West. A whole blood immunoassay using gold nanoshells. *Anal. Chem.*, 75(10):2377–2381, 2003.
- [150] C. Loo, A. Lowery, N. Halas, J. West, and R. Drezek. Immunotargeted nanoshells for integrated cancer imaging and therapy. *Nano Lett.*, 5(4):709–711, 2005.
- [151] A. S. Angelatos, B. Radt, and F. Caruso. Light-responsive polyelectrolyte/gold nanoparticle microcapsules. *J. Phys. Chem. B*, 109:3071–3076, 2005.
- [152] M. Liu and P. Guyot-Sionnest. Mechanism of silver(i)-assisted growth of gold nanorods and bipyramids. *J. Phys. Chem. B*, 109:22192–22200, 2005.
- [153] H. Fredriksson, Y. Alaverdyan, A. Dmitriev, C. Langhammer, D. S. Sutherland, M. Zäch, and B. Kasemo. Hole-mask colloidal lithography. *Adv. Mater.*, 19:4297–4302, 2007.
- [154] A. B. Dahlin, J. O. Tegenfeldt, and F. Höök. Improving the instrumental resolution of sensors based on localized surface plasmon resonance. *Anal. Chem.*, 78:4416, 2006.
- [155] M. J. Weber. *CRC New York. Handbook of Optical Materials*, 2002.
- [156] M. Schubert. Polarization-dependent optical parameters of arbitrarily anisotropic homogeneous layered systems. *Phys. Rev. B.*, 53:4265–4274, 1996.
- [157] D. M. Sullivan. *Electromagnetic Simulation using the FDTD Method*. New York: IEEE Press Series, 2000.
- [158] A. H. Sihvola and J. A. Kong. Effective permittivity of dielectric mixtures. *IEEE Trans. Geosci. Remote Sensing*, 26:420–429, 1988.
- [159] M. O. Vassell. Structure of optical guided modes in planar multilayers of optically anisotropic materials. *J. Opt. Soc. Am.*, 64:166–173, 1974.
- [160] J. Homola. Present and future of surface plasmon resonance biosensors. *Anal. Bioanal. Chem.*, 377:528–539, 2003.
- [161] W. A. Murray, B. Auguie, and W. L. Barnes. Sensitivity of localized surface plasmon resonances to bulk and local changes in the optical environment. *J. Phys. Chem. C*, 113:5120–5125, 2009.
- [162] C. Novo, Gomez D., J. Pérez-Juste, Z. Zhang, H. Petrova, M. Reismann, P. Mulvaney, and G. V. Hartland. Contributions from radiation damping and surface scattering to the linewidth of the longitudinal plasmon band of gold nanorods: A single particle study. *Phys. Chem. Chem. Phys.*, 8:3540–3546, 2006.
- [163] L. J. Sherry, S.-H. Chang, G. C. Schatz, R. P. Van Duyne, B. J. Wiley, and Y. Xia. Localized surface plasmon resonance spectroscopy of single silver nanocubes. *Nano Lett.*, 5:2034–2038, 2005.
- [164] P. Kvasnička and J. Homola. Optical sensors based on spectroscopy of localized surface plasmons on metallic nanoparticles: Sensitivity considerations. *Biointerphases*, 3:FD4–FD11, 2008.
- [165] M. D. Malinsky, K. L. Kelly, G. C. Schatz, and R. P. Van Duyne. Nanosphere lithography: Effect of substrate on the localized surface plasmon resonance spectrum of silver nanoparticles. *J. Phys. Chem. B*, 105:2343–2350, 2001.

- [166] L. Richert, Y. Arntz, P. Schaaf, J.-C. Voegel, and C. Picart. pH-dependent growth of poly(L-lysine)/poly(L-glutamic) acid multilayers and their cell adhesion properties. *Surf. Sci.*, 570:13–29, 2004.
- [167] G. J. Nusz, A. C. Curry, S. M. Marinakos, A. Wax, and A. Chilkoti. Rational selection of gold nanorod geometry for label-free plasmonic biosensors. *ACS Nano*, 3:795–806, 2009.
- [168] A. Dmitriev, C. Hägglund, S. Chen, H. Fredriksson, T. Pakizeh, M. Käll, , and D. S. Sutherland. Enhanced nanoplasmonic optical sensors with reduced substrate effect. *Nano Lett.*, 8:3893–3898, 2008.
- [169] B. Brian, B. Sepúlveda, Y. Alaverdyan, L. M. Lechuga, and M. Käll. Sensitivity enhancement of nanoplasmonic sensors in low refractive index substrates. *Opt. Express*, 17:2015–2023, 2009.
- [170] L. Feuz, P. Jönsson, M. P. Jonsson, and F. Höök. Improving the limit of detection of nanoscale sensors by directed binding to high-sensitivity areas. *ACS Nano*, 4:2167–2177, 2010.
- [171] M. P. Jonsson, A. B. Dahlin, L. Feuz, S. Petronis, and F. Höök. Locally functionalized short-range ordered nanoplasmonic pores for bioanalytical sensing. *Anal. Chem.*, 82:2087–2094, 2010.
- [172] P.-Y. Chung, T.-H. Lin, G. Schultz, C. Batich, and P. Jiang. Nanopyramid surface plasmon resonance sensors. *Appl. Phys. Lett.*, 96:261108–261103, 2010.
- [173] S. S. Acimovic, M. P. Kreuzer, M. U. Gonzalez, and R. Quidant. Plasmon near-field coupling in metal dimers as a step toward single-molecule sensing. *ACS Nano*, 3:1231–1237, 2009.
- [174] E. M. Larsson, J. Alegret, M. Käll, and D. S. Sutherland. Sensing characteristics of near localized surface plasmon resonances in gold nanorings for application as ultrasensitive biosensors. *Nano Lett.*, 7:1256–1263, 2007.
- [175] A. V. Kabashin, P. Evans, S. Pastkovsky, W. Hendren, G. A. Wurtz, R. Atkinson, R. Pollard, V. A. Podolskiy, and A. V. Zayats. Plasmonic nanorod metamaterials for biosensing. *Nat. Mater.*, 8:867–871, 2009.
- [176] J. McPhillips, A. Murphy, M. P. Jonsson, W. R. Hendren, R. Atkinson, F. Höök, A. V. Zayats, and R. J. Pollard. High-performance biosensing using arrays of plasmonic nanotubes. *ACS Nano*, 4:2210–2216, 2010.
- [177] S. Chen, M. Svedendahl, M. Käll, L. Gunnarsson, and A. Dmitriev. Ultrahigh sensitivity made simple: Nanoplasmonic label-free biosensing with an extremely low limit-of-detection for bacterial and cancer diagnostics. *Nanotechnology*, 20:434015, 2009.
- [178] A. Das, J. Zhao, G. C. Schatz, S. G. Sligar, and R. P. Van Duyne. Screening of type I and II drug binding to human cytochrome P450-3A4 in nanodiscs by localized surface plasmon resonance spectroscopy. *Anal. Chem.*, 81:3754–3759, 2009.
- [179] M. Svedendahl, S. Chen, A. Dmitriev, and M. Käll. Refractometric sensing using propagating versus localized surface plasmons: A direct comparison. *Nano Lett.*, 9:4428–4433, 2009.
- [180] M. A. Otte, B. Sepúlveda, W. Ni, J. Pérez-Juste, L. M. Liz-Marzán, and L. M. Lechuga. Identification of the optimal spectral region for plasmonic and nanoplasmonic sensing. *ACS Nano*, 4:349–357, 2010.
- [181] Beeram S. R. and F. P. Zamborini. Purification of gold nanoplates grown directly on surfaces for enhanced localized surface plasmon resonance biosensing. *ACS Nano*, 4:3633–3646, 2010.

- [182] L. Carrascosa, A. Calle, and L. M. Lechuga. Label-free detection of dna mutations by spr: Application to the early detection of inherited breast cancer. *Anal. Bioanal. Chem.*, 393:1173–1182, 2009.
- [183] R. Charbonneau, P. Berini, E. Berolo, and E. Lisicka-Shrzek. Experimental observation of plasmon polariton waves supported by a thin metal film of finite width. *Opt. Lett.*, 25:844–846, 2000.
- [184] I. Salakhutdinov, J. S. Thakur, and K. Leosson. Characterization of long-range surface plasmon-polariton in stripe waveguides using scanning near-field optical microscopy. *J. Appl. Phys.*, 102:123110–123115, 2007.
- [185] I. De Leon and P. Berini. Amplification of long-range surface plasmons by a dipolar gain medium. *Nat. Photon.*, 4:382–387, 2010.
- [186] E. Verhagen, J. A. Dionne, L. Kuipers, H. A. Atwater, and A. Polman. Near-field visualization of strongly confined surface plasmon polaritons in metal-insulator-metal waveguides. *Nano Lett.*, 8:2925–2929, 2008.
- [187] R. F. Oulton, V. J. Sorger, D. A. Genov, D. F. P. Pile, and X. Zhang. A hybrid plasmonic waveguide for subwavelength confinement and long-range propagation. *Nat. Photon.*, 2:496–500, 2008.
- [188] V. J. Sorger, Z. Ye, R. F. Oulton, Y. Wang, G. Bartal, X. Yin, and X. Zhang. Experimental demonstration of low-loss optical waveguiding at deep sub-wavelength scales. *Nat. Commun.*, 2:331, 2011.
- [189] S. I. Bozhevolnyi, V. S. Volkov, E. Devaux, J.-Y. Laluet, and T. W. Ebbesen. Channel plasmon subwavelength waveguide components including interferometers and ring resonators. *Nature*, 440:508–511, 2006.
- [190] B. Augu e and W. L. Barnes. Collective resonances in gold nanoparticle arrays. *Phys. Rev. Lett.*, 101:143902, 2008.
- [191] Y. Chu, E. Schonbrun, T. Yang, and K. B. Crozier. Experimental observation of narrow surface plasmon resonances in gold nanoparticle arrays. *Appl. Phys. Lett.*, 93:181108–181103, 2008.
- [192] E. M. Hicks, S. Zou, G. C. Schatz, K. G. Spears, R. P. Van Duyne, L. Gunnarsson, T. Rindzevicius, B. Kasemo, and M. K all. Controlling plasmon line shapes through directive coupling in linear arrays of cylindrical nanoparticles fabricated by electron beam lithography. *Nano Lett.*, 5:1065–1070, 2005.
- [193] V. G. Kravets, F. Schedin, and A. N. Grigorenko. Extremely narrow plasmon resonances based on directive coupling of localized plasmons in arrays of metallic nanoparticles. *Phys. Rev. Lett.*, 101:087403, 2008.
- [194] G. Vecchi, V. Giannini, and J. G omez Rivas. Surface modes in plasmonic crystals induced by directive coupling of nanoantennas. *Phys. Rev. B*, 80:201401, 2009.
- [195] T. Yang and K. B. Crozier. Dispersion and extinction of surface plasmons in an array of gold nanoparticle chains: Influence of the air/glass interface. *Opt. Express*, 16:8570–8580, 2008.
- [196] W. Zhou and T. W. Odom. Tunable subradiant lattice plasmons by out-of-plane dipolar interactions. *Nat. Nanotechn.*, 6:423–427, 2011.

-
- [197] C. L. Holloway, E. F. Kuester, and D. Novotny. Waveguides composed of metasurfaces: The two-dimensional equivalent of metamaterials. *IEEE Antennas Wireless Propag. Lett.*, 8:525–529, 2009.
- [198] J.-W. Dong, K. H. Fung, C. T. Chan, and H.-Z. Wang. Localization characteristics of two-dimensional quasicrystals consisting of metal nanoparticles. *Phys. Rev. B*, 80:155118, 2009.
- [199] A. Aubry, D. Y. Lei, A. I. Fernández-Domínguez, Y. Sonnefraud, S. A. Maier, and J. B. Pendry. Plasmonic light-harvesting devices over the whole visible spectrum. *Nano Lett.*, 10:2574–2579, 2010.
- [200] M. A. Otte, M. C. Estévez, L. G. Carrascosa, A. B. González-Guerrero, L. M. Lechuga, and B. Sepúlveda. Improved biosensing capability with novel suspended nanodisks. *J. Phys. Chem. C*, 115:5344–5351, 2011.
- [201] A. Abad, J. Primo, and A. Montoya. Development of an enzyme-linked immunosorbent assay to carbaryl. 1. antibody production from several haptens and characterization in different immunoassay formats. *J. Agric. Food Chem.*, 45:1486–1494, 1997.
- [202] M. A. González-Martínez, S. Morais, R. Puchades, A. Maquieira, A. Abad, and A. Montoya. Monoclonal antibody-based flow-through immunosensor for analysis of carbaryl. *Anal. Chem.*, 69:2812–2818, 1997.
- [203] E. Mauriz, A. Calle, A. Montoya, and L. M. Lechuga. Determination of environmental organic pollutants with a portable optical immunosensor. *Talanta*, 69:359–364, 2006.
- [204] A. Dmitriev, T. Pakizeh, M. Käll, and Sutherland D. S. Gold-silica-gold nanosandwiches: Tunable bimodal plasmonic resonators. *Small*, 3:294–299, 2007.
- [205] J. B. González-Díaz, A. García-Martín, J. M. García-Martín, A. Cebollada, G. Armelles, B. Sepúlveda, Y. Alaverdyan, and M. Käll. Plasmonic au/co/au nanosandwiches with enhanced magneto-optical activity. *Small*, 4:202–205, 2008.
- [206] J. M. Spotts. Fabrication of pdms microfluidic devices. http://corefacilities.systemsbiology.net/foswiki/pub/Microfluidics/IntroLectures/PDMS_Microfluidic_Device_Fabrication.pdf.
- [207] J. Harris, H. Lee, B. Vahidi, C. Tu, D. Cribbs, N. L. Jeon, and C. Cotman. Fabrication of a microfluidic device for the compartmentalization of neuron soma and axons. *J. Vis. Exp.*, 7:e261, 2007.
- [208] M. A. Otte, M.-C. Estévez, D. Regatos, L. M. Lechuga, and B. Sepúlveda. Guiding light in monolayers of sparse and random plasmonic meta-atoms. *ACS Nano*, 5:9179–9186, 2011.
- [209] N. J. Halas, S. Lal, W.-S. Chang, S. Link, and P. Nordlander. Plasmons in strongly coupled metallic nanostructures. *Chem. Rev.*, 111:3913–3961, 2011.
- [210] F. Eftekhari, C. Escobedo, J. Ferreira, X. Duan, E. M. Girotto, A. G. Brolo, R. Gordon, and D. Sinton. Nanoholes as nanochannels: Flow-through plasmonic sensing. *Anal. Chem.*, 81:4308–4311, 2009.
- [211] A. A. Yanik, M. Huang, A. Artar, T.-Y. Chang, and H. Altug. Integrated nanoplasmonic-nanofluidic biosensors with targeted delivery of analytes. *Appl. Phys. Lett.*, 96:021101, 2010.
- [212] L. Feuz, M. P. Jonsson, and F. Höök. Material-selective surface chemistry for nanoplasmonic sensors: Optimizing sensitivity and controlling binding to local hot spots. *Nano Lett.*, 12:873–879, 2012.

-
- [213] C. Escobedo, A. G. Brolo, R. Gordon, and D. Sinton. Opto uidic concentration: Plasmonic nanostructure as concentrator and sensor. *Nano Lett.*, 12:1592–1596, 2012.

